NEUTRON-PROTON BREMSSTRAHLUNG AT 4.8 MeV

J. WHITTAKER

A thesis submitted for the degree of Doctor of Philosophy
at the University of Cape Town

November 1979

ABSTRACT

The differential cross-section for neutron-proton bremsstrahlung at an incident energy of 4.8 MeV has been measured where the outgoing nucleon angles were $\theta_n = 35^0$, $\theta_p = 25^0$. An upper limit to $d^2\sigma/d\Omega_n d\Omega_p$ of 210 $\mu b/sr^2$ was found. The experimental method was unusual in that the target was an organic scintillation crystal which also served as recoil proton detector, and the bremsstrahlung photon was detected in addition to the two nucleons in a second crystal. An estimate of the cross-section corresponding to this experiment has been made using elastic scattering parameters. The measured upper limit is above this and other theoretical predictions, but represents a marked improvement over previous measurements in the energy range.

CONTENTS

---ooOoo---

CHAPTER 1

INTRODUCTION

1.1 THE 2-NUCLEON INTERACTION

A great deal of effort, both experimental and theoretical, has gone into the study of the force between two nucleons, as this is the basic component for an understanding of the structure of all nuclear matter. Much of the recent work has been concentrated on the investigation of elastic collisions between two nucleons in which the observables are differential cross-sections and, as a result of nucleon spin, polarization parameters. Unfortunately, the presence of spin allows considerable complexity; for each energy and scattering angle there are 256 distinct experiments which may be performed [1]; of these, 5 are independent if the currently accepted conservations laws hold. Subject to these constraints, the interaction has been found to display the maximum variation.

One of the primary aims of these collision studies has been to establish a simple potential which fits all the experimental scattering and bound-state data. However, potentials which satisfy the data are not of the desired concise form; one of the most widely used, that of Hamada and Johnston [2] has 31 parameters [1] which have been set to achieve agreement with experiment.

As a result of this effort, 2-nucleon elastic collisions can be considered reasonably well defined, although the force is complicated and no new simplifying generalisations have been found.

1.2 THE 2-NUCLEON INTERACTION OFF-THE-ENERGY-SHELL

The information obtained from elastic 2-nucleon collisions is restricted in that energy is conserved, i.e. the interaction is on-the-energy-shell. When three or more particles interact, the 2-nucleon part of the interaction does not in general conserve energy and a complete knowledge of the 2-nucleon interaction therefore further requires information off-the-energy-shell. The most direct way to study the off-shell behaviour is by means of nucleon-nucleon bremsstrahlung (NNB), in which a photon is emitted from a nucleon-nucleon collision. In Chapter 5 it is shown how off-shell effects arise in NNB as manifested by off-shell elements* of the 2-nucleon transition matrix.

---

* A distinction is sometimes made between 'fully-off-shell' and 'half-off-shell' elements [3]. In this terminology, the elements encountered in NNB are half-off-shell.

Unfortunately, NNB cross-sections are small, being less than those for N-N elastic scattering by a factor of $\simeq 10^5$ in typical geometries. This makes NNB experiments difficult.

' A satisfactory potential must also yield correct off-shell predictions and an important motive for NNB experiments is the testing of potential models which appear to satisfy the on-shell data.

1.3 NUCLEON-NUCLEON BREMSSTRAHLUNG (NNB) EXPERIMENTS

The review papers of Halbert [4] and Jovanovich [5] cover experiments which have been done since work began on NNB some 15 years ago. In spite of the fact that npB cross-sections are larger than ppB by typically a factor of 10 (Sect. 5.4), most experiments have been ppB because they are easier. Protons can be easily produced in a collimated beam and directly detected, whilst monodirectional neutron beams are unavailable, and detection is by indirect methods. However, npB experiments are necessary if the full scheme of the 2-nucleon interaction is to be investigated as they alone can yield information about the T=0 isospin state of the interaction. Moreover, it has been predicted that npB cross-sections are more sensitive to off-shell effects than ppB [6].

Most measurements have been of differential cross-sections, $d^2\sigma/d\Omega_1 d\Omega_2$, in the Harvard geometry (Fig. 1.1) which has coplanar detectors for the two nucleons only*. NN elastic scatters are excluded as the sum of the laboratory scattering
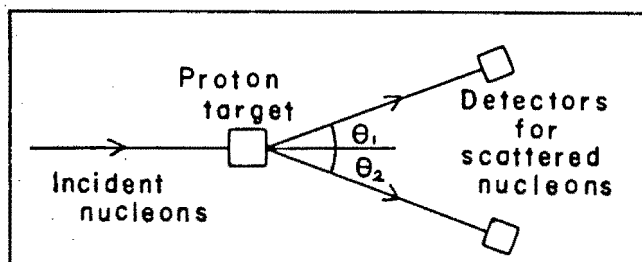
Fig. 1.1

Harvard geometry. The detectors for the scattered nucleons are coplanar with the incident beam, and the photon is undetected. Elastic scatters are excluded since $\theta_1 + \theta_2 < 90^0$.

angles, $\theta_1 + \theta_2$, is less than 90^0, and NNB events are selected by their position on the E1 - E2 plane (Fig. 1.2).

Following a number of simpler experiments, the recent trend in ppB has been to mount large-scale experiments [7,8] using multi-wire proportional counters which measure cross-sections over a large range of angles simultaneously, with uncertainties down to about 10%. The npB work has not reached this stage and

---

* Some authors include a restriction to equal scattering angles in the definition of Harvard geometry.
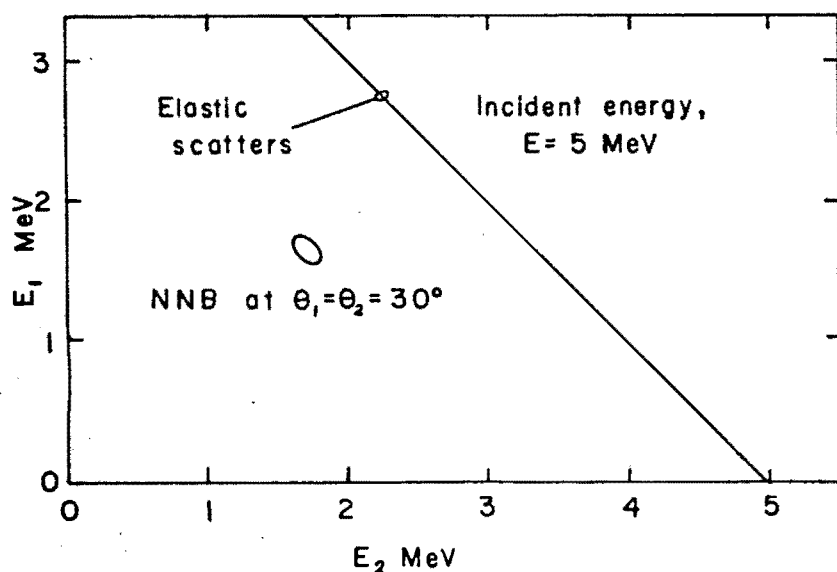
Fig. 1.2

Kinematic restrictions for NNB events (see Appendix Al). The periphery of the small region is the allowed locus for coplanar NNB events at $\theta_1 = \theta_2 = 30^0$, E = 5 MeV, as the photon emission angle rotates through 360^0. E_1 and E_2 are the outgoing nucleon energies. Non-coplanar events would populate the inside of the region; the kinematics allow the nucleons to be non-coplanar by a few degrees (see Sect. 5.8).

all known results are summarised in Table 1.1. They are few and of poor accuracy compared with ppB, particularly below 100 MeV. Indeed, to quote Jovanovich [5], "the low energy npB experiments are almost impossible within the framework of existing technologies".

This work was intended to test this contention, and to find the limits of accuracy to be expected in this low energy range. In the design we have concentrated on making the experiment reasonably possible, rather than paying attention to those kinematic regions (e.g. small θ_1, θ_2, see Sect. 5.5) which might maximise off-shell information.

Chapters 2, 3 and 4 describe the experiment in detail up to the production of a cross-section value. Chapter 5 contains an outline of NNB theory together with a brief review of calculations and their features, and our result is compared with some theoretical predictions (Sect. 5.7). Finally, in Chapter 6, some comments are made about the status of NNB work as a whole.

Energy MeV	Institution	θ_n , θ_p	Cross-section $d^2\sigma/d\Omega_n d\Omega_p$	Ref.	Date reported
208	U.C. Davis	30^0, 30^0	35 ± 14 μb/sr^2	[9]	1968
130	Harwell	32^0, 29^0	77 ± 32 μb/sr^2	[10]	1974
14.4	R. Boskovic Zagreb	30^0, 30^0	< 400 μb/sr^2	[11]	1970
14	UCLA	30^0, All	(< 170 μb/sr)*	[12]	1967

* Single differential cross-section, $d\sigma/d\Omega_n$. This result implies an upper limit to $d^2\sigma/d\Omega_p d\Omega_n$ of the order of 3 mb/sr^2.

Table 1.1

npB experiments at or near $\theta_n = \theta_p = 30^0$ in Harvard geometry. The measurements at 130 and 208 MeV also included other angles. Two experiments using p-n scattering with deuterium as a quasi-free neutron target have not been included.

CHAPTER 2

EXPERIMENTAL METHOD

2.1 OVERVIEW

Because of the low probability of NNB events, with NN elastic scatters more probable by a factor of typically 10^5, a successful experiment will be highly selective in order to count NNB events preferentially above all types of background. On the other hand, high selectivity implies a low rate of event counting.

Harvard geometry (Sect. 1.3) has been widely used for NNB experiments as it can be made sufficiently selective; this can be ascribed to the fact that each event is kinematically overdetermined. For an event there are 9 variables (3 energies, 6 angles, see Fig. 2.1) which are reduced to 5 on applying conservation of energy and momentum. Assuming point detectors, 6 variables are determined in Harvard geometry. For ppB, the proton directions, and thus the event itself, can be defined within narrow limits by the use of suitable detectors, for example, multi-wire counters or proton 'telescopes' consisting of two or more aligned detectors. With sufficient precision, at the expense of count rates, all types of background can be made negligible.
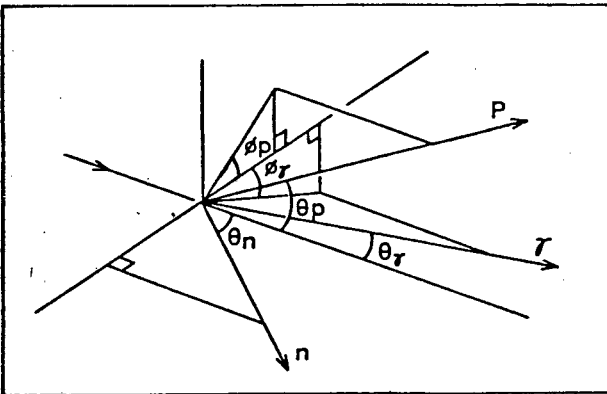
Fig. 2.1

Definition of angles of scattered particles for npB. We define the plane to contain the scattered neutron, thus $\phi_n = 0$.

Harvard geometry is less precise for npB although it was used for all the experiments listed in Table 1.1 except UCLA. The imprecision results from the spread in angle and energy from available neutron sources and from the lack of a direction-sensitive detector. Further, the neutron energy must be inferred from time-of-flight measurements rather than pulse-height. At low energies (0-20 MeV) these problems are compounded by the need for the proton to emerge from the target for detection. For instance, a 3 MeV proton in a CH_2 target has a range of only $\simeq 0.1$ mm, so the target must be very thin with consequent

prohibitively low count rates.   This was a problem in the Zagreb experiment at
14.4 MeV [11]; a month's run yielded -2 ± 2.8 events.   The same considerations
of short range preclude the direction-sensitive proton detectors mentioned above.

The approach in this experiment was to avoid the thin target by using a
scintillation crystal (stilbene) as proton target and detector.   The recoil
proton direction was thus completely unknown, and the resulting lack of
selectivity was overcome, albeit with a rate loss of a further factor of $\simeq 10^2$,
by the inclusion of a third detector for the npB photon.   The final count after
background subtraction was 1.5 events nett from 125 hours' running (Sect. 3.13).

We first outline the design used (Sect. 2.2) and then discuss more of the
detailed reasons for it (Sect. 2.3).   The remainder of this chapter is concerned
with the techniques used in the experiment and in data acquisition.

2.2 OUTLINE OF METHOD

The geometry is shown in Fig. 2.2.   The target was one of the stilbene
crystals which also detected the npB proton, with the other stilbene crystal
used for detection of the photon.   The two crystals were interchangeable in
that either could function as target, and data was collected for both alternatives.
During analysis (Sect. 3.4) events with a proton in detector 1 and photon in
detector 2 (p-γ events) were separated from the opposite variety (γ-p events) by
pulse-shape discrimination (PSD).   The npB neutron was detected in a separate
liquid scintillator which also used PSD to remove gammas.   An accepted event
consisted of a triple coincidence with suitable windows set on the time between
the signals from the three detectors.
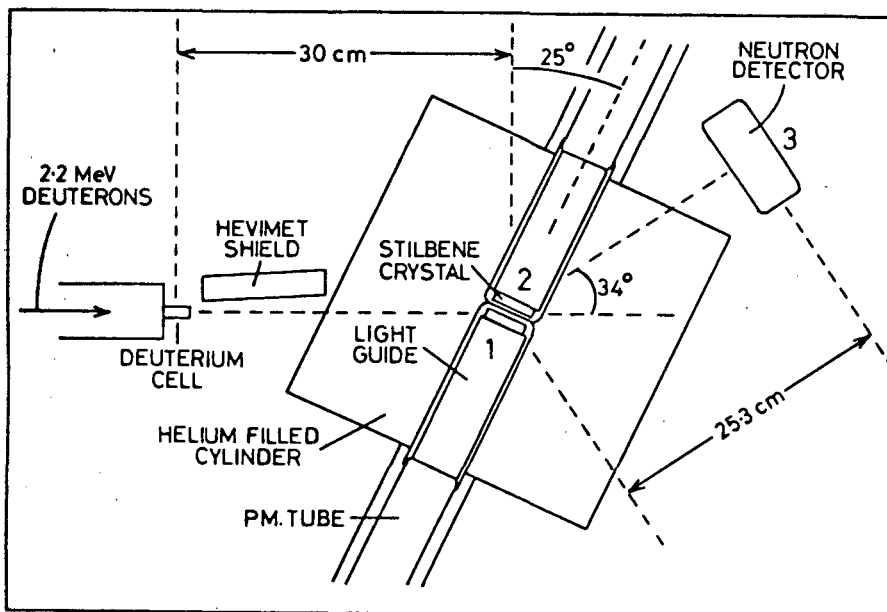
Fig. 2.2

Experimental geometry

The purpose of the helium chamber and the stilbene detector construction was to remove some types of unsubtractable background (Sect. 2.3g).

The incident neutron energy was 4.8 MeV, and the outgoing nucleon angles, as selected in the data reduction (Sect. 3.12) were $\theta_n = 35^0 \pm 5^0$, $\theta_p = 25^0 \pm 10^0$. This limited the observed final energies to $E_n = 0.4$ to 2.0 MeV, $E_p = 1.4$ to 3.1 MeV, $E_\gamma = 0.9$ to 1.9 MeV by virtue of the kinematics of npB (Sect. 2.3f).

In the following sections, the method is justified and some other possibilities are discussed. Most of the experimental parameters, such as detector volumes, are a compromise between conflicting requirements, but it is unlikely that any modifications to the chosen design would bring significantly improved results. Of special importance were the PSD system on the stilbene detectors (Sect. 2.6a) as good p-γ separation was needed at low energy, and the circuit and alignment of the electronics (Sect. 2.7). Due to the very low npB count rate, any small defect in the electronic system could have given rise to spurious information.

2.3 REASONS FOR CHOICE OF METHOD

2.3a Target and proton detector

A proton target without the presence of other nuclei does not exist. The two practical targets available are liquid hydrogen, which has other nuclei in its container, and hydrocarbon. Scatters involving these unwanted nuclei must be eliminated from the count. The motives for selecting a hydrocarbon target in the form of a scintillator have been mentioned in Sect. 2.1. The particular choice of trans-stilbene ($C_{14}H_{12}$) as scintillation crystal was because of its PSD properties [13]; good separation of protons from gammas was required down to low energies.

With regard to the size of the target, the volume that may be used is limited by multiple scattering; furthermore, if the count rate at the target is too high ($\gtrsim 50$ kHz), losses from pileup become severe (Sect. 2.7f). On the other hand, small dimensions allow protons and electrons to escape from the crystal thus giving misleading information (see Sect. 3.11). The volume chosen was $\simeq 15$ cm^3 which gave priority to high counting rates and small probability of escapes; special attention had to be given to the exclusion of multiple scatters from the data.

2.3b Photon and neutron detectors

With high npB count rates as a priority, high efficiencies for the photon and neutron detectors were required, and thus large volumes. This, together with the need for PSD, restricted the choice to liquid or crystal scintillators for all three detectors.

The usage of a second stilbene crystal for the photon fulfilled the above requirements and the symmetrical geometry allowed the interchangeability of the crystals' function as described in Section 2.2. The two crystals were placed close together to minimise the solid angle between them which thus gave maximum photon total detection efficiency.

The size of the neutron detector was chosen for high efficiency consistent with good light collection. It was found, for large detectors of this type, that the PSD properties deteriorate if the light collection is poor, or significantly dependent on the position of the scintillation in the detector. The 250 cm^3 NE213 liquid-in-glass scintillator provided a neutron detection efficiency of $\simeq$ 0.3 over most of the observed energy range (Sect. 4.9) with acceptable gamma-separation by PSD.

The recoil neutron flight path was made as small as possible to maximise the solid angle for detection, although this caused a large uncertainty in the neutron energy as derived from time-of-flight. The mean neutron angle of $\theta_n = 35^0$ was the smallest that would allow for shielding from the neutron source. Without the shield, an intolerably high flux of random neutrons would be detected; the shield reduced this random rate by about 85%.

Finally, the stilbene crystal orientation results from the anisotropic photon distribution from npB. The angular distribution has a dipole pattern about the direction of the outgoing proton (Sect. 5.4) and since the proton recoil angle (θ_p) was selected as 25^0 (Sect. 2.3f) the orientation chosen maximised the photon detection efficiency with respect to this distribution.

2.3c Sources of background

A list of some possible background reactions in the target is given in Table 2.1. In isolation, these are of little concern, since we are detecting three-particle coincidences; however multiple scatters involving some of these reactions can give rise to intolerable background. Table 2.2 presents estimates of rates of some multiple scatter events as compared with npB.

Reaction	Q-value, MeV	Typical Total Cross-section	Ref.
$^1H(n,n)\,^1H$	-	1.6 b (5 MeV)	
$^1H(n,\gamma)\,^2D$	- 2.23	30 μb (14 MeV)	[14]
$^{12}C(n,n)\,^{12}C$	-	1.1 b (5 MeV)	[15]
$^{12}C(n,\gamma)\,^{13}C$	+ 4.95		
$^{12}C(n,n'\gamma)\,^{12}C$	thresh.: 4.8 for 2^+ state	225 mb (6 MeV)	[16]
$^{12}C(n,p)\,^{12}B$	-12.59		
$^{12}C(n,d)\,^{11}B$	-13.73		
$^{12}C(n,\alpha)\,^9Be$	- 5.70		
$^{12}C(p,\gamma)\,^{13}N$	- 1.94	38 μb (1.7 MeV resonance)	[17]

Table 2.1: Some possible reactions in the stilbene target.

Nucleus X		Lowest Excited State of X (MeV)	Relative Rate
^{14}N	if air in chamber	2.31	1
^{27}Al	if 0.2 mm foil between crystals	0.84	5
^{18}O	from light guides	1.98	0.1
^{12}C	if incident energy high enough, e.g. 14.6 MeV	4.43	50
^{13}C	if incident energy high enough	3.09	0.5
For comparison:			
	npB		1
	$^1H(n,n)\,^1H$ n-p scatters in det. 1. ↘1		10^9
	$^1H(n,n)\,^1H \rightarrow$ n-p scatters with neutron detected. ↘3 ↘1		10^7

Table 2.2: Estimated rates of some npB mimic reactions of the type $^1H(n,n)\,^1H \longrightarrow$ X(n,n'γ)X or X(n,n'γ)X $\longrightarrow\,^1H(n,n)\,^1H$ with the chosen geometry. Rates are relative to npB events where $d^2\sigma/d\Omega_p d\Omega_n$ is taken as 80 μb/sr^2.

Of particular concern for any detection system are those triple coincidence events which mimic npB. As an example, we consider an n-p elastic scatter, $^1H(n,n)^1H$, in which the scattered neutron undergoes an inelastic scatter from a carbon nucleus, $^{12}C(n,n'\gamma)^{12}C$ (see Fig. 2.3). The particles produced from this combination are n, p and γ and for certain scattering angles with the geometry chosen the event can cause a triple coincidence and pass the selection system as npB.

$E_\gamma = 4.5\,MeV$ $E_n = 2.1\,MeV$

$E = 14.6\,MeV$ 35° 19° $E_p = 8.0\,MeV$

TYPICAL npB EVENT

$E_\gamma = 4.4\,MeV$ $E_n = 2.1\,MeV$

35° ^{12}C

$E = 14.6\,MeV$ 48° 42°

$E_p = 8.0\,MeV$
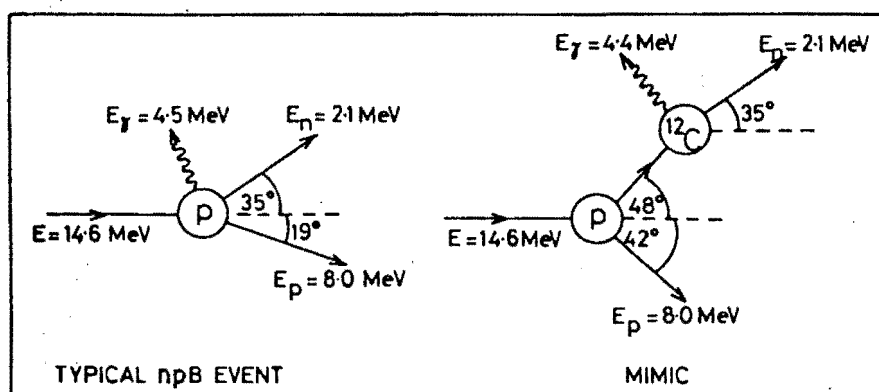
MIMIC

Fig. 2.3

Mimic event of the type $^1H(n,n)^1H \longrightarrow ^{12}C(n,n'\gamma)^{12}C$. The only observable difference between this and npB is the proton angle θ_p. (The missing 0.1 MeV in the mimic event is the energy of the carbon recoil.)

Multiple scatters will concern us frequently, so for convenience we adopt the notation $^1H(n,n)^1H \longrightarrow ^{12}C(n,n'\gamma)$ for the above combination where the small arrows indicate which detectors counted the scattered particles. A similar notation will be used for other combinations.

Also of importance are double coincidences involving any pair of the three detectors, in which the third detector counts a random particle. This type of background event is subtractable on analysis, but if present in sufficient numbers, it seriously reduces the accuracy of the npB cross-section being measured. An example of this type of event is $^1H(n,n)^1H \longrightarrow ^{12}C(n,\gamma)$ with a random particle in detector 3.

The detection system was designed to eliminate all possible npB mimics and to minimise subtractable background.

2.3d Incident neutron energy

Neutrons in the range 0-22 MeV were available using the usual (p,n) and (d,n) reactions with 0-6 MeV charged particles from the Van de Graaff accelerator at S.U.N.I. The energy of 4.8 MeV was chosen for the following reasons.

Firstly, the energy had to be high enough that PSD was effective for the

recoil particles. The experiment depended on good proton-gamma separation in the stilbene crystals and this was found to set a lower limit of $\simeq$ 1 MeV for protons or 0.25 MeV for Compton electrons with the PSD system used. For the neutron detector, where some gamma breakthrough could be tolerated, the limit was $\simeq$ 0.4 MeV. These considerations set a lower limit of $\simeq$ 3 MeV for the incident neutron energy since we required the photon and neutron detection efficiencies to be reasonably high.

Secondly, if the energy is below 5 MeV it is possible by suitable choice of the range of observation of the variables (Sect. 2:3f) to exclude mimics of the type $^{1}H(n,n)^{1}H \longrightarrow X(n,n'\gamma)$, where X is ^{12}C or ^{13}C. Furthermore, many of the reactions listed in Table 2.1 involving ^{12}C are then below threshold.

Finally, it was found that 4.8 MeV, using the D(d,n) reaction, was a satisfactory choice with regard to the purity of the source. Higher energies brought greater gamma contamination; in particular, the T(d,n) reaction which covers the range of 14 MeV and upwards, always produced additional lower energy neutron groups. A time-of-flight spectrum using a pulsed beam is shown in Fig. 2.4. There is no appreciable contamination from lower energy neutrons.
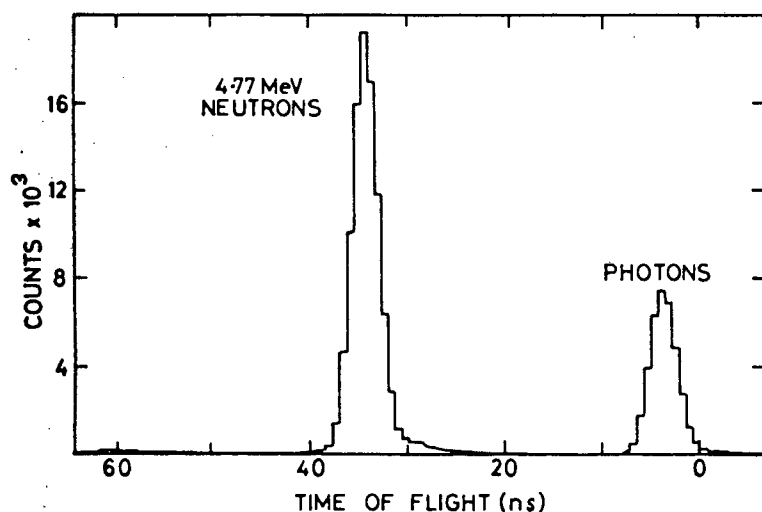
Fig. 2.4

Neutron source time-of-flight spectrum. Flight path = 1 m.

2.3e Detection system

In Sect. 2.1 we justified the use of a scintillator as target which detects its own recoil proton. The basis was that this overcomes the problem, at low energies, of low rates associated with a thin target and separate proton detector. The selectivity afforded by Harvard geometry is thus not available with this method as the proton angle is unknown.

We now mention a preliminary experiment at 14.6 MeV in which an anthracene target/proton detector was used (Fig. 2.5), the object being to make use of the
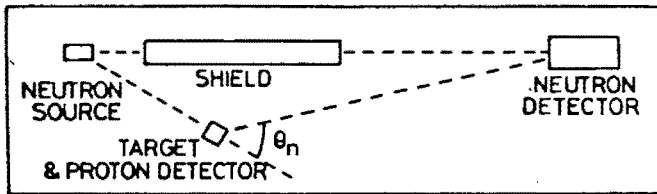
Fig. 2.5

Experiment using pulse-shape anisotropy to determine θ_p.

pulse-shape anisotropy (PSA) properties of anthracene [18] to determine the proton direction. The incident energy of 14.6 MeV was taken as the lowest for reasonable angular resolution by PSA, which improves as the energy increases [18]. However, at this energy or above, mimic events of the type $^1H(n,n)\,^1H \longrightarrow ^{12}C(n,n'\gamma)\,^{12}C$ can occur and it was found that the angular resolution was insufficient to distinguish these from npB; also a large amount of random background was allowed. The outcome of this experiment was an upper limit to $d^2\sigma/d\Omega_p d\Omega_n$ of the order of 3 mb/sr^2 (expressed as for Harvard geometry) for $\theta_p, \theta_n = 25^0, 30^0$, which was considered a poor result.

With the failure of this experiment, other methods of improving selectivity were investigated and the only viable solution found was the inclusion of a third detector for the photon.

2.3f Ranges of observation

The following restrictions applied to the variables:

i) $E_p > 1$ MeV, $E_n > .4$ MeV, $E_\gamma > .4$ MeV to enable effective PSD in the detectors (see Sect. 2.3d).

ii) $E_p + E_n \ll 4.8$ MeV, otherwise elastic n-p scatters, e.g. $^1H(n,n)\,^1H$ with a $\underset{3}{} \underset{1}{}$ random photon in detector 2, cause a heavy background. This can be seen in the reduced data, e.g. Fig. 3.10a and b.

iii) The neutron detector (detector 3) must be shielded from the source and this set a lower limit to the mean neutron angle at $\theta_n = 35^0$.

The region chosen was defined on the $\theta_p - \theta_n$ plane, and this led to the observed $E_p - E_n$ region shown in Fig. 2.6, as derived from npB kinematics (Appendix A.1).
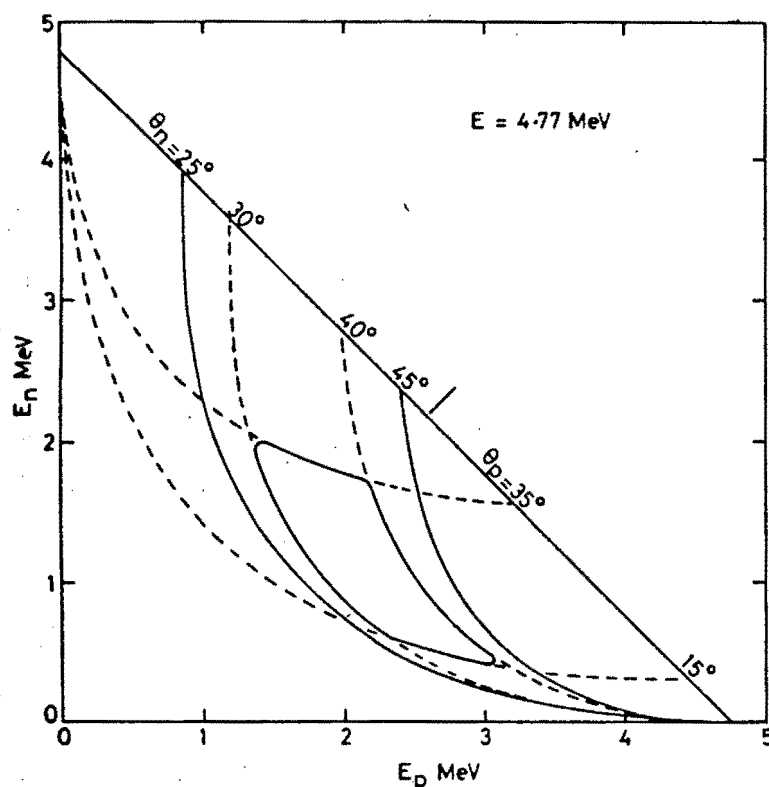
Fig. 2.6

$E_p - E_n$ regions allowed by kinematics. The region defined by the neutron detector is between the lines $\theta_n = 25^0$ and 45^0. The region chosen for observation is bounded by $\theta_p = 15^0$ to 35^0, $\theta_n = 30^0$ to 40^0.

2.3g Helium chamber

The problem of npB mimics of the type $^1H(n,n)^1H \longrightarrow X(n,n'\gamma)X$ has been raised in Sect. 2.3c for the case where $X = {}^{12}C$, and was eliminated in this case by suitable choice of incident energy. However, if there are nuclei in the vicinity of the target with excited states below $\simeq$ 2.3 MeV (1.8 MeV maximum observed E_γ + 0.5 MeV added for neutron energy resolution), then this mimic can occur. Some estimated rates appear in Table 2.2. In order to remove this problem, offending materials were avoided in the detector construction (Sect. 2.5) and the targets were surrounded by Helium in a cylinder 30 cm × 30 cm diameter to exclude air.

A mimic event of the above type, where X is on the periphery of the chamber, is shown in Fig. 2.7. The size of chamber and the coincidence requirement between the signals from detectors 1 and 2 (1.14 ns, Sect. 3.10) meant that, if X is outside the chamber, the mimic was removed due to the different flight times for n' and γ.
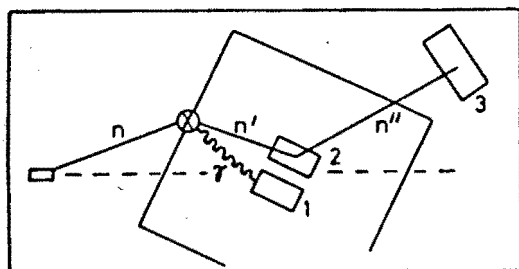
Fig. 2.7

Mimic event of the type $X(n,n'\gamma)X \longrightarrow {}^1H(n,n)^1H$, where X is on the periphery of the chamber.

2.4 NEUTRON PRODUCTION

Neutrons of 4.8 MeV were produced using the $^2D(d,n)\,^3He$ reaction with $\theta_n = 0^0$, and with the target in gaseous form at $\simeq 1.4$ At. absolute pressure. The gas cell was 3 cm × 1 cm diameter and had a Havar window and platinum beam stop. The cell was air-cooled.

The incident deuterons were in a D.C. beam at 2.2 MeV. The loss in the cell window (3.52 mg/cm^2) was calculated as 0.48 MeV giving a deuteron energy range in the cell of 1.42 to 1.72 MeV. This led to neutron energies between 4.60 and 4.94 MeV with a mean of 4.77 MeV, as confirmed by time-of-flight analysis (Fig. 2.4), and the energy distribution over this range was flat within ± 15%. The deuteron current varied slowly over the runs having a mean value of 1.0 μA and producing a forward neutron flux of typically 4×10^7 sr^{-1} s^{-1}.

The forward angle was chosen for zero polarization. One beneficial aspect of this is that the D(d,n) differential cross-section at 2.2 MeV incident energy is forward peaked and falls off to 50% at $\theta_n \gtrsim 25^0$, thus eliminating some random background.

Beam pulsing at 2×10^6 Hz was available but was not used as it was found to cause a large increase in the rate of coincidences involving random counts.

2.4a Choice of target

An alternative to the gas cell was a solid target, e.g. deuterated polyethylene. This was not used as the presence of other nuclei causes a broader distribution of neutron energies, and the required neutron flux could not be obtained with a static target due to local heating.

A variation in the cell design which was tested was the replacement of the platinum beam stop by another Havar window so that the air would act as beam stop with a possible reduction in gamma production. Indications were that the gamma production was marginally greater for this case.

2.4b Associated particle method

This method, which was considered but not used, employs a detector for the recoil ^3He ion from the D(d,n) reaction in coincidence with the other detectors, the effect being to define a neutron 'beam' (see e.g. [19]). In this way, only events for which a neutron has left the source in the direction of the target will be passed.

This system was used in the Zagreb experiment [11] to avoid counting events where the scatter did not occur in the target. In our case, using target as proton detector, the only purpose served would be to eliminate events in which the incident neutron did not travel direct from the source. Since this type of event was anyway highly improbable, the system could be of little value.

2.5 HELIUM CHAMBER AND DETECTOR CONSTRUCTION

The helium chamber was constructed from galvanised iron and could not stand high pressures and was not leak-tight. In order to maintain the helium atmosphere, a continuous purge of gas was supplied at 20 ℓ/hr and the pressure was kept at 50 mm w.g.

In an effort to avoid elements in the detectors other than C, H, O, the light sheaths were made from filter paper (cellulose) coated with colloidal graphite instead of the more conventional aluminium foil and TiO_2 reflector paint. The light guides were perspex (polymethyl methacrylate) and paraffin oil was used to couple crystal to guide. A 1.2 mm wax (CH_2) disc was set in between the crystals to prevent protons escaping from one crystal to the other.

2.6 STILBENE DETECTOR CIRCUITRY

Three separate signals from detectors 1 and 2 were required, a fast pulse (T) for timing, the pulse-height (L) for particle energy, and a signal related to the pulse-shape (S) for particle discrimination (PSD). The circuit of Fig. 2.8 was built into the RCA 6810 A photomultiplier base and contains the dynode voltage supplies and the T, L, S outputs.

2.6a Pulse-shape discrimination and 'S' output

The pulse-shape from organic scintillators has been amply discussed elsewhere (e.g. [13]). For the present purposes, the light output can be considered as the sum of two exponential components which, for stilbene, decay with time constants of 6 and 370 ns [20]. The fast component contains most of the light, and the ratio of the amplitudes of the two components depends on particle type, with heavy particles having a greater proportion of slow component.
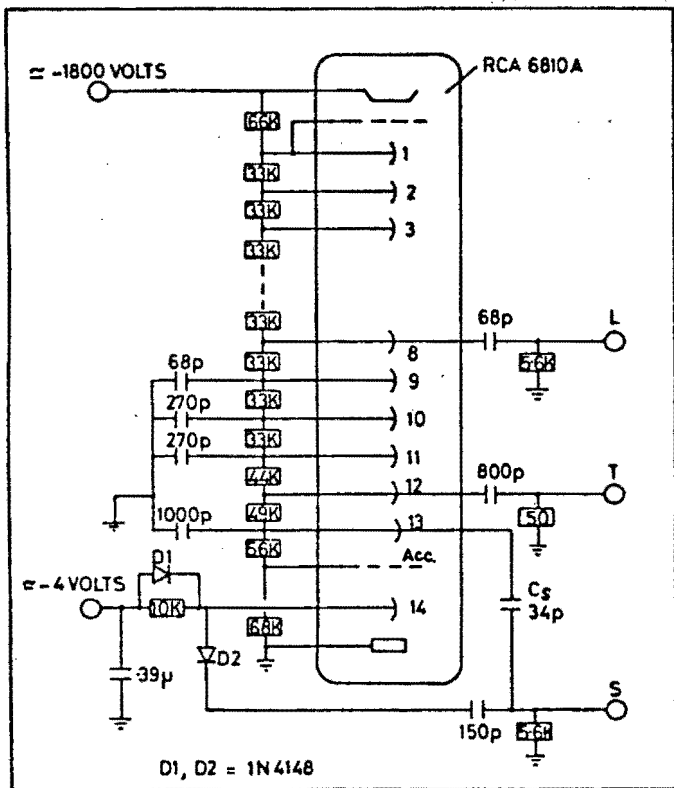
Fig. 2.8

Photomultiplier circuit.

The S output was provided by a simple passive circuit relying on space charge saturation in the region of the last dynode (dynode 14) in a manner first reported by Owen [20]. The value of S can be considered as approximating to the integral of the slow component and the operation is as follows.

Dynode 14 is held at $\simeq$ -4 volts with respect to the anode instead of $\simeq$ -200 volts for normal working. As a result, the leading edge of the pulse for all but the smallest signals causes a buildup of space charge around dynode 14 which inhibits the fast component. When the fast component has passed, the space charge is absorbed by the anode and dynode 14, and diodes D1 and D2 prevent the formation of a negative pulse at the S output. With the space charge now dissipated, the remainder of the signal, having insufficient amplitude to cause space charge saturation, causes a positive pulse on dynode 14 in the normal way which passes to the output through D2. The nett effect of the space charge is thus to clip off the early part of the signal.

The capacitor C_S was provided after trials had shown that the S pulse for low energy electrons was below the LGS bias level (see Sect. 2.7d). This, in itself, did not detract from the discrimination, but in the analysis, events with zeroes on any parameter were rejected. C_S provided a small positive addition to the S pulse.

The S output was evidently energy dependent as the amount of space charge and thus the time taken for it to dissipate depended on the amplitude of the

fast component. Because of this, the particle separation in the analysis had to be effected by means of cuts on the L-S plane (Sect. 3.4, Fig. 3.1). The voltage setting on dynode 14 was critical in that it determined which part of the signal was passed to the output; the setting was chosen to maximise the separation. The high counting rate ($\lesssim$ 50 kHz) was found to cause no problems once dynode 14 had been decoupled from the voltage divider chain (Sect. 2.6d).

Since PSD was important to the success of the experiment, other systems were tested and the above selected as the best performer. The zero-crossing method (e.g. [21]), where S was taken as the time between the T pulse and the point at which a differentiated form of the L pulse crossed the baseline, was found to give worse separation at low energies. Since the experiment, faster electronics have become available [22] and a new evaluation may reverse this result. Zero-crossing PSD was used with success on the neutron detector where separation was not so critical.

Faster and more efficient photomultipliers than RCA 6810 A are now available (e.g. RCA 8850, RCA C31024) and the use of these could lead to improvements [23].

2.6b 'L' and 'T' outputs

The L output was taken from an early dynode as it was important that the space charge at the anode end of the tube should not affect the pulse-height. On the other hand, the T output had to be a high amplitude pulse with little regard for linearity, hence the choice to take this from dynode 12.

2.6c Output time constants

The time constants at the L and S outputs were small to facilitate fast pulse decay and minimise the incidence of pileup. For the L output, this means that the total integral of the signal was not taken, but most of the energy is contained in the fast component and the pulse-height responses were not materially affected. The 50 ohm load resistor at the T output was for impedance matching.

2.6d Dynode voltage supplies

The potential divider provides voltages for the dynodes in similar ratios to those recommended by the tube manufacturer except for dynode 14. With a view to voltage stability, the resistors in the chain were of low value consistent

with the avoidance of excessive heating.

When a signal travels through the tube, the voltage at each dynode is pulled positive by the secondary emission as the signal passes, with the effect increasing towards the anode end. The gain of the later dynodes then changes in a complex way during the leading, high amplitude portion of the signal and can cause severe distortion of the pulse shape. Blocking capacitors were thus used on dynode 9 onwards and their values were chosen generally in accordance with criteria given by Kowalski [24]. The capacitors serve to hold the voltages steady during the passage of a pulse. This unfortunately means that the voltage distribution takes a finite time to restabilize after a pulse, $\simeq$ 100 μs with the capacitors used. If, then, an event follows a previous one within this order of time, the L pulse will be increased, and the S pulse changed in an unpredictable way. The event rate at the stilbene detectors was typically 40 kHz giving a mean pulse separation of 25 μs.

Fig. 2.9 shows the average voltage distortion at 30 kHz measured for a circuit similar to that used (Fig. 2.8) but with dynode 14 drawing its supply from the chain. It appears that dynode 13 is mainly responsible for the voltage changes, and the mean increase in gain to dynode 8 (L output) can be calculated from the curve to be 2%. This leads to a standard error of ± 0.5% for L from this source. Since this is considerably smaller than the spread in L from other sources (Sect. 2.9f) it is not surprising that an attempt to narrow the L and S spreads by supplying dynode 13 separately showed no noticeable improvement.
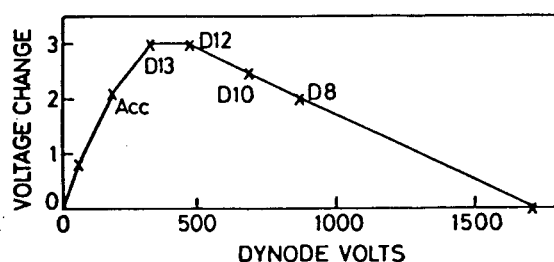
Fig. 2.9

Dynode voltage distortion. The graph shows how the average voltages increase from the static values when counting at 30 kHz.

On the other hand decoupling and supplying dynode 14 separately gave considerable improvement in the width of both L and S at usual rates of 40 kHz. This is presumably due to the complex variations in current through dynode 14 which accompany the space charge effects. The method of testing in each case was to measure the spread in L and S of the high energy proton recoils from monoenergetic neutrons.

2.7 ELECTRONICS

The circuit for processing the detector signals and providing the required digital information to the on-line computer (PDP15) is shown in Fig. 2.10. The circuit logic provided that only triple coincidence events were passed; that is, events in which all three detectors fired, with the further condition that the particle discriminator on the neutron detector (detector 3) had indicated a neutron. The information produced per event was: pulse heights from all three detectors (L_1, L_2, L_3); pulse shape parameters from detectors 1 and 2 (S_1, S_2) times between signals from detectors 2 and 1 (T_1) and detectors 1 and 3 (T_2); one bit indicating a pileup condition at either of detectors 1 or 2.

The features of the circuit are discussed in the following. Particular attention went into handling high detector rates with a view to minimising deadtime loss and avoiding wrong information from detector signals not belonging to the event being processed but close to it in time. As we were searching for so few events (1.5 events nett were counted after analysis (Sect. 3.14)) any slight malfunction or misalignment in the electronics could have led to severe errors in the result. In this connection, the synchronisation of the various pulses (Sect. 2.7b) and the use of efficient pileup rejection (Sect. 2.7f and g) were of great importance.

2.7a Coincidence logic

Fig. 2.11 indicates the order of event selection. Outputs from TAC 1 signalled a coincidence between detectors 1 and 2 within the set time range. The true-stop output, via a TFA unit to invert the logic pulse, served to start TAC 2, the stop input for this unit being from detector 3. An output from TAC 2 thus indicated a triple coincidence. The SCA output from TAC 2 was passed through the n-γ discriminator on detector 3 (TAC 3 and associated units) and an output from this indicated an accepted event. Since the time range on TAC 1 was larger than required, this range was restricted by combining TAC 1's SCA output with the accepted event signal in an AND gate. The output from this then opened the ADC gates via TAC 4 (see Sect. 2.7b) to pass the event.

This logical order was designed to minimise deadtime. All the TAC's have a minimum reset period of 2.1 µs after an accepted start during which no further inputs are accepted. The count rates at the detectors were typically 40 kHz (detectors 1 and 2) and 75 kHz (detector 3), giving mean count separations of

EXPERIMENTAL AREA

CONTROL AREA

EHT-1700V →
D14-5·02V →
6810A 1

6810A 2
EHT-1900 →
D14-3·85V →

EHT-1700V →
TIME PICKOFF BIAS 1·0
BASE 271
58AVP
NEUTRON DETECTOR 3

L S T

×100

AMP 203 GAIN 300

AMP 450 GAIN 90

AMP 203 GAIN 250

AMP 450 GAIN 140

ARC 1 GAIN 5 BIAS ·15

PILE UP 3 µs

ARC 2 GAIN 5 BIAS ·60

S_5

AMP 203 GAIN 41

DELAY 1 µs

DELAY 1 µs

S_1 32ns $\bar{P}$ S_2

326 ns

DEL O/P

STOP   STRT

TFA τ_f=10ns τ_6=5ns   STRT

STOP

S_3 TRUE STRT

TAC1 50ns LLD1 ULD7

TRUE STOP STROBE

LSD2 DEL 34 µs

TAC 2 200 ns LLD ·2 ULD 6·2

SCA   TAC

STROBE

SCA

B   A

COINC

LSD1 DEL 2·2 µs

LSD 5 DEL ·1 µs

TSCA BIAS ·12

n-γ Discriminator

S_4

S_6

STRT STOP

TAC3 200 ns

LSD3 DEL 23 µs WID. 2 µs

50   50

AND GATE

TAC

INT DISC

50

LGS1 442

LGS2 442

LGS3 1454

LGS4 442

STRT

TAC4 4 µs

S_7 PERIOD

LSD4 DEL 2 µs

GATE

XY SCOPE

L1   S1   L2   S2

50

TRUE STRT

S_8

T2

L3

ADC1 ND

ADC2 ND

ADC3 ND

ADC4 ND

Computer input Register

ADC5 LECROY

ADC6 ND

ADC 8 ND

1   2   3   4   7   5   6   8

PU   T1

Fig. 2.10

Electronic circuit (see Index, page 20)

1. INDEX

AMP 203	:	Linear amplifier, Tennelec 203.
AMP 450	:	Linear amplifier, Ortec 450.
DELAY	:	Delay amplifier, Canberra 1457.
LGS	:	Linear gate and stretcher, Ortec 442 or Canberra 1454.
BASE 271	:	Constant fraction timing base, Ortec 271.
ARC	:	ARC timing discriminator, Canberra 1427.
PILEUP	:	Pileup gate, E.G. & G. GP100/N.
TAC 1,2	:	Time-to-amplitude converter/single channel analyser, Ortec 467.
TAC 3,4	:	Time-to-amplitude converter, Ortec 437A.
LSD	:	Logic shaper and delay, Canberra 1455A.
TFA	:	Timing filter amplifier, Ortec 454.
TSCA	:	Timing single channel analyser, Ortec 420A.
INT DISC	:	Integral discriminator, Ortec 421.
GATE	:	Linear gate, Canberra 1451.
COINC	:	Coincidence unit, Canberra 1446.
ADC	:	Analogue to digital converter, Nuclear Data 880303 or Lecroy.
∇	:	Preamplifier, Nuclear Enterprises 5283.
-\/\/\-	:	Delay line.
[S]	:	Scaler.
⊥∖50	:	50 ohm termination.
∕	:	Gate input.

2. ADJUSTMENTS

Some critical settings are shown in the figure; and the following adjustments were generally used:

All units D.C. coupled
No baseline restoration used } where applicable.
D.C. levels to zero
Time constants on all amplifiers set to 0.25 µs.
L.G.S. bias levels: 200 mV (see text).
A.D.C.'s { bias between noise and 200 mV.
zero offsets slightly positive.
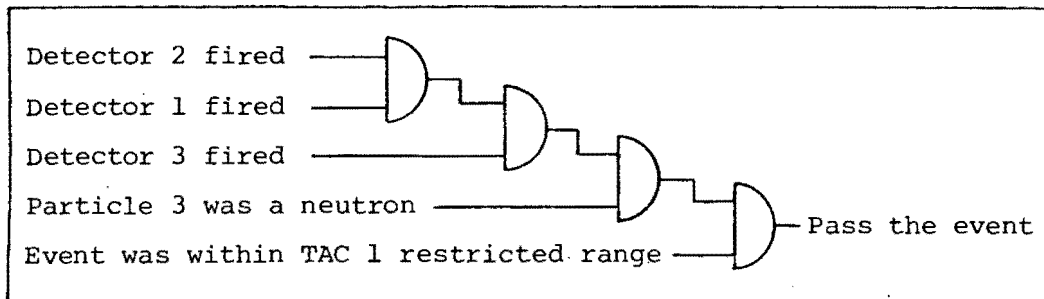
Fig. 2.11

Logical order of event selection.   The process was initiated by a signal from detector 2 which had the lowest rate of the three.   The above order then minimised event losses due to deadtime.

25 μs and 13 μs respectively and thus a high probability of event loss in the wrong circuit.   For this reason the detector with the lowest rate (detector 2) was used to start the sequence and the only point at which deadtime could occur was at TAC 1.   Events passed by this unit must have been separated by at least the unit's turnaround time of 11 μs (Fig. 2.12) and the start signals to the other TAC's would thus always be accepted.   The deadtime loss was typically 10%. part of which would anyway have been lost by the pileup rejection system (Sect. 2.7f, Appendix D).

2.7b Synchronisation

The main gate signals were all synchronised to the T pulse from detector 1, and Fig. 2.12 shows a timing diagram in which the stop input to TAC 1 is taken as zero.   The gate input to the ADC's, showing acceptance of an event, only arose after 3 μs, and all analogue signals to the ADC's had to be delayed so as to rise simultaneously and only after the gate.

LSD 1, fed from TAC 1 true stop and hence synchronised to the stop input, provided the linear-gate-and-stretcher (LGS) gate signals.   Unfortunately, due to availability of equipment, two varieties of LGS unit were used, Ortec 442 (L_1, S_1, S_2) and Canberra 1454 (L_2) and these have different internal logic. The 442 stretches and outputs the first peak above its bias level to arrive after the gate, whilst the 1454 stretches all peaks above bias (provided it is not busy) and the gate merely enables the output.   LSD 1 was set so that the LGS gates opened ≲ 100 ns before the signal peak thus using the 442 logic to minimise wrong pulse identity.   However, the 1454 could derive no benefit from
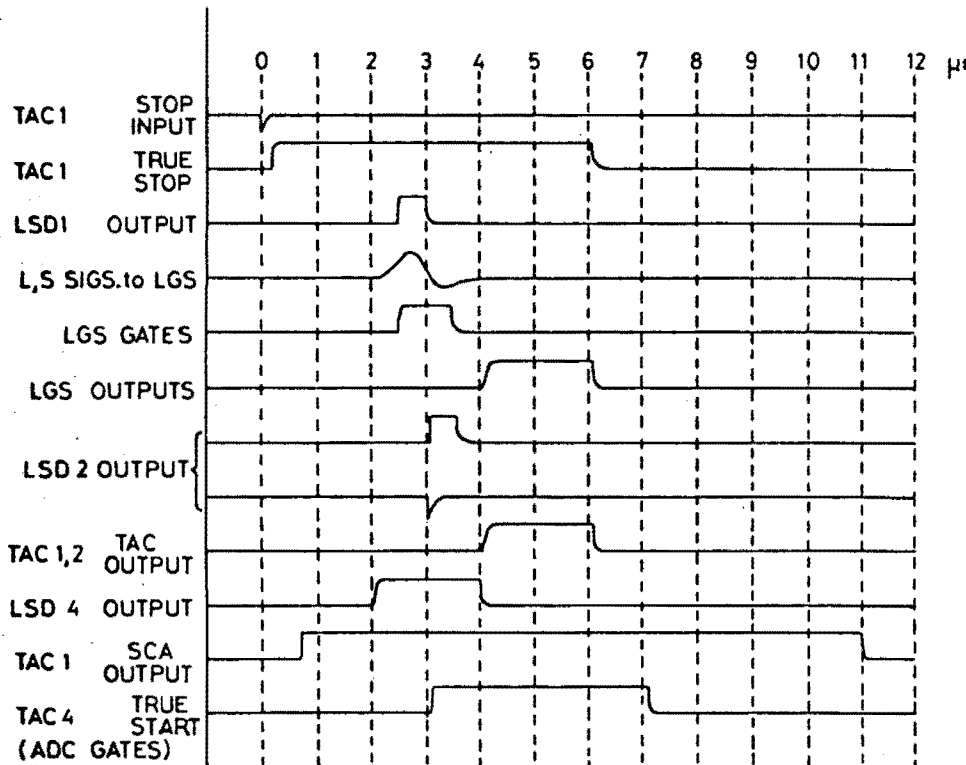
Fig. 2.12

Timing diagram for accepted event.

this precise timing as any previous signal which, at gate time, had not decayed below bias, would be outputted. The result of this only came to light in the analysis, where a few L_2 points were found to be erroneously high, and this caused the loss of a quarter of the data (Sect. 3.10a).

LSD 2, fed also from TAC 1 true stop, provided a signal which, through TAC 4, opened the ADC gates for a passed event. TAC 4 was not used for its normal function; its purpose was to furnish a positive logic pulse (true-start output) from a fast negative input (start input) with gate facility. Its particular value here was that the timing of the output was unconditionally linked to the input with no possible dependence on the timing of the gate. This was important as otherwise the timing of the count in detector 3 would have caused the ADC gate opening time to vary. No other available unit had this feature.

LSD 2 also provided the strobe input to both TAC 1 and TAC 2 and the internal delay on the TAC's ensured that their outputs were conveniently within the ADC gate period.

2.7c Stilbene detector timing signals

The coincidence timing between detectors 1 and 2 was critical, and Canberra 1427 ARC timing units were selected after trials against another unit, Ortec 463, as providing the most stable and walk-free time pickoff. Both units employed the constant fraction of pulse-height trigger (CFPHT) system [25]. The timing

resolution as measured using a ^{22}Na source between the stilbene crystals was 1.8 ns FWHM. This improved to 1.2 ns when the crystals were replaced by 2.5 cm × 1.5 cm diameter plastic scintillators. This width is attributed to photomultiplier transit time spread and non-uniform light collection.

2.7d Stilbene detector 'L' and 'S' outputs

The L and S pulses had to be amplified, delayed, and suitably shaped for input to the ADC's. Time constants on the linear amplifiers (Ortec 450 or Tennelec 203) were set low at .25 μs to minimise pileup, and different internal delays in the 450 and 203 were corrected by delay amplifiers following the 450's. The LGS's were used as their internal logic helped to prevent wrong pulse identity (apart from L_2, see Sect. 2.7b) and they provided suitable pulse shapes for the ADC's. Due to the method of output coupling in the photomultiplier base, outputs from the linear amplifiers were bipolar and not compatible with the ADC's; LGS units ignore the negative part of the pulse.

LGS bias levels were set at about 200 mV, slightly above the levels on the ARC units, as a lower setting would have caused loss of events due to deadtime.

2.7e Neutron detector signals

The neutron detector used a manufactured base (Ortec 271) which, in conjunction with a pickoff unit (Ortec 403A), provided a preamplified linear output (L_3) and a fast timing pulse (T).

The PSD system used the two signals in a zero-crossing system (see Sect. 2.6a). The zero-crossing point of the bipolar output from the L_3 amplifier was identified by a TSCA (Ortec 420A), and the interval between this point and a delayed T was measured by TAC 3 (Ortec 437A). The TAC output (S_3) was displayed against L_3 and n-γ separation optimised by walk adjustment on the TSCA. It was then possible to remove most of the gammas by a straight cut on S_3 (integral discriminator).

2.7f Pileup and pulse-pair rejection

Typical L and S pulse shapes from the stilbene detectors taken after the shaping amplifiers are shown in Fig. 2.13. In spite of efforts to keep the pulses short by using small time-constants throughout, there is still an appreciable probability of pileup with the high counting rates. If, for instance, two S-pulses are separated by 1 μs, then the second pulse-height will

be erroneously low due to the addition of part of the first pulse. On the basis of the observed shapes, it was arranged that a pulse be rejected if it occurred within 2.4 µs of a previous one.
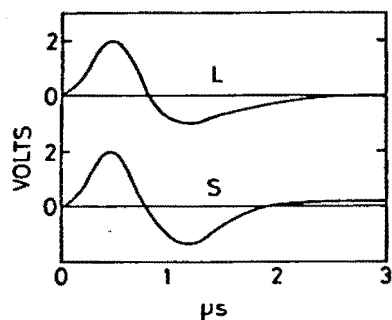
Fig. 2.13

Typical pulse shapes after linear amplifiers. Pileup occurs when two pulses are too close, such that the second pulse height is wrong due to the addition of the tail of the first pulse.

If two pulses are very close, the first pulse-height may also be wrong due to the addition of the rise of the second pulse. In this circumstance both were rejected (pulse-pair rejection). The pulse-pair interval was set at 0.6 µs making a total rejector set period of 3 µs.

A measure of pileup rejection is afforded at the start input (from detector 2) of TAC 1 by its deadtime. Every accepted start signal holds the TAC busy for 2.1 µs during which time no further starts will be accepted. However, a signal received during the busy period, although itself rejected, cannot update the busy period, and some pileups would thus be passed (see Appendix D). Besides being an imperfect pileup rejector, pulse-pair rejection cannot be achieved, and no protection is provided at the stop input. As a result, a separate unit, pileup gate E.G. & G. GP 100N, was used to fulfil all the necessary functions for both detectors 1 and 2.

The circuit was so arranged that a pileup or pulse-pair condition on either detector for a particular event was passed to the computer as a single bit along with the rest of the information for the event. The actual removal of pileup events was done in the data analysis (Sect. 3.10).

Losses from pileup and pulse-pair rejection (over and above the TAC 1 deadtime loss) varied according to count rates, having an average over all runs of 20%; equations for predicting loss rates for this system are derived in Appendix D. Fig. 3.1d demonstrates the effectiveness of the system.

2.7g Pileup rejection, detailed functioning

The pileup gate, GP 100 N, has two looping inputs which were fed from the stilbene detectors, and the output used ($\overline{P}$) remains positive until a pileup is sensed. If two pulses arrive at either input within the set period, τ_p (3 µs),

the output falls to zero $\simeq$ 75 ns after the second pulse and remains so for the set period.   If further pulses are received during this time, the internal timer updates and holds the output down for τ_p from the last pulse received.

Since all accepted events are T_1 coincidences between detectors 1 and 2, the unit would thus seem to condemn all useful data.   Fortunately, pulses closer than 6 ns were not resolved, and the events finally selected in the analysis (Sect. 3.10) were T_1 coincidences within $\pm$ 1.14 ns, and were therefore not seen as pileups.   Cable lengths between the ARC discriminators and the pileup gate were adjusted so that simultaneous counts at detectors 1 and 2 gave rise to simultaneous signals at the pileup gate inputs.

For every T_1 coincidence, the output state of the pileup gate was tested. This was achieved by combining the SCA output from TAC 1, which signals a T_1 coincidence, with the pileup gate output in a coincidence unit (Canberra 1446). This unit operates basically as an AND gate except that one input (from SCA) is internally shortened to 100 ns.   With an output from this unit, LSD 3 produced a signal, delayed to coincide with the ADC signals, which was then digitised in the computer input register.   Pulse-pair rejection of about 0.6 μs was accomplished automatically because the TAC 1 SCA output only rises 0.7 μs after the stop input.   This is best explained by examples as follows.

Fig. 2.14a shows a case of pileup rejection.   A T_1 coincidence at t=0 gave rise to a TAC 1 SCA output (test pulse) which rose at t=0.7 μs.   However, the coincidence was preceded by a pulse in detector 2 at t=-2 μs which caused the pileup gate output to be down when the test pulse arrived.   No output to the computer was generated.

Fig. 2.14b shows a passed event.   In this case, the event was followed by
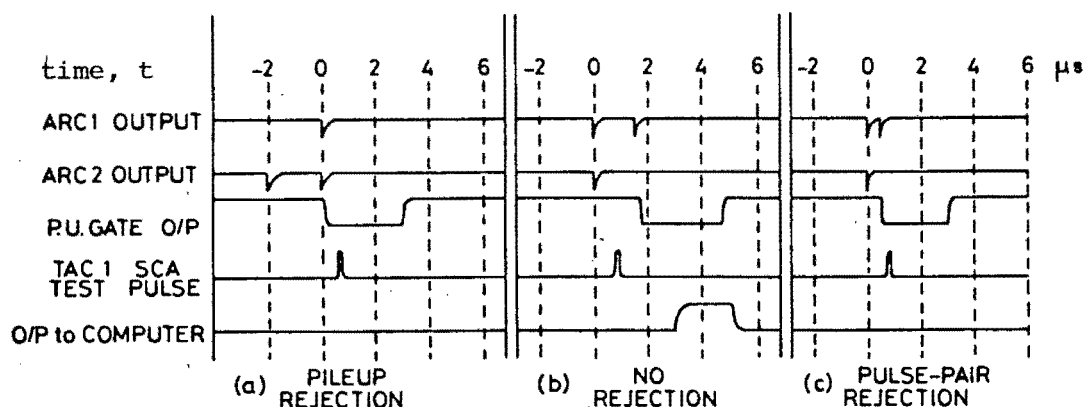
Fig. 2.14

Examples of pileup rejector operation.   A T_1-coincidence (shown here at time = 0) will only pass if there were no signals in either detector within 2.4 μs prior to the event, or within 0.6 μs following it.

a pulse at t=1.5 μs in detector 1, beyond the pulse-pair rejection period. The test pulse arrived at a time when the pileup gate output was positive and an output was produced. Fig. 2.14c shows the same situation, but the second pulse occurred at t=0.5 μs, within the rejection period. No output was generated.

2.8 DATA COLLECTION

The digitised information for each event was fed to an on-line computer (PDP 15) whose main purpose was to stack the events into blocks and record on magnetic tape. All data analysis was then done off-line. The acquisition program had a facility for active display of any pair of parameters; this was used together with the scalers (Fig. 2.10) to monitor the system whilst running.

The data was acquired in ten runs of typically 12 hours over about 8 days, giving a total of 125.9 hours' useful running time. The geometry (Sect. 2.2) and electronics (Sect. 2.7) were kept standard throughout. The various calibration data (Sect. 2.9; 2.10) were collected between runs. In particular, before and after each run, the pulse-height spectra, L_1 and L_2, and time coincidence spectra, T_1 and T_2, were recorded to monitor drifts. These were present on L_1, L_2 and T_1 and were corrected in the analysis (Sect. 3.5) using the recorded information.

2.9 PULSE-HEIGHT RESPONSES, DETECTORS 1 AND 2

The response curves for detector 1 for protons and electrons are shown in Fig. 2.15 together with the relationship of minimum gamma energy (E_γ) to L.
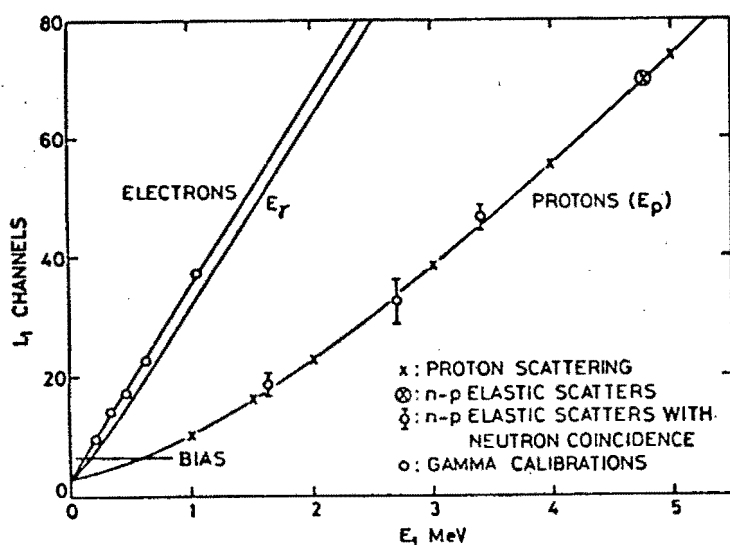
Fig. 2.15
Response curves for stilbene detector 1 at run 4. The E_γ curve is the minimum photon energy (see text).

As the method of gamma detection relies on Compton scattering, the exact gamma energy for an event cannot be obtained from L and only the minimum energy can be found. These calibration curves, and similar curves for detector 2 were drawn from information obtained as follows.

2.9a Pulse-height zero

Zero offsets were present in the electronic apparatus, and the channel number at zero energy had to be found.

The pulse-height for organic scintillators for electrons is proportional to the particle energy for the range of energies involved (0.2-5 MeV) [13]. The zero was thus found using 5 points from γ-sources, ^{22}Na (2 points), ^{54}Mn, $^{137}C_s$, $^{133}B_a$. For each point the channel number taken was at 90% of the peak pulse-height at the Compton edge (Fig. 2.16a) following Knox and Miller [26] and the corresponding electron energy, T_1 calculated from $T = 2E_\gamma^2/(.511 + 2E_\gamma)$.

A straight line was then drawn through the points by the least-squares method, and the intercept on the L axis gave the required zero point.
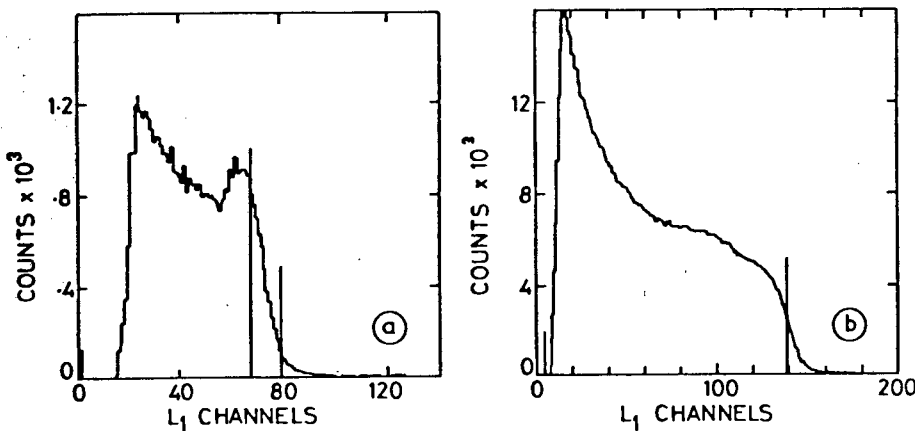
Fig. 2.16

Detector 1 spectra.

(a) $^{137}C_s$ gammas. Positions shown are 90% of the Compton edge for the electron calibration, and 10% for the E_γ curves.

(b) 4.8 MeV neutrons. The position shown is taken as corresponding to forward proton recoils.

2.9b Gamma response

The spectra from the above γ-sources were used to draw the gamma response curve by relating E_γ to the channel number at 10% of the Compton peak (Fig. 2.16a). It was found that $\gtrsim$ 99% of the total distribution lay below this point; E_γ is thus the minimum gamma energy, and was used in applying conservation of energy (Sect. 3.7c; 3.9).

2.9c Proton response

Three sources of information were used for the proton responses:

i)   The L distribution for elastic n-p scatters in the crystal was recorded at
     4.8 MeV and 7.9 MeV.   The channel number at the half-height at the edge
     of the distribution was taken as corresponding to forward proton recoils at
     these energies (Fig. 2.16b).

ii) In an independent experiment, the response was measured directly by
     scattering protons of 1-5 MeV from a gold foil into the crystal (Sec. 2.9e).

iii) The L distribution for elastic n-p scatters was recorded with the recoil
     neutron detected in coincidence as in the main experiment. Three points
     were obtained with $E = 4.8$ MeV, θ_n(mean) $= 34^0$ and 60^0; $E = 7.9$ MeV,
     θ_n(mean) $= 34^0$.   Time of flight information was used to restrict the
     range of neutron recoil energies and thus narrow the proton peak.   However,
     owing to the size of the neutron detector, the proton energy was still not
     well defined and the information from this method was only used to confirm
     that from i) and ii) above.

2.9d Pulse-height anisotropy

The response of organic scintillators to protons and heavier ions depends
on the direction of the ion relative to the crystal axes [18].   The orientation
in the experiment was chosen so as to minimise the variation in L for the
accepted range of npB recoil proton angles using the results of Jones [27] for
stilbene-2.   No orientation information was available for stilbene-1 but the
relative axes of the two crystals were found by comparison under a polarizing
microscope.   Jones' results imply that, for the low proton energies involved,
the pulse-height variation is small;   this is also the conclusion from the
proton scattering experiment (Sect. 2.9e) and the effect is hereafter disregarded.

2.9e Proton scattering experiment

Protons of 1-5 MeV were scattered through 90^0 in the apparatus of Fig. 2.17 and
the positions of the highest-energy peaks of the resulting spectra are plotted
in Fig. 2.18.   Corrections were made for zero offset and the energy of the
recoil gold nucleus, and the curve is normalised so that the electron response
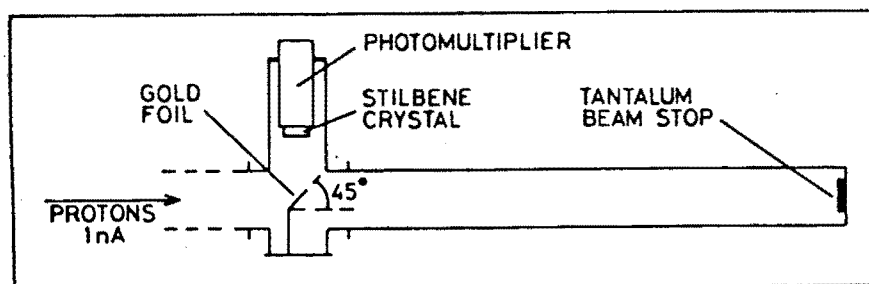
Fig. 2.17

Apparatus for proton
scattering experiment.

is the same as that from the n-p scatter calibrations (Sect. 2.9c; i) and iii)).
The electron response was measured in the same way using γ-sources.

This method may not provide an exact absolute calibration of the proton
response as in the main npB experiment for the following reasons:

i) surface effect; the particles are all detected on the front surface of the
    crystal, whereas with n-p scatters, the 'incident' protons are distributed
    throughout the crystal. The variation of light collection efficiency with
    position in the crystal will cause different responses;

ii) pulse-height anisotropy; the protons are all incident at or near the angle
    of minimum response;

iii) foil thickness; no correction was made for energy loss in the foil.

All these effects would lead to a lower average response as compared with n-p
scatters. However, the results from the 2 methods for 5 MeV protons agree to
within 1% and it is concluded that all three effects are negligible.

2.9f Proton energy resolution

The widths of the peaks in the proton scattering experiment were used to
obtain a figure of 0.2 MeV as the standard deviation of the proton energy
measurement over the observed range. This was confirmed by the width of the
tail on the n-p scatter calibration spectra (Sect. 2.9c; i)). In this case an
additional spread was observed resulting from the uncertainty in incident energy
(± .17 MeV).

2.9g Comparison of responses with other work

The electron and proton responses obtained above are compared with the
results of Smith [28] in Fig. 2.18, where the curves are normalised to correspond
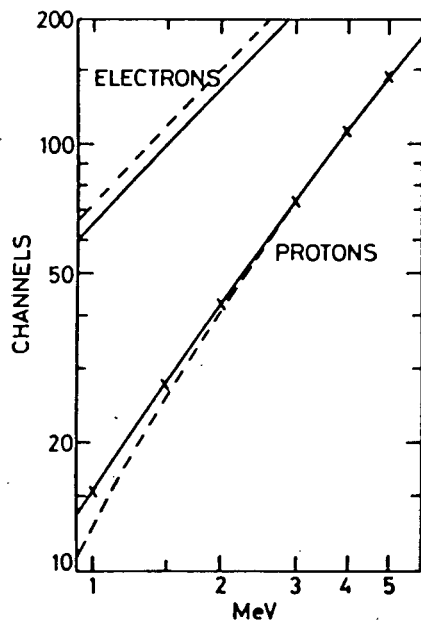
Fig. 2.18

Comparison of response curves from the proton scattering experiment with those of Smith (dotted) [28].

for 5 MeV protons.   Agreement is within 4% for protons between 2 and 8 MeV, but Smith's results are lower between 1 and 2 MeV and his electron response curve is 8.5% higher.

With regard to the electron discrepancy, we found (Sect. 2.9e) good agreement between our two methods when comparing electrons with 5 MeV protons. Since the electron normalisation was identical in each case, an error in this normalisation procedure is suggested.   The most likely reason for this discrepancy is that the 90% rule of Knox and Miller (Sect. 2.9a) is not applicable to our detectors, and it is found that if 70% of Compton peak is chosen as the maximum γ energy, then our results agree with Smith's.   This is consistent with earlier work [29], and is plausible in that our resolution is worse than Knox and Miller's and the scintillator type and configuration considerably different.

In any event, the discrepancy does not affect our results as the electron information is only used to define zero points which are independent of the percentage of Compton peak chosen.   Likewise, the disagreement for low-energy protons is also unimportant, as the largest difference, at the bias level of 1.3 MeV, is only 0.1 MeV whilst the energy resolution is 0.2 MeV.

2.9h Pulse-height and pulse-shape drift

During the course of the experiment (about 1 week) the pulse height (L) for a given particle energy was found to drift generally lower for both detectors, with corresponding changes in the pulse-shape parameter (S). The greatest change in L was 12% from the mean and its origin is not known but may be a result of partial leakage of the oil coupling between the light guide and crystal. All the electronic settings and geometry remained constant throughout. Variations were slow and it was possible to check the 4.8 MeV point before and after each run using the n-p scatter calibration (Sect. 2.9c; i)) in order to apply suitable corrections (Sect. 3.5a). By checking the drift at lower energy calibration points using gamma sources, it was found that the linear correction, $L'-L_o = f(L-L_o)$, could be applied where L' = corrected channel number, L_o = channel number at zero energy, f = correction factor determined for each run.

No correction data was taken for S but it was found that the same factors, f, could be applied where $S'-S_o = f(S-S_o)$ with the zero points, S_o, determined by inspection. This correction in S was necessary in order that the boundary used in the data reduction (Sect. 3.7b) should apply equally to all runs.

2.10 NEUTRON DETECTOR RESPONSE

A knowledge of the response for the neutron detector was less important than for detectors 1 and 2, but was required to assist in setting the L_3-T_2 limit in the data reduction (Sect. 3.8a) and for determining the bias level for the efficiency calculation (Sect. 4.9). The zero point and electron response were found in the same way as for the stilbene detectors (Sect. 2.9a) and the proton response curve was based on the results of Smith [28] and confirmed by elastic n-p scatters as in Sect. 2.9c iii).

CHAPTER 3

DATA REDUCTION

3.1   INFORMATION COLLECTED

The raw data consisted of 10 runs containing 2.75×10^6 events in total, an event being a coincidence between all three detectors with the further condition that the particle at detector 3 had passed the discriminator (Sect. 2.7e) as a neutron.   For each event, 7 parameters were recorded, together with one bit indicating a pileup condition in detectors 1 or 2 (Table 3.1).

Parameter	Name	No. of bits	Description
1	L_1	12	Pulse height, detector 1
2	S_1	12	PSD parameter, detector 1
3	L_2	12	Pulse height, detector 2
4	S_2	12	PSD parameter, detector 2
5	T_1	8	Time of flight, detector 2 to detector 1
6	T_2	12	Time of flight, detector 1 to detector 3
7	PU	1	Pileup flag
8	L_3	12	Pulse height detector 3

Table 3.1:   Recorded parameters

3.2   SUMMARY OF REDUCTION PROCESS

The primary object was to make full use of all the information collected per event to reject those which could not be npB.   The data were reduced by successive cuts as detailed in the following sections.   Referring to Table 3.2, the first step was the course application of PSD information for detectors 1 and 2 to select only events which had a proton in detector 1 and a gamma in detector 2 (p-γ events) and vice-versa (γ-p events).   The next stage was 'conversion' of the selected data which mainly involved correction of pulse-height drifts, conversion of pulse-height and time-of-flight parameters to energies, and

Reduction Stage	Described in Sect.	Operation	Events Remaining
1	3.4	Select p-γ and γ-p events.	35436
conversion	3.5	Correct L, S drifts. Convert pulse-heights (L_1, L_2) to energy (E_1, E_2). Correct T_1 drift. Add T_1 to T_2 to obtain neutron flight time; invert T_1 (γ-p data only). Select and flag npB and background regions on T_1-T_2 plane. Convert T_2 (neutron T.O.F.) to energy (E_n).	5730
2	3.6	E_p, S_p biases. Remove run 1 (p-γ data only).	2550
3	3.7	E_p-E_γ energy conservation E_γ limits & E_γ-S_γ boundary.	1571
4	3.8	L_3 limits and L_3-E_n boundary. Remove events not in T_1-T_2 regions.	1112
5	3.9	Conservation of energy.	854
6	3.10	T_1 limits, and remove pileups (regions 1, 4, 5 only).	164
	3.12	Select npB region on θ_n-θ_p plane.	9
	3.13	Background subtraction.	1.52

Table 3.2: Schedule of data reduction. The operations applied equally to the p-γ and γ-p data except where stated. Events remaining are sums of both types of data, and totals after 'conversion' refer to events in the npB region (region 1) of the T_1-T_2 plane (see Sect. 3.5e).

changing the time scales for the γ-p events so that these became the same as for the p-γ events. Subsequent reduction included stricter application of PSD boundaries to minimise gamma breakthrough into the proton region and vice versa, and removal of events which violated conservation of energy.

The remaining data were displayed as a projection on the E_p-E_n plane (Sect. 3.11). If npB events were present, this should have made them conspicuous as they would occupy a particular area as defined by the neutron detector angular range in terms of the kinematics (Fig. 2.6); however there were not enough events. The last cut was then effectively selection of events within a suitable locus on this E_p-E_n plane (Sect. 3.12). The final stage was background subtraction with respect to two time coordinates (Sect. 3.13) which left a nett total of 1.52 events.

We first examine the types of event collected in the raw data.

3.3 RAW DATA - DISCUSSION

3.3a Time-of-flight information

A typical plot of T_1 vs. T_2 (Fig. 3.1a) shows the types of coincidence possible. In the following, we classify events by the notation X-Y-Z to denote that particle X was counted by detector 1, Y by detector 2 and Z by detector 3. For example, an npB event would be p-γ-n or γ-p-n.

There are three ridges in Fig. 3.1a which coincide at $T_1 = 0$, $T_2 = 10.1$ ns. The vertical ridge containing most of the points is mainly p-p-R events where the incident neutron was elastically n-p scattered from detector 1 to 2 or vice versa, and R refers to a random count in detector 3. This ridge also contains γ-γ-R events from double Compton scatters or electron escapes between the stilbene crystals, where the incident particle was probably a gamma from the neutron source. Other events in the vertical ridge are γ-p-R or p-γ-R, for example
$${}^{1}H(n,n)\,{}^{1}H \xrightarrow{} {}^{12}C(n,\gamma)\,{}^{13}C \quad \text{(see Sect. 2.3c)}.$$
$$\underset{1}{\searrow} \qquad\qquad \underset{2}{\searrow}$$

The horizontal ridge contains p-R-n events, where an n-p elastic scatter took place in detector 1, with the recoil neutron in detector 3. The sloping ridge is similarly type R-p-n, where the slope arises because the time-of-flight between detectors 2 and 3 is represented by the sum of the times on the two axes.

The above interpretation is confirmed by examination of other projections, for example L_1 vs. S_1 and L_1 vs. T_1 (Figs. 3.1b and e). In the latter, the densely populated region occupies the correct locus for p-p-R events, and the few points at higher energy are γ-γ-R events.

3.3b Pulse-shape information

The two ridges in Fig. 3.1b are protons and Compton electrons, the protons having the higher S value.

There are a number of data points between and outside both ridges. One cause of these is pileup (Sect. 2.7f) where L and S may have wrong values. The effect of pileup rejection on the data of Fig. 3.1b is shown in Fig. 3.1d, the main feature being the removal of events on the low-S side of the gamma (electron) ridge. This demonstrates the satisfactory operation of the pileup rejection system, as this is the only region where real events could certainly not occur.
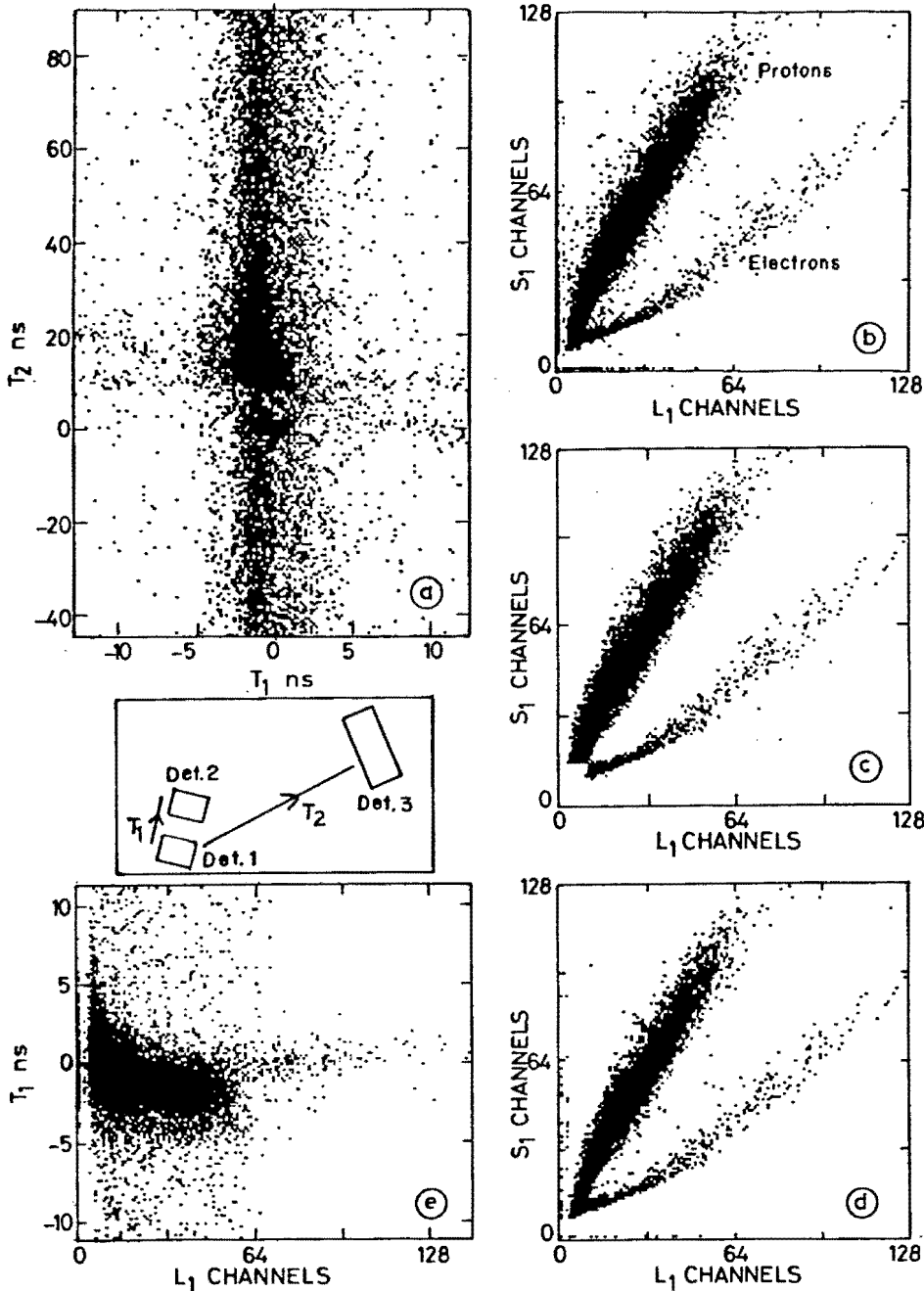
Fig. 3.1

Raw (triple-coincidence) data projections; part ($\simeq \frac{1}{4}$) of run 7. (c) shows the data of (b) after application of boundaries to select protons and electrons, and (d) is as (b) with pileups removed. For definition of parameters, see Table 3.1.

The remaining data points between the ridges are attributed to 'composite' particles in which a proton and an electron were detected simultaneously in the same crystal. A likely reaction giving rise to these is $^1H(n,n)^1H \longrightarrow {}^{12}C(n,\gamma)^{13}C$,

where the Compton scattered gamma or electron is detected in detector 2 with a random particle in detector 3. Strong evidence for this type of reaction emerged

from an earlier experiment in which coincidences from this mid-ridge region in one crystal with gammas in the other crystal were examined. Nearly all the observed events were such that the total energy of the scattered particles was greater than the incident energy; this implies the participation of a reaction with a positive Q-value, and the ^{12}C neutron capture reaction is the most likely candidate.

3.4 REDUCTION STAGE 1, L-S REGION SELECTION

The first step was to use the PSD information from detectors 1 and 2 to remove the mass of unwanted p-p and γ-γ events, leaving and separating the required p-γ and γ-p events. This was achieved by defining boundaries on the L-S plane to correspond with the extent of the proton and electron ridges, and discarding events outside them, as illustrated for detector 1 in Fig. 3.1b and c.

Over the course of the experiment, the gain on L and S for both detectors 1 and 2 was observed to shift by up to ± 12% (see Sect. 2.9h) with the result that the proton and electron loci were not identical from run to run. Fortunately it was found that the same course boundaries could be applied to all runs, bearing in mind that the purpose of this reduction stage was purely to remove most of the unwanted data. The boundaries were thus somewhat generous and a small amount of electron breakthrough at low energy into the proton region, and vice versa, was allowed. L-S distributions were obtained for the detectors for protons and electrons separately, using a gamma-source and the neutron source without coincidence requirements, and these were used to assist in defining the boundaries. The L and S gain drifts were later corrected (Sect. 3.5a) and stricter cuts then applied (Sects. 3.6; 3.7).

It is instructive to examine the T_1 vs. T_2 projections (Fig. 3.2) after the above cut. Concerning the γ-p data (Fig. 3.2b), the horizontal p-R-n ridge at 10.1 ns in the raw data (Fig. 3.1a) has correctly disappeared, whilst the sloping R-p-n ridge remains but is reduced. We deduce that most of the R-p-n events in the raw data had a random proton in detector 1, and that the remaining events are those with a random gamma in detector 1. A new horizontal ridge has become evident near $T_2 = 0$, which is identified as γ-R-γ events where the gamma in detector 3 bypassed the n-γ discriminator and was assumedly Compton-scattered from detector 1. The vertical ridge now contains mainly γ-p-R events.

The features in the p-γ data (Fig. 3.2a) were identified by similar arguments; the horizontal ridge contains the remaining p-R-n events, the new sloping ridge R-γ-γ, and the vertical ridge p-γ-R events.
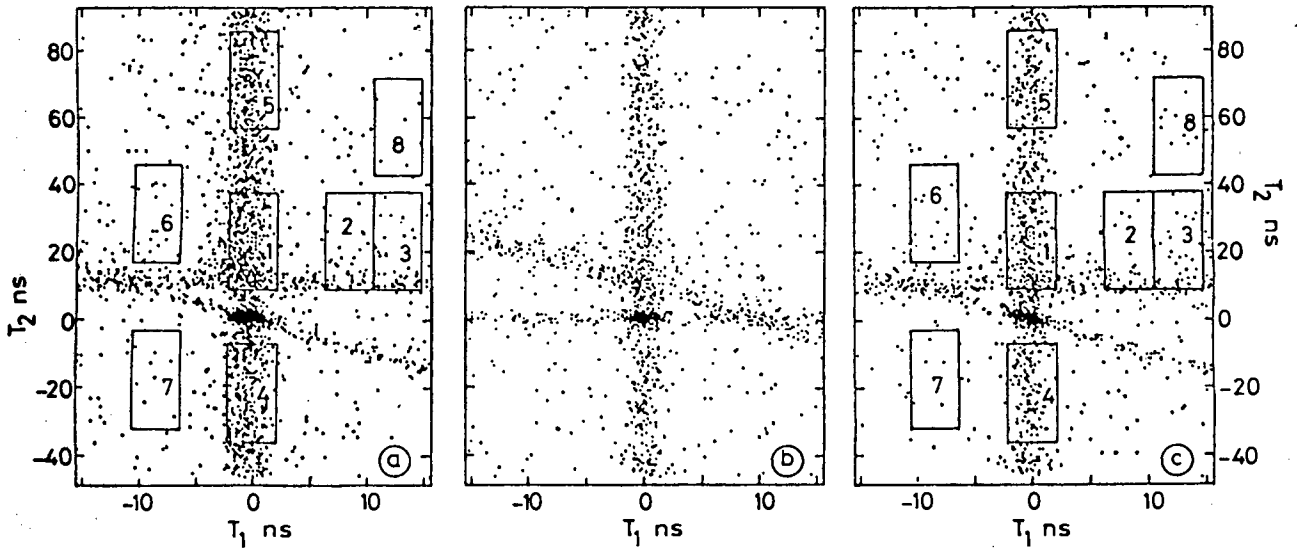
Fig. 3.2

Time projections after reduction stage 1, Run 7.   (a) p-γ data;   (b) γ-p data;
(c) γ-p data after time conversion.   In (a) and (c), npB events can occur in
region 1, and the other regions were selected for background subtraction
(Sect. 3.5e).   The distribution of events in (a) and (b) can be compared with
the raw data (Fig. 3.1a), noting that the above is derived from a larger
original sample of data (see text, Sect. 3.4).

3.5 CONVERSION

The data from stage 1 reduction were passed run-by-run through program
'conversion' which had a number of functions (Table 3.2) as detailed below.

3.5a L and S drift correction

The origin and methods of monitoring these drifts are described in Sect.
2.9h.   Linear correction was applied to each event for detectors 1 and 2
according to the formulae $L'-L_0 = f(L-L_0)$, $S'-S_0 = f(S-S_0)$ where L',S' are the
corrected values, and the factor f was determined for each run.   Constants
L_0,S_0 were the same for all runs.

3.5b T_1 correction

A zero shift in T_1 of up to $\pm$ .6 ns of unknown origin was observed over the
course of the experiment, and corrected here.   The correction constants were
obtained by monitoring the position of a T_1 coincidence peak taken with the
normal neutron source, but without requiring coincidence with detector 3.
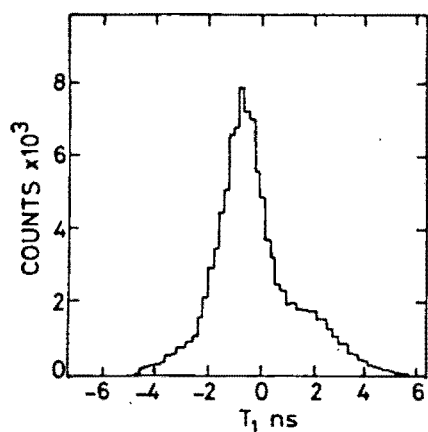
Fig. 3.3

Typical T_1 coincidence peak, used to monitor zero shift in T_1.

In the typical peak of Fig. 3.3, the events are predominantly n-p elastic scatters between the crystals; the asymmetry results from the geometry which favours scatters from detector 1 to detector 2.

3.5c Conversion of pulse heights to energy

The detector response curves (Sect. 2.9) were used to convert parameters 1 and 3 (L_1 and L_2) to energy (E_p and E_γ). In the case of the p-γ data parameter 1 now gave the proton energy, E_p, and parameter 3 gave the minimum gamma energy, E_γ, for the event.

3.5d Time conversion

In this operation, the time scales for the γ-p data were changed so as to be the same as the p-γ data, so that both sets of data could hereafter be treated identically (Fig. 3.4). For the γ-p data only, the sign of T_1 was changed, and
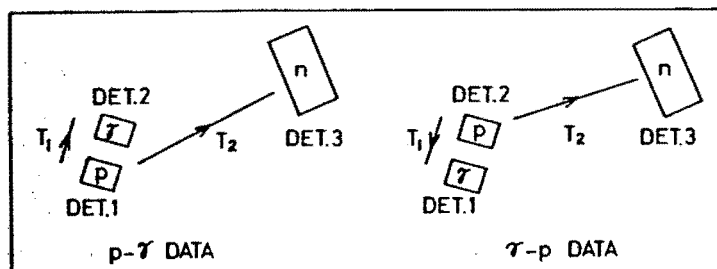
Fig. 3.4

Definition of T_1, T_2 after time conversion.

T_2 became effectively $T_1 + T_2$; T_1 and T_2 both now referred to the time of the count in the proton detector.

The effect on the $T_1 - T_2$ projection for the γ-p data of Fig. 3.2b is shown in Fig. 3.2c, where the features are now in the same positions as in Fig. 3.2a (p-γ data).

3.5e Region selection

The events in eight regions of the T_1-T_2 plane were selected (Fig. 3.2) and an appropriate flag put into parameter 7 (so far used only for the pileup bit). npB events could occur in region 1, with different types of background represented in the other regions. The background species and method of subtraction are detailed in Sect. 3.13.

3.5f Conversion of neutron time-of-flight to energy

The most probable neutron energy, E_n, was computed from T_2 and the result put to parameter 9, leaving parameter 6 unchanged. Evidently, the events of regions 4-8 had a random count in detector 3 and could have no dependence on T_2; a direct calculation of E_n for these regions would thus be meaningless. However, in order to treat all regions equally in subsequent data reduction, it was necessary to calculate a pseudo-energy, E_n, for these regions; this was done by shifting the region prior to calculation of E_n so as to coincide with regions 1, 2 and 3 (see Sect. 3.13b). The accuracy of E_n was poor ($\simeq .35$ MeV at 1.5 MeV) owing to the short flight path and large detector dimensions.

3.5g Total energy calculation

The final stage of the 'conversion' program was the addition of parameters 1, 3, 9 to give a minimum total energy for the event, which became parameter 10.

3.5h Parameter changes and summary

The operations performed by 'conversion' and changes to the recorded parameters are summarised in Table 3.3.

Hereafter, the notation E_p refers to the proton energy, which could be E_1 or E_2, representing the p-γ or γ-p data. A similar meaning is attached to E_γ, S_p and S_γ.

Parameter	Before	After	Changes
1	L_1	E_1	pulse-height $\rightarrow$ energy
2	S_1	S_1	
3	L_2	E_2	pulse-height $\rightarrow$ energy
4	S_2	S_2	
5	T_1	T_1	} times converted (p-γ data)
6	T_2	T_2	
7	P.U. flag	P.U. & region flag	region flags introduced
8	L_3	L_3	-
9	-	E_n	energy computed from T_2
10	-	$E_1 + E_2 + E_n$	total energy computed

Table 3.3: Parameter changes during conversion.

3.6 REDUCTION STAGE 2

3.6a E_p, S_p biases

The purpose of further cuts on the proton ridge was twofold. Firstly, a standard bias for all runs was required; on drift correction for L and S, the primary boundaries of stage 1 moved, giving each run effectively a different bias. Secondly, there were a number of events at low E_p, S_p (Fig. 3.5a) which were evidently not protons as the S_p distribution for a particular value of E_p was heavily bunched at low S_p. These events could be γ-γ where electron breakthrough occurred into the proton region. However, they are some distance from the γ-ridge, so may be composite-γ events (see Sect. 3.3b). Whatever the cause, these events had to be removed.

The bias levels chosen ($E_p > 1.0$ MeV; $S_{p1} > $ ch 22; $S_{p2} > $ ch 16) removed most of the offending events. The observed effect on the T_1-T_2 plot was the removal of most of the T_1-coincidences in the vertical ridge; this ties in with the above suggestion that the events were correlated γ-γ coincidences.

In effect these limits were later superseded by the final event selection on the θ_p-θ_n plane (Sect. 3.12) which removed any protons below 1.37 MeV.

3.6b Removal of run 1, p-γ data

The gate on the LGS unit (Sect. 2.7b) for S_2 (parameter 4) had inadvertently been left inoperative for run 1. The result was that S_2 for a few events had an erroneously low value presumably due to a small previous pulse which was below the ARC unit bias and hence did not cause pileup rejection, and yet held the LGS unit busy during the correct pulse. The effect was that some protons in detector 2 were thrown into the gamma ridge; the particles in this ridge therefore had an ambiguous identity and could not be further included in the analysis. The proton ridge apparently remained uncontaminated and there was no reason to discard the γ-p data.

3.7 REDUCTION STAGE 3

3.7a E_γ limits

As for protons in stage 2, a standard E_γ bias for all runs was necessary. The bias setting is critical as it determines the gamma detection efficiency. It was set at the lowest value ($E_\gamma \geqslant .425$ MeV or $E_e \geqslant .34$ MeV) which would override the effective bias set by the stage 1 boundaries before drift correction. An upper limit was also set on E_γ as, in terms of the E_p-E_n region chosen (Sect. 2.3f), the npB photon could not have an energy greater than 2.2 MeV at the maximum incident energy.

3.7b E_γ-S_γ strict boundary

Comparison of E_γ-S_γ plots of data after stage 1 with similar spectra from a ^{60}Co source (Fig. 3.5b and c) shows that the S_γ distributions at low E_γ do not correspond; there are more points in the data at high S_γ, towards the proton region. This indicates the presence of particles which are not gammas but could be proton escapes or composites (Sect. 3.3b). Further analysis showed that these events were not removed by any of the later cuts, in particular, pileup removal or tighter restrictions on T_1. In attempt to remove some of these, an E_γ-S_γ boundary was imposed putting an upper limit on S_γ for given E_γ. The boundary was chosen to be stricter than the stage 1 boundaries for all runs after drift correction, with the provision that it should have negligible effect on the ^{60}Co spectrum. In fact < ½% of the ^{60}Co events above bias were lost by this cut. The effect of the cut on the data of Fig. 3.5b is shown in
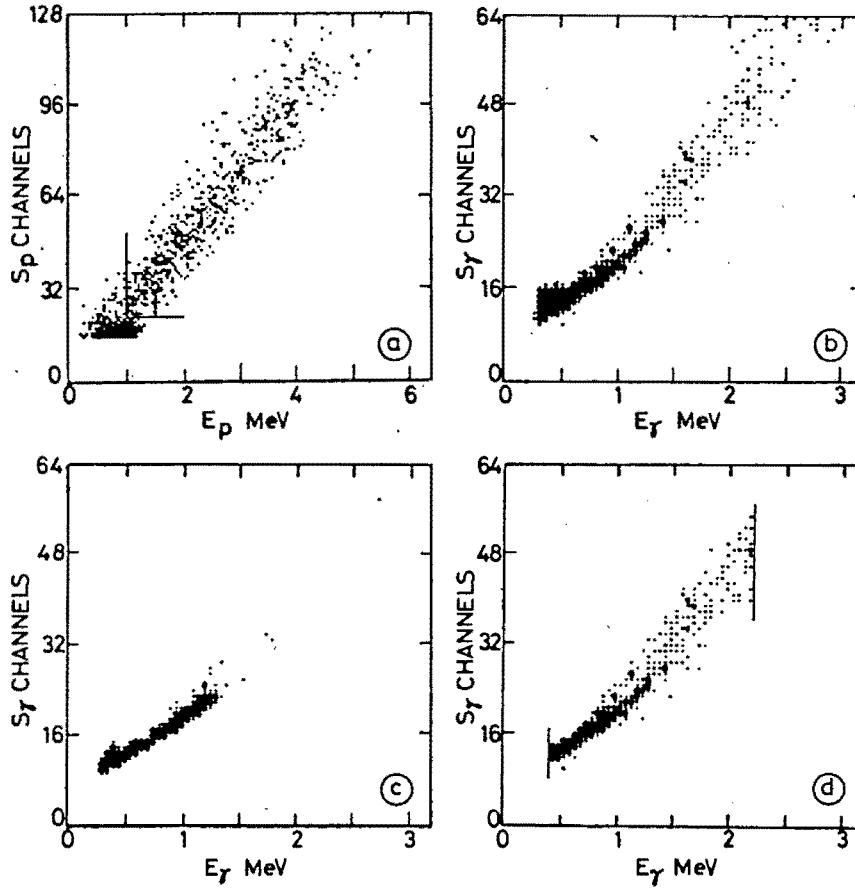
Fig. 3.5

E-S distributions after conversion (detector 1, part of run 7); (a) proton distribution showing biases at reduction stage 2; (b) gamma distribution; (c) gamma distribution from a ^{60}Co source; (d) as (b) after application of stricter boundary and biases at reduction stage 3.

Fig. 3.5d. It was found that there was no need for a lower S_γ boundary on the gamma locus as, after later reduction stages, no points on this side of the locus remained.

There is no guarantee that this cut removed all the offending points. Indeed, it is possible that proton escapes have passed as gammas through the complete data reduction, and there is no way of isolating them (see Sect. 3.11).

3.7c E_p-E_γ energy conservation

The bias on the neutron detector was later (stage 4) set to 0.4 MeV with the result that, for an npB event, $E_p + E_\gamma \leqslant 4.74$ MeV, where an allowance of 0.2 MeV has been made for proton energy resolution, with the maximum incident energy of 4.94 MeV. A boundary was imposed on the E_p-E_γ plane to this effect.

This could be expected to provide some protection from events of the type
$^1H(n,n)$ $^1H \longrightarrow$ $^{12}C(n,\gamma)$ ^{13}C, as the latter reaction has a Q-value of 4.95 MeV.

3.8 REDUCTION STAGE 4

3.8a L_3-T_2 limits

The neutron detector pulse-height, L_3, is a measure of the proton recoil energy in that detector, and thus sets an upper limit to the neutron energy. For real events this must be consistent with the neutron energy, E_n, as derived from time-of-flight (T_2). The limit boundary of Fig. 3.6 was thus applied
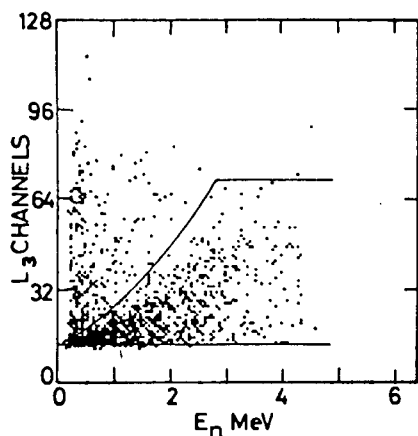
Fig. 3.6

L_3 bias and upper-limit boundary applied in reduction stage 4a. (All data after reduction 3, p-γ, npB region.)

where an allowance has been made for E_n resolution.

The bias of 0.4 MeV and an upper limit of 3.7 MeV was also imposed on L_3 at this point. This limit was the maximum neutron energy for an energy-conserving event consistent with the proton and gamma bias levels of stages 2 and 3 and had little effect.

3.8b Removal of events not in T_1-T_2 regions

There was no further purpose in retaining the events which did not fall into the T_1-T_2 regions (Sect. 3.5e) and these were discarded.

3.9 REDUCTION STAGE 5, CONSERVATION OF ENERGY

The minimum total energy, parameter 10, could not exceed the maximum incident energy of 4.94 MeV for a real event. This cut was in the form of a boundary on the E_n-total energy plane (Fig. 3.7) as an allowance had to be made for the uncertainty in E_n which increases with E_n.
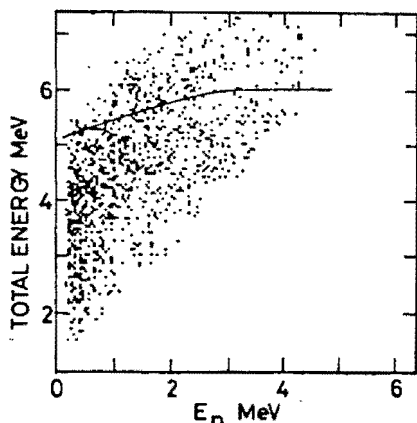
Fig. 3.7

Total energy limit applied in reduction stage 5. (All data from reduction 3, p-γ, npB region.)

3.10 REDUCTION STAGE 6

3.10a T_1 limits

A further restriction on T_1 was necessary to protect against mimic events of the type $^1H(n,n)^1H \longrightarrow X(n,n'\gamma)X$ (see Sect. 2.3g). This was set to $T_1 = 0 \pm 1.14$ ns which superseded the limits set by the region selection on the T_1-T_2 plane (Sect. 3.5e) of $T_1 = -2.2$ to $+2.0$ ns. This restriction is only relevant for regions 1, 4, 5 (see Fig. 3.2a) and it was not applied to the others. A proportional reduction in numbers of events for these other regions was made in subtracting background (Sect. 3.13). Some real events would be lost by this cut and an allowance was made in normalising the result (Sect. 4.4) based on the measured shape of the T_1 distribution.

With regard to the p-γ data, we had been conscious of two problems throughout most of the reduction. Firstly, all plots of E_γ-S_γ (Fig. 3.8b) have shown a number of points on the low-S side of the gamma locus which were not removed by any of the cuts; real events could not populate this region. Secondly, the T_1 distribution in region 1 (Fig. 3.8c), which should have been symmetrical about $T_1 = 0$, had a predominance of events at low T_1. Neither of these problems was present in the γ-p data.
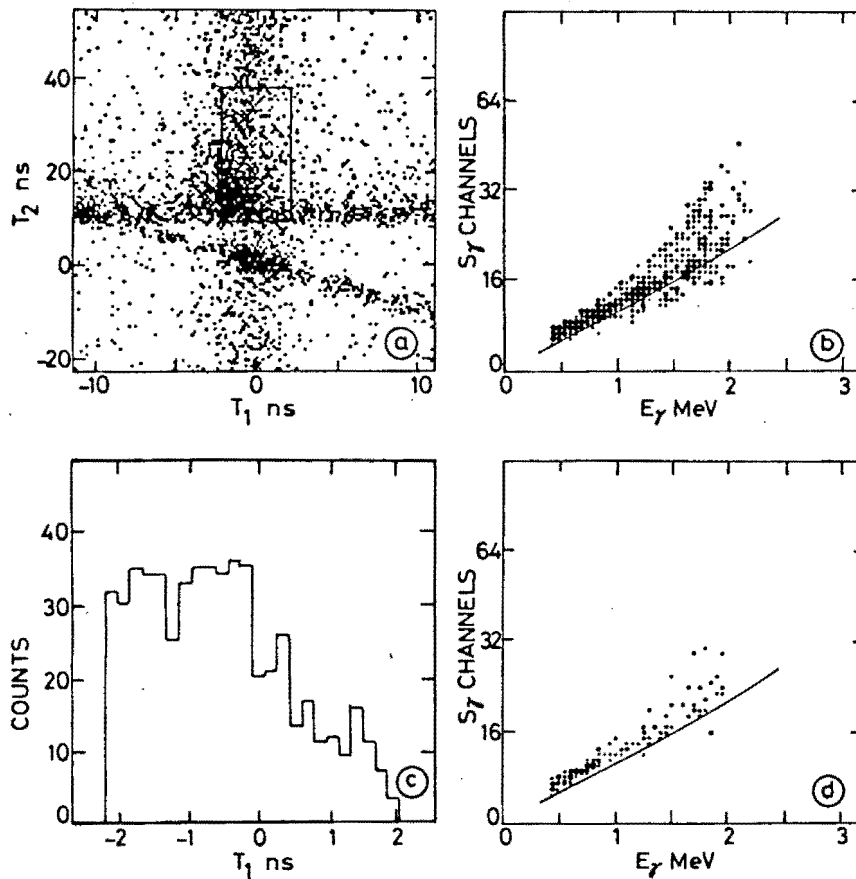
Fig. 3.8

p-γ events 'off-the-gamma locus' (reduction stage 3, run 7). (b) depicts the $E\gamma$-$S\gamma$ distribution corresponding to non-pileups in the npB region shown in (a), and (c) is the T_1 spectrum for these events. The line on (b) defines the extent of the correct gamma locus and (d) shows the improvement in (b) when only events with $T_1 > 0$ are passed.

It was established that these seemingly unconnected difficulties had the same cause. The offending events on the E_γ-S_γ plane formed part of the T_1 asymmetry and the effect was ascribed to unsuitable internal logic in LGS unit 3 (Sect. 2.7b) in which L_2 was given an incorrectly high value. A small number of low energy protons in detector 2 were thus put into the gamma ridge and beyond, and the events were thus p-p-n. A typical event is shown in Fig. 3.9 and the reasoning is as follows.
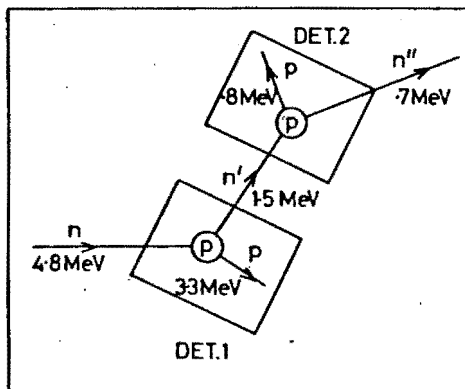
Fig. 3.9

Reconstruction of p-γ event 'off-the-gamma locus'.

The position of the offending events with respect to T_1 shows that the count in detector 2 was later than that in detector 1 by typically 0.7 ns. Taking the separation of the stilbene crystal centres as 1.2 cm, this corresponds to a neutron of 1.5 MeV travelling between the crystals. No other effect could give rise to this time difference; hence we deduce that the first scattering was n-p elastic in detector 1 with the proton being correctly detected, and the neutron recoil causing a second scatter in detector 2.

The most likely candidate for this second reaction is a further n-p elastic scatter as the T_2 value for a typical problem event corresponds to a neutron of about 0.7 MeV travelling from detector 2 to 3. This leaves 0.8 MeV for the recoil proton in detector 2 which accords with the value of S_2.

Since the L_2 error was unknown and erratic, the problem events in question must populate the gamma ridge as well as both sides of it, so that a strict selection of the points in the gamma ridge alone would serve no purpose. The other approach, which was adopted, was to cut T_1. The window for the p-γ data was set at $T_1 = 0.09$ to 1.14 ns which unfortunately resulted in the loss of half this data (i.e. about a quarter of the total data). The effect of the cut on the E_γ-S_γ plot is shown in Fig. 3.8d which convincingly demonstrates the effectiveness of the solution.

It may be expected that the reaction could occur in the opposite sense with the first n-p scatter in detector 2, followed by another in detector 1. However, this would result in a proton of higher energy in detector 2, which, if given a wrong L_2 value, could not be moved into the gamma region. This reaction is anyway not favoured by the geometry and is certainly not apparent in Figs. 3.8c and d.

3.10b Pileup removal

Pileups were here removed from regions 1, 4 and 5. Unfortunately, this cut could not be applied to the other regions as all events in these regions were recorded as pileups, due to the pileup resolution limit of 6 ns (Sect. 2.7f). As with the T_1 limits (Sect. 3.10a) a proportional reduction in events from these regions was made on subtracting background.

3.11 EXAMINATION OF REDUCED DATA

The only remaining reduction is to restrict to a portion of the E_p-E_n plane as defined in Sect. 2.3f.

Before doing this, we examine the $E_p - E_n$ distribution for the various $T_1 - T_2$ regions (Fig. 3.10). It should be noted that there are many more points in regions 2 and 3 than in region 1 because these regions did not suffer pileup removal or the T_1 limits (Sect. 3.10). Also, the higher density of points at high E_n in regions 1, 2 and 3 is attributed to elastic breakthrough, $^1H(n,n)^1H$ $_3$ $_2$

with a random photon in detector 1 (see Sect. 2.3f).
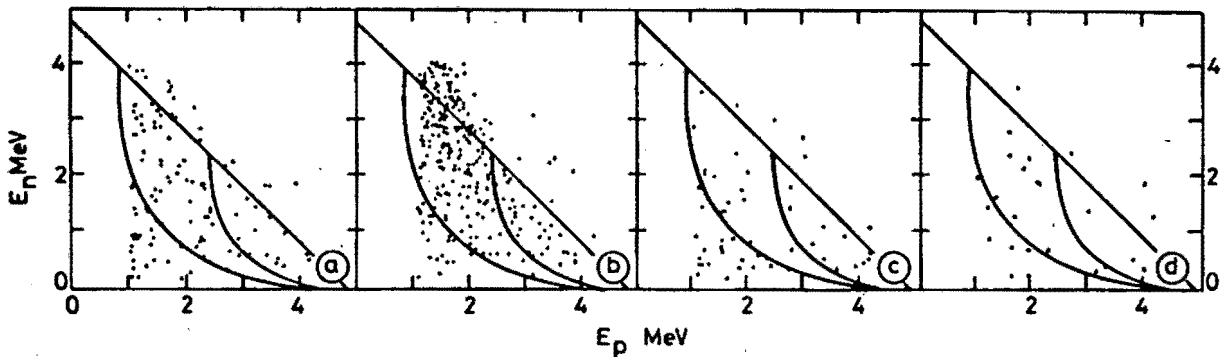
Fig. 3.10

Final E_p-E_n projections for the regions of the T_1-T_2 plane (all γ-p data).
(a) region 1 (npB region); (b) regions 2 and 3; (c) regions 4 and 5;
(d) regions 7 and 8. (See Fig. 3.2 for definition of regions.) The area shown is that allowed for npB by the neutron detector geometry.
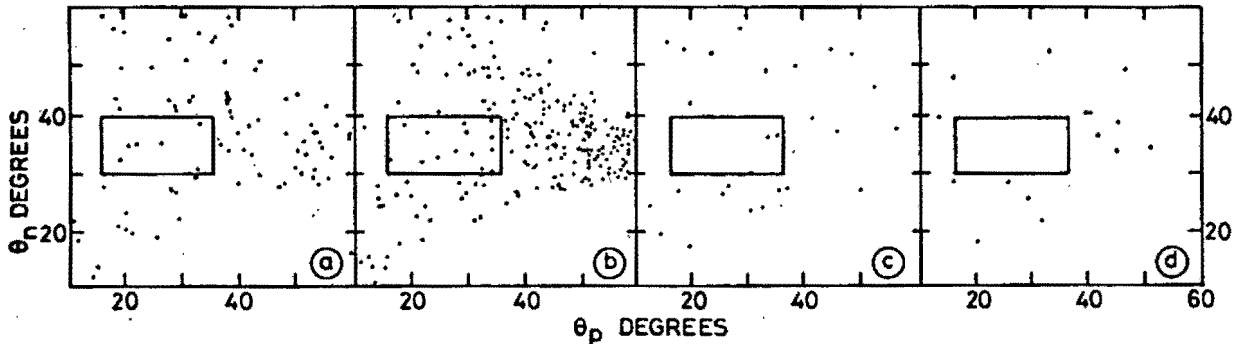
Fig. 3.11

Plot of the data of Fig. 3.10 as a function of θ_p and θ_n. The final counts were made in the areas shown.

There is no evident enhancement of points in region 1 in the area allowed for npB by the neutron detector geometry, but this is hardly surprising as the final nett npB count for the γ-p data shown was only 1.2 events (Sect. 3.14). The only certainty is that, if npB events were present, they would occupy this E_p-E_n area within energy resolutions ($E_n = \pm$ .35 MeV at 1.5 MeV). On the other
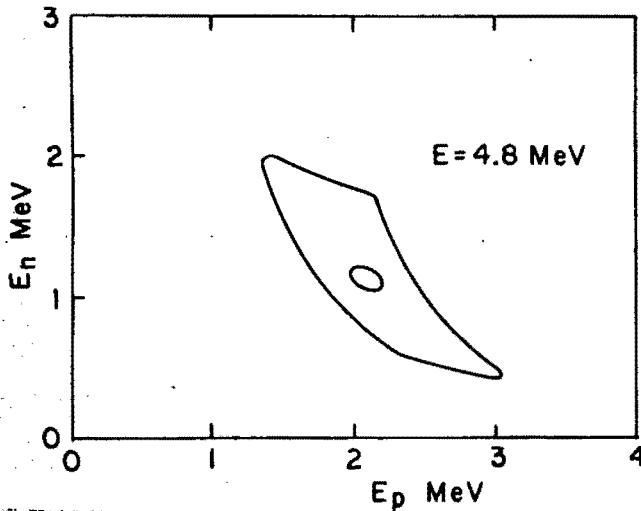
Fig. 3.12

Kinematically allowed regions. For $\theta_p = 25^0$, $\theta_n = 35^0$, events are confined to the small inner region. The outer region (repeated from Fig. 2.6) applies when the detectors are extended so that $15^0 < \theta_p < 35^0$, $30^0 < \theta_n < 40^0$.

and the required selection on the θ_p-θ_n plane could be made on the E_p-E_n plane by calculating the boundary locus using Fig. 3.13.
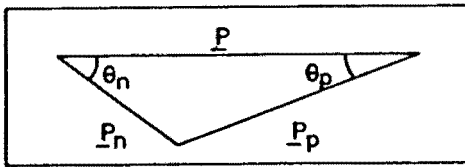
Fig. 3.13

Momentum diagram where the photon momentum, P_γ, is set to zero corresponding to the limit of low incident energy.

At the finite incident energy of this experiment, this procedure is still valid since the areas on the E_p-E_n plane corresponding to each value of θ_p and θ_n are still small relative to the large E_p-E_n area chosen for observation. This would only be invalidated if the cross-section varies rapidly in the vicinity of the boundary, which is highly unlikely.

The boundary calculated from Fig. 3.13 could thus be drawn on the final E_p-E_n data projections (Fig. 3.10) and events counted within. However, it was easier to calculate θ_p, θ_n from E_p, E_n for the remaining data points, and to project them on the θ_p-θ_n plane (Fig. 3.11) as the boundary is then a rectangle. This procedure gives the correct count, but there is evidently some uncertainty in the angles arising from the kinematics; this is however smaller than that resulting from the uncertainty in E_p and E_n, typically 0.2 and 0.35 MeV respectively.

The final numbers of possible npB events from region 1 (Fig. 3.11a) were 3 (p-γ data) and 6 (γ-p data).

3.13 BACKGROUND SUBTRACTION

3.13a Principles

In Sect. 3.5e, Fig. 3.2, 8 regions of the T_1-T_2 plane were defined for the purposes of subtracting background. As summarised in Table 3.4, region 1 contains triply correlated events which should only be npB, as well as doubly correlated coincidences from random counts in all three detectors. The other regions contain the various varieties of background.

Since the regions are the same size, those other than region 1 are replicating the background events in region 1, and it is the nett count in this region which is required. According to Table 3.4, this could be achieved as

$$N_{br} = N_1 - N_2 - N_4 - N_6 + 2N_7 \qquad\qquad 3.1$$

where N_{br} is the nett count and there are N_i events in region i.

Region	Class of Events				
	Triple Correlated	Doubly Correlated			Triple Random
		Random n-detector (Type T_1)	Random γ-detector (Type T_2)	Random p-detector (Type T_3)	
1	×	×	×	×	×
2			×		×
3			×		×
4		×			×
5		×			×
6				×	×
7					×
8					×

Table 3.4: Classes of events in T_1-T_2 regions.

However, no background events of type T_3 (Table 3.4) were ever observed, so region 6 was disregarded; also the uncertainty of the result is reduced by using larger regions, so a better result can be obtained from:

$$N_{br} = N_1 - \frac{1}{2}(N_2 + N_3) - \frac{1}{2}(N_4 + N_5) + \frac{1}{2}(N_7 + N_8) = \sum_i f_i N_i \qquad 3.2$$

and this is basically what was done.

3.13b Treatment of background regions during reduction

It was necessary to define the T_1-T_2 regions early in the analysis because both these parameters were used in the subsequent reduction. Having defined the regions, it was important that all stages of reduction should treat each region identically, otherwise the subtraction would be invalid.

In reduction stages 4a and 5 (L_3-E_n boundary and conservation of energy) the neutron energy, E_n, as derived from T_2, was used. These stages could only validly be applied to regions 1, 2, 3 since all the events of regions 4-8 were random in the neutron detector and hence independent of T_2. Now the above cuts acted to remove some of the type T_1 background from region 1, which background is also represented in regions 4 and 5 (Table 3.4), so a similar removal had to be made from these regions. Further, after the cuts, the distribution of T_1 background in region 1 was no longer independent of T_2, so the event removal from regions 4 and 5 had to be done in such a way that this new T_2 distribution was also reproduced. This is important as the final count was made with respect to θ_p, θ_n as derived from E_n (T_2), so the correct distribution with respect to T_2 had to be maintained for all regions during the reduction.

The solution to this problem was temporarily to shift T_2 for regions 4-8 so as to coincide with region 1 for the purposes of calculating a pseudo-energy, E_n', for these regions (Sect. 3.5b). This value of E_n was then used in the above cuts in precisely the same way as the real E_n for regions 1, 2, 3. Evidently E_n', and thus θ_p, θ_n', for regions 4-8 have no meaning other than leading to the correct nett count on subtraction. In principal this approach is the same as the 'delayed coincidence' method of Edgington et al. [10].

In stage 6a, limits on T_1 were applied to regions 1, 4, 5, effectively reducing the width of the regions. In order that regions 2 and 3 should continue to replicate the type T_2 background in region 1, these regions could have been similarly reduced in width. However, since the events in these regions were independent of T_1, they were all retained and a smaller fraction of them was used on subtracting. This procedure led to a smaller final error and was applied also to regions 7 and 8.

Likewise, the pileup removal of stage 6b could only be applied to regions 1, 4, 5 as the pileup rejector was only effective in the range $T_1 = 0 \pm 6$ ns

(Sect. 2.7g). In the absence of any information as to which events of regions 2, 3, 7, 8 were pileups, the pileup loss rate was extracted from the data (Sect. 3.13c) and the numbers of events in these regions were again proportionally reduced when subtracting.

3.13c Pileup loss factors

For the correct weighting of background subtraction, we require to know the fractions ($\overline{PU}$) of the remaining events of regions 2, 3, 7, 8 which would have passed pileup had the rejection system been effective for these regions.

Since the probability of pileup in either detector depends only on the proximity of a previous or following event, all events in the raw data, irrespective of type, have equal probability of being pileups. However, events recorded as pileups may be displaced on the L-S plane (the object of the rejection system was to remove such events). Hence, since reduction stage 1 consisted of cuts on the L-S plane, $\overline{PU}$ after stage 1 and subsequent cuts is likely to be different from $\overline{PU}$ for the raw data. Furthermore, $\overline{PU}$ may now vary according to the class of event.

In fact, for events random in T_1, $\overline{PU}$ remained not statistically different from constant during the reduction (Table 3.5); however for correlated T_1 coincidences, $\overline{PU}$ generally decreased during reduction, being 80% in the raw data and about 72% (γ-p data) after stage 1. This is predictable, as, in the raw data, about 40% of random T_1 coincidences were p-γ or γ-p, whilst only about 5% of correlated T_1 coincidences were p-γ or γ-p, with the main contributors being p-p or γ-γ (see Sect. 3.3a). As a result, one would expect an appreciable fraction of p-p correlated events to pass stage 1 with one of the protons being seen as a γ due to L-S displacement through pileup, and thus to reduce $\overline{PU}$ as observed.

Fortunately, the values of $\overline{PU}$ required were those for events random in T_1, and the figures were obtained by counting events outside the T_1 coincidence ridge ($T_1 \simeq -3$ to $+3$ ns) yet within the working limits of the pileup rejection system ($T_1 \simeq -6$ to $+6$ ns). The results after various reduction stages are given in Table 3.5 where all runs have been added.

The values of $\overline{PU}$ used in the calculation were those after stage 1. Ideally, the stage 5 figures should have been used, but the uncertainty is much worse, and stage 1 accounts for the largest expected change in $\overline{PU}$ as it removed 98% of the collected data.

	p-γ	γ-p
Raw data	.801 ± .001	.801 ± .001
Stage 1	.803 ± .023	.807 ± .016
Stage 3	.849 ± .028	.802 ± .022
Stage 5	.831 ± .060	.788 ± .038

Table 3.5: Values of $\overline{PU}$, the fraction of events passing pileup, after various reduction stages.

3.13d Region weight factors

The weight factors f_i of Eq. 3.2 (Sect. 3.13a), $N_{br} = \sum_i f_i N_i$ must now be modified to account for the T_1 limits and removal of pileups from regions 1, 4, 5 in reduction stage 6.

The effect of the T_1 limits was that the width of these regions was reduced from 24 channels to 6 and 13 channels for the p-γ and γ-p data respectively, so the number of events counted in regions 2, 3, 7, 8 must be proportionally reduced. Combining with the pileup pass rates, 0.803 and 0.807 from Sect. 3.13c, the revised values of f_i become those of Table 3.6:

Region	1	2,3	4,5	7,8
p-γ	1	-.1004	-.5	.1004
γ-p	1	-.2185	-.5	.2185

Table 3.6: Values of f_i, the region weight factors for the purposes of background subtraction.

3.14 FINAL npB COUNT

Using Eq. 3.2 with the values of f_i of Table 3.6 on the finally selected data of Fig. 3.11, the nett numbers of events in the npB region are 0.30 (p-γ) and 1.22 (γ-p).

These numbers were not directly used in evaluating the npB cross-section, as the detection probability varied over the θ_p-θ_n plane; it was thus necessary to weight each event individually to make the result a true average over the observed angular range. This procedure is dealt with in Sect. 4.5.

CHAPTER 4

CALCULATION OF CROSS-SECTION

4.1 INTRODUCTION

The most convenient form for the cross-section result from this work is in terms of ideal Harvard geometry (Sect. 1.3) in which two coplanar point detectors are used for the outgoing nucleons, leaving the photon undetected. In this experiment, both nucleon detectors had considerable extent in and out of the plane, and a photon detector was included which therefore imposed restrictions on the photon direction. These totally different geometries must be reconciled, and the necessary tools are derived from the known npB photon angular distribution (Appendix B) which, at low energies, has a dipole pattern about the recoil proton direction.

Another problem arising from the large range of observed nucleon angles is that the detection efficiency for npB events was not constant over this range. The cross-section is required as a true average over allowed values of θ_n, θ_p and the solution used was to weight each remaining event according to its position on the $\theta_n - \theta_p$ plane.

The result also had to be normalised as the incident flux was not accurately known, and this was effected by comparison with the rate of n-p elastic scatters where the photon coincidence requirement was removed. Unfortunately this rate was so high that it was inconvenient to record or count all n-p elastic scatters directly; a procedure was developed whereby a known fraction of this number was extracted from the triple-coincidence data collected during normal running.

The above and other necessary ingredients for calculating the cross-section are the subjects of Sects. 4.2 - 4.6. Details of the method of monitoring n-p elastic scatters, and the determination of photon and neutron detection efficiencies, are left to the second part of the chapter, Sects. 4.7 - 4.9.

4.2 TRANSFORMATION TO HARVARD GEOMETRY

For an ideal Harvard experiment, the number of recorded npB events, N_{br}, may be expressed:

$$N_{br} = k \, e_n \, e_p \, \sigma_{br} \, \delta\Omega_n \, \delta\Omega_p \quad ; \quad k = F \, t \, n_p \qquad 4.2.1$$

where

σ_{br} = $d^2\sigma/d\Omega_n d\Omega_p$, the npB cross-section for Harvard geometry;

F = neutron flux incident on target;

t = target thickness;

n_p = proton density in target;

e_n = neutron detection efficiency;

e_p = proton detection efficiency;

$\delta\Omega_n, \delta\Omega_p$ = solid angles subtended at the target by the (point) neutron, proton detectors.

Eq. 4.2.1 must now be altered to suit this experiment. Firstly, since no significant quantity of protons was removed in the reduction, and the escape probability is small (Sect. 3.11) e_p can be set to 1.

Now for a particular outgoing neutron direction, with no restrictions on photon direction, the proton may be non-coplanar up to a limit of a few degrees (Appendix A.2.3). Defining β_p (Fig. 4.1) as the 'noncoplanarity' angle of the proton, and β_{pm} as its maximum for particular values of θ_n, θ_p, if all
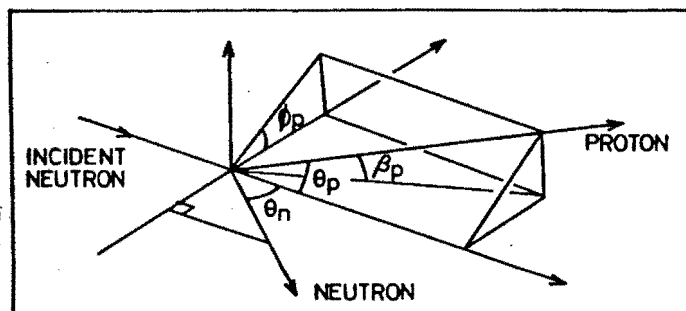
Fig. 4.1

Definition of noncoplanarity angle, β_p. The experimental plane is taken to include the incident and scattered neutrons.

kinematically allowed β_p angles are observed, we may rewrite Eq. 4.2.1:

$$N_{br} = k\,e_n\sigma_{br}\,\delta\Omega_n\,\delta\theta_p \int_{-\beta_{pm}}^{\beta_{pm}} f(\beta_p)\,d\beta_p \qquad\qquad 4.2.2$$

where $f(\beta_p)$ gives the change in cross-section with β_p, and $f(0) = 1$ (since β_p is small, $\delta\Omega_p = \delta\theta_p\delta\beta_p$). In Appendix B, $f(\beta_p)$ is derived using the photon angular distribution (see also Sect. 5.8):

$$f(\beta_p) = 1 + \beta_p^2/\beta_{pm}^2 \qquad\qquad \text{for } -\beta_{pm} \lesssim \beta_p \lesssim \beta_{pm}$$

$$= 0 \qquad\qquad\qquad\qquad \text{otherwise}$$

and

$$\int_{-\beta_{pm}}^{\beta_{pm}} f(\beta_p)\, d\beta_p = \left(\tfrac{8}{3}\right)\beta_{pm}$$

Substituting into Eq. 4.2.2:

$$N_{br} = \left(\tfrac{8}{3}\right) k\, e_n\, \sigma_{br}\, \delta\Omega_n\, \delta\theta_p\, \beta_{pm} \qquad\qquad 4.2.3$$

Eq. 4.2.3 now relates to the case where $\delta\Omega_n$ and $\delta\theta_p$ are still small, but $\delta\beta_p$ is enlarged so as to be greater than the kinematic limits; $\delta\beta_p > 2\beta_{pm}$. However, it applies equally if $\delta\beta_n$, the neutron out-of-planar range, is also enlarged. For each pair of angles θ_n, θ_p, the experiment can be considered as the sum of point neutron detector experiments at all angles β_n allowed by the neutron detector size, with all kinematically allowed β_p angles in each case. In other words, we are considering the sum of results as the point neutron detector experiment is rotated about the incident neutron axis. Eq. 4.2.3 thus applies to an experiment with nucleon detectors whose non-coplanar extents exceed the kinematical limits. As $2\delta\theta_p \beta_{pm}$ is in fact the useful proton detector solid angle for any point on the neutron detector, the only modification from Eq. 4.2.1 is the inclusion of the $\tfrac{4}{3}$ 'Harvard factor' to account for noncoplanarity.

Eq. 4.2.3 does not yet provide for our photon detector; in fact it would apply to an experiment which included a photon detector whose efficiency was unity over 4π solid angle. At this stage we can simply include the photon detector as an efficiency e_γ; in Sect. 4.7 the known photon angular distribution is folded into the calculation of e_γ. Thus, rewriting Eq. 4.2.3:

$$N_{br} = \left(\tfrac{8}{3}\right) k\, e_n\, e_\gamma\, \sigma_{br}\, \delta\Omega_n\, \delta\theta_p\, \beta_{pm}\, C$$

$$k = F\, t\, n_p \qquad\qquad 4.2.4$$

The factor C allows for those events lost by the T_1 window (Sect. 3.10a). Eq. 4.2.4 is now completely applicable to the experiment undertaken.

4.3 NORMALISATION

In order to avoid having to determine the incident flux, F, and the absolute neutron detection efficiency, e_n, the results were normalised against

n-p elastic scatters, where the incident neutron was scattered in one of the stilbene crystals to the neutron detector. Using notation similar to that of Sect. 4.2 (primed quantities refer to elastic scatters), the number of elastic scatters is:

$$N_{el} = k \, e'_n \, \sigma_{el} \frac{\cos \theta'_n}{\pi} \, \delta\Omega'_n \qquad 4.3.1$$

where σ_{el} is the total n-p elastic cross-section. The solid angle $\delta\Omega'_n$ here refers to the whole neutron detector. This is not the same as $\delta\Omega_n$ as the observed polar range for npB events, $\delta\theta_n$, was restricted.

N_{el} was measured for each stilbene detector for each run, and k calculated from Eq. 4.3.1 for use in Eq. 4.2.4. The results are summarised in Table 4.1. The method of finding N_{el} was indirect, using the raw data collected during normal running (Sect. 4.7).

4.4 EVENT LOSSES

In reduction stage 6, limits were imposed on T_1, and pileups were removed. Since neither of these restrictions applied to the normalisation using elastic scatters, appropriate corrections must be made.

The loss from the T_1 limits occurs in Eq. 4.2.4 as factor C which is evaluated as follows. The T_1 coincidence peak as measured using a ^{22}Na source between the detectors was close to Gaussian with FWHM 1.8 ns (Sect. 2.7c), centred on $T_1 = 0$. Using the T_1 limits of stage 6, (0.09 to 1.14 ns, p-γ data; -1.14 to 1.14 ns, γ-p data), the fractions of events after the cut, C, are simply calculated from areas under the Gaussian as 0.411 and 0.869 respectively.

The fraction of events passing pileup ($\overline{PU}$) varied slightly from run to run having a weighted average for the raw data of 0.801 (Sect. 3.13c). The values of $\overline{PU}$ were built into the normalisation count, N_{el}, run by run, and the values of N_{el} of Table 4.1 refer to the sum of runs after reduction by $\overline{PU}$.

There were also event losses from deadtime in TAC 1 but these are the same for the npB data and the normalisation data and were anyway overridden by the pileup system losses (Sect. 2.7c). It should be pointed out that, to be strictly correct, $\overline{PU}$ is the ratio of events passing rejection to events passing TAC 1 deadtime.

4.5 WEIGHTING OF EVENTS

From Eq. 4.2.4, the npB cross-section can now be evaluated as:

$$\sigma_{br} = \frac{N_{br}}{\left(16/3\right) k\, e_\gamma\, \delta\theta_n\, \delta\theta_p\, e_n\, \beta_n\, \beta_{pm}\, C} \qquad 4.5.1$$

where $2\delta\theta_n \beta_n = \delta\Omega_n$.

Now this equation contains terms which vary over the observed area of the $\theta_p - \theta_n$ plane. These are: (1) e_n, the neutron detection efficiency, a function of neutron energy (Sect. 4.9) which is, in turn, related to θ_p, θ_n by npB kinematics; (2) $2\beta_n$, the observed neutron azimuthal range as restricted by the detector size, which is a function of θ_n; (3) β_{pm}, the calculated maximum azimuth for the proton (Sect. 4.2), which depends on θ_p, θ_n. The photon detection efficiency, e_γ, is nearly constant over the observed range of photon energies (0.9 - 1.9 MeV) and need not be considered (Sect. 4.7c).

It was desired that the result be expressed as an average over the chosen θ_p, θ_n area; that is, the probability of observation should be equal at all points on the $\theta_p - \theta_n$ plane. For this reason, e_n, β_n and β_{pm} were calculated for all the remaining events in the foreground and background regions according to their position in this plane, and the events appropriately weighted when calculating the cross-section. Eq. 4.5.1 is thus rewritten:

$$\sigma_{br} = \frac{1}{\left(4/3\right) k\, e_\gamma\, \Delta\theta_p\, \Delta\theta_n\, C} \sum_i \frac{f_i}{4\, e_{ni}\, \beta_{ni}\, \beta_{pmi}} = \frac{1}{\ell} \sum_i w_i \qquad 4.5.2$$

where the sum is taken over all events of all regions, f_i is the appropriate region weighting factor (Sect. 3.13d), and $\Delta\theta_p \Delta\theta_n$ is now the full area of observation.

The standard deviation of the result is simply calculated from:

$$\varepsilon(\sigma_{br}) = \frac{1}{\ell} \sqrt{\sum_i w_i^2} \qquad . \qquad 4.5.3$$

4.6 RESULTS

The cross-section calculation using equations 4.3.1 and 4.5.2 are summarised in Table 4.1, where all runs have been added. The final figure for σ_{br} of 59 ± 153 μb/sr^2 has been evaluated after adding the p-γ and γ-p data. The large uncertainty in this figure is wholly due to the paucity of events and

consequent poor statistics, and the other errors, 11% for N_{el} and 9% for e_γ, have been disregarded, being small in comparison.

Class of Event	$N_{el} \times 10^6$	σ_{el} (4.8 MeV)	$\delta\Omega'_n$	θ'_n (mean)	e'_n	$k \times 10^{33}$
p-γ	44.73*	1.7b	.103 sr	35.8^0	.258	3.35* cm^{-2}
γ-p	43.27	1.7b	.114 sr	32.2^0	.246	2.93 cm^{-2}

(a) Calculation of normalisation factor, $k = N_{el}/(\sigma_{el}\, e'_n\, \delta\Omega'_n \cos\theta'_n/\pi)$ (Eq. 4.3.1). All runs have been added, and an appropriate reduction in N_{el} has been made to account for events which were pileups.
*Figures exclude run 1 (see Sect. 3.6b).

Class of Event	e_γ	$\Delta\theta_p\Delta\theta_n$	C	ℓ(sr/μb)
p-γ	.0147	.0609 sr	.411	1.64
γ-p	.0126	.0609 sr	.869	2.61
				4.25

(b) Calculation of factor $\ell = 4/3\, k\, e_\gamma\, \Delta\theta_p\Delta\theta_n\, C$ (Eq. 4.5.2).

Class of Event	$\sum_i w_i$	$\sqrt{\sum_i w_i^2}$
p-γ	47.7 ± 370.1 sr^{-1}	
γ-p	203.3 ± 536.5 sr^{-1}	
sum	251.0 ± 651.7 sr^{-1}	
σ_{br}	59.1 ± 153.5 μb/sr^2	

Upper limit to σ_{br} including one standard deviation = 212.6 μb/sr^2.

(c) Calculation of $d^2\sigma/d\Omega_n d\Omega_p = \sigma_{br} = \frac{1}{\ell}\sum_i w_i$ (Eq. 4.5.2).

Table 4.1: Summary of cross-section calculation.

4.7 METHOD OF MONITORING ELASTIC n-p SCATTERS

4.7a Coincidence method

The straightforward method for finding N_{el} would have been to collect all coincidence events between either stilbene crystal and the neutron detector; however the large number of events collected in this way could not be conveniently handled. Instead, the required information was extracted for each run from the uncut raw triple-coincidence data as follows:

i) An offset cut was imposed on T_1 (Fig. 4.2a). This then selected events in which the stilbene-stilbene coincidence was random.

ii) These events were projected as a T_2 spectrum (Fig. 4.2b) with the two peaks each corresponding to elastic scatters from a stilbene crystal to the neutron detector, whilst the count in the other stilbene was random.
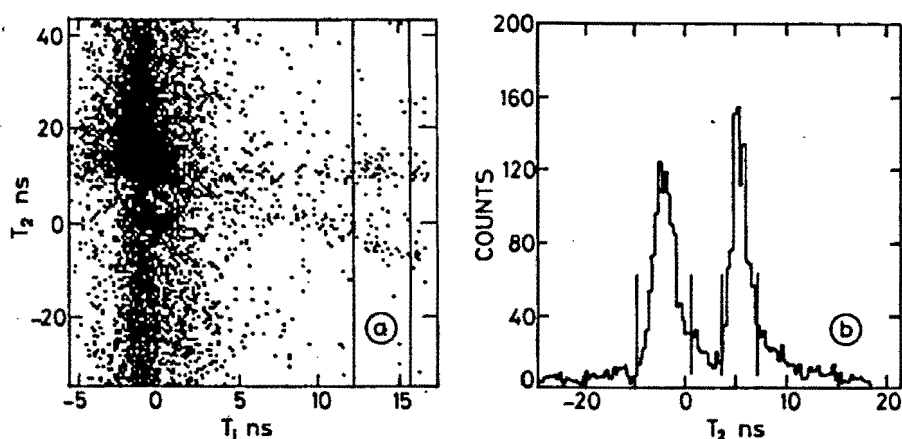
Fig. 4.2

Counting elastic scatters. (a) part of run 7, showing cut; (b) T_2 spectrum corresponding to cut in (a), whole of run 7.

iii) The nett numbers of events in each peak, N_{c1} and N_{c2} were counted.

iv) For the p-γ data, N_{el} was calculated from $N_{el} = N_{c1}/(\mu_2 \omega)$ $(N_{el} = N_{c2}/(\mu_1 \omega)$ for the γ-p data) where $\mu_2 (\mu_1)$ = average count rate in detector 2(1) as obtained from scaler readings, ω = width of cut in i), and the formula is derived in Appendix E. The figures for μ_1 and μ_2 include a small downwards correction to allow for the fact that some of the counts scaled were correlated T_1 coincidences and hence could not contribute to N_c.

This method relies on the assumption that μ_1 and μ_2 remain constant during a run. This is not strictly correct and variations of up to 10% were normal which would cause N_{el} as derived above to be high by ½%. This is much smaller than the other errors involved and was disregarded.

The largest error arises from counting the events in the elastic peaks as the window positions are somewhat arbitrary. The peaks have a predictable spread towards low neutron energy (high T_2) due to multiple scatters in which, for instance, the elastic recoil neutron was rescattered from some of the hardware before being detected. The windows were in fact chosen to be consistent with the known range of energies of the elastic neutrons and the time-of-flight resolution, and this excluded most of the low energy tails. An uncertainty of 11% is assigned to the N_{el} value from this cause.

4.7b Comparison with other results

A direct calculation of elastic scattering rates was made using the known deuteron flux at the neutron source. This could not provide an accurate result, mainly due to the difficulty of estimating multiple scatter contributions, but showed that there were no gross errors in the results from the above indirect method.

A relative comparison of N_{el} from run to run was also made against the scaler readings. With variation of incident flux, the deadtime loss at TAC 1 varies; this is however reflected in the TAC 1 true-stop (scaler 4) whose rate should thus be proportional to the npB and n-p elastic rates.

4.8 DETERMINATION OF PHOTON DETECTION EFFICIENCY, e_γ

e_γ is the probability that a photon, emitted from an npB process in one stilbene crystal, is detected in the other, where the event passes the cuts made in the data reduction. The only relevant cut is the electron bias of 0.34 MeV (Sect. 3.7a) and the small loss from the strict E_γ-S_γ boundary (Sect. 3.7b) is disregarded. e_γ was evaluated by calculation and a course absolute check made by comparison with rates from a ^{60}Co source (Sect. 4.8e).

4.8a Calculation of e_γ

The only relevant gamma detection process in this experiment is Compton scattering, as pair production and the photoelectric effect have negligible probability due to the low-Z of the scintillator. For a photon of energy E_γ emitted from stilbene 1 and detected in stilbene 2, e_γ may be written:

$$e_\gamma(E_\gamma) = \frac{n_e}{4\pi V_1} \int_{T_b}^{T_{max}} \frac{d\sigma_\gamma}{dT} \, dT \int_{det\,1} dV_1 \int_{det\,2} dV_2 \left(\frac{g \, e^{-\sigma_\gamma n_e \ell}}{\ell^2} \right) \qquad 4.8.1$$

where

n_e = electron density in stilbene

dV_1, dV_2 = volume elements in detector 1, 2

$\int_{T_b}^{T_{max}} \frac{d\sigma_\gamma}{dT} \, dT$ = Compton cross-section, where T = electron energy;

T_b = electron bias level; T_{max} = maximum electron energy from a photon of energy E_γ

ℓ = separation of volume elements dV_1, dV_2

g = correction function allowing for the dipole angular distribution of photons from npB events (Appendix B).

The two volume integrals act to average over all positions for the npB process in stilbene 1 and to add the probabilities of detection for all volume elements of stilbene 2. These integrals were evaluated numerically (Sect. 4.8b). The effect of multiple scatters and electron escapes is discussed in Section 4.8d.

4.8b Evaluation of volume integrals

We require to know the value of:

$$I = \int_{det\,1} dV_1 \int_{det\,2} dV_2 \left(\frac{g \, e^{-\sigma_\gamma n_e \ell}}{\ell^2} \right)$$

of Eq. 4.8.1. The attenuation factor $e^{-\sigma_\gamma n_e \ell}$ allows for the removal of photons between the two volume elements by Compton scattering, and is energy dependent through σ_γ, the total cross-section. As this factor is close to 1 (e.g. 0.9), and σ_γ only varies slowly over the observed range of photon energies, the factor was taken as independent of energy with the value corresponding to a mid-range energy of 1.5 MeV. Then $\sigma_\gamma n_e = 171.4$ mb $\times$ 3.70×10^{23} cm^{-3} = .0634 cm^{-1}.

The crystals were oriented with their common axis at right angles to the observed proton direction, $\theta_p = 25°$, in order to exploit the photon dipole angular distribution in maximising the detection probability. The allowed

variation in θ_p of $\pm 10^0$ has little effect and was disregarded in the calculation. Thus, the dipole function, g, for angles θ', ϕ' shown in Fig. 4.3 is, from Appendix B, Eq. B.6:

$$g = {}^3/_2 \, (1 - \sin^2\theta' \cos^2\phi')$$

where this is normalised such that its average value is 1:

$$\bar{g} = \int g\,d\Omega / \int d\Omega = 1 \, .$$
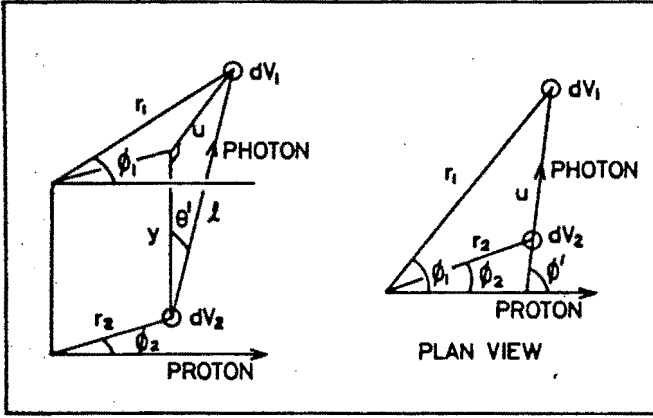
Fig. 4.3

Coordinate definitions for evaluation of volume integrals in the calculation of e_γ, the photon detection efficiency.

We now transform to cylindrical coordinates, r, ϕ, t as shown, where $y = s + t_1 + t_2$, s = separation of crystals. From the geometry:

$$\cos \phi' = \frac{r_1 \cos \phi_1 - r_2 \cos \phi_2}{u} \, , \quad \sin \theta' = u/\ell$$

then the integral becomes:

$$I = \frac{3}{2} \int_0^{R_1} dr_1 \int_0^{R_2} dr_2 \int_0^{T_1} dt_1 \int_0^{T_2} dt_2 \int_0^{2\pi} r_1 d\phi_1 \int_0^{2\pi} r_2 d\phi_2 \left\{ \left(1 - \frac{(r_1 \cos \phi_1 - r_2 \cos \phi_2)^2}{\ell^2}\right) \frac{e^{-\sigma_\gamma n \ell}}{\ell^2} \right\}$$

4.8.2

where $\ell^2 = y^2 + u^2$

and $u^2 = r_1^2 + r_2^2 - 2r_1 r_2 \cos (\phi_1 - \phi_2)$.

This was evaluated numerically using the known crystal dimensions and separation as $I = 49.50$ cm^4.

The dependence on the correction terms was also checked; the dipole function, g, caused a 15.4% increase in I whilst the attenuation term, $e^{-\sigma_\gamma n_e \ell}$ reduced the result by 9.6%.

The greatest contribution to the uncertainty in I was the error in s, the crystal separation, which was only known to the nearest mm. This causes an uncertainty in I of ± 9%.

4.8c Compton cross-section

The value of

$$\int_{T_b}^{T_{max}} \frac{d\sigma_\gamma}{dT} \, dT$$

of Eq. 4.8.1 is required. The relevant equations are given in Appendix C and the results for T_b = 0, and T_b = .34 MeV are shown in Fig. 4.4.
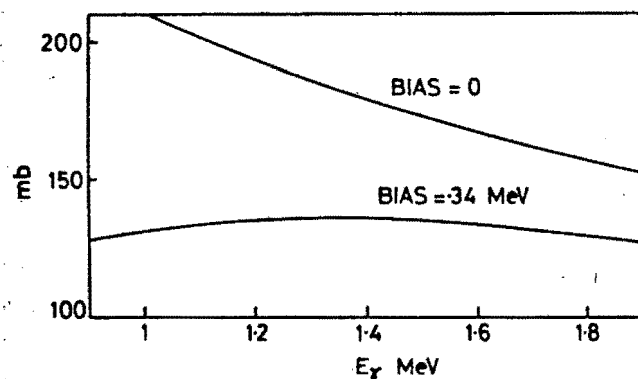
Fig. 4.4

Cross-sections for Compton scattering, electron bias = 0 and 0.34 MeV.

It is found that the cross section with the bias of 0.34 MeV varies very little over the observed range of photon energies (0.9 - 1.9 MeV), and a mean value of 133.0 mb was used giving a maximum error of 2%.

4.8d Multiple scatter and escape contribution

We now consider what processes, other than direct detection by Compton scattering in the stilbene crystal, could affect e_γ. The npB photon could cause a Compton process in any of the material surrounding the crystal, and the scattered photon could be detected, or the scattered electron could pass into the crystal. These processes would increase e_γ. On the other hand if a Compton scatter occurred in the normal way inside the crystal but close to its surface, the scattered electron could escape and if the energy deposited in the crystal was less than the bias level, the event would not be detected.

A quantitative analysis of the above contributions would be complex. However, an approximate treatment was undertaken by estimating, for a mean photon energy of 1.5 MeV, the order of thickness of crystal on the light-guide side rendered useless for detection by electron escapes; this is $\simeq$ 1.0 mm (the physical crystal thicknesses are 12.3 and 11.5 mm). Similarly, for escapes into the crystal, $\simeq$ 1.4 mm of the material between the crystals can be considered as adding to the detector volume. The same approach applied to the curved surface shows that the effects cancel within a few percent. Bearing in mind the large uncertainty in the final npB cross-section figure, no further effort to improve these estimates was warranted, and the effects were disregarded.

4.8e Comparison with rates from a ^{60}Co source

A ^{60}Co source of known activity was attached to the curved surface of the scattering chamber opposite the crystals, and the nett count rate at each detector recorded. These rates were compared with those predicted by a formula similar to Eq. 4.8.1 as follows:

$$N_\gamma = N \frac{\sigma_\gamma n_e}{4\pi} \int dV \left(\frac{e^{-\sigma_\gamma n_e m}}{\ell_c^2} \right) \qquad 4.8.3$$

where

N_γ = recorded rate at detector

N = activity of source = 52.23×10^4 sec^{-1}

σ_γ = total Compton cross section at 1.25 MeV = 188.6 mb

n_e = electron density in stilbene = 3.70×10^{23} cm^{-3}

m = distance of volume element from crystal surface

ℓ_c = separation of source from centre of crystal = 15.1 cm .

Since the exponential term is close to 1, we take it outside the integral and use a mean value for m. Thus $\overline{m} = 1.7$ cm, and:

$$N_\gamma \simeq \frac{N\sigma_\gamma n_e V}{4\pi \ell_c^2} e^{-\sigma_\gamma n_e \overline{m}} \qquad 4.8.4$$

The results were as follows:

	Measured rate, Hz	Calculated rate, Hz	Difference %
det. 1	213.7	175.3	21.9
det. 2	174.9	149.8	16.8

The main difference between this comparison and the actual experimental conditions is that the photons are here travelling normal to the crystal axis. This renders a large portion of the light guide and other crystal available for multiple scatters, and the above differences are attributed to this. An accurate calculation of this contribution would be difficult, and the comparison as it stands shows that there was no gross underestimation of e_γ.

4.8f Results

It remains to insert the calculated values from Sects. 4.8b and c into Eq. 4.8.1 with the following results:

	det. 1	det. 2	Uncertainty
e_γ	.0147	.0125	± 9%

4.9 DETERMINATION OF NEUTRON DETECTION EFFICIENCY, e_n

The equation used for calculating σ_{br}, Eq. 4.5.2, contains the neutron detection efficiency e_n, which is a function of E_n. The normalisation factor k (Eq. 4.3.1) is also proportional to e_n; thus the absolute value is not required, and sufficiently accurate figures for the relative efficiency can be obtained from:

$$e_n(E_n) = \frac{E_n - E_B}{E_n}\left(1 - e^{-\sigma_{el}(E_n)n_n x_n}\right) \qquad 4.9.1$$

where

E_n = neutron energy

E_B = detector bias level

$\sigma_{el}(E_n)$ = n-p elastic cross-section

x_n =   detector thickness

n_n =   proton density in detector

Eq. 4.9.1 takes no account of multiple scattering and the efficiency curve
is shown in Fig. 4.5,
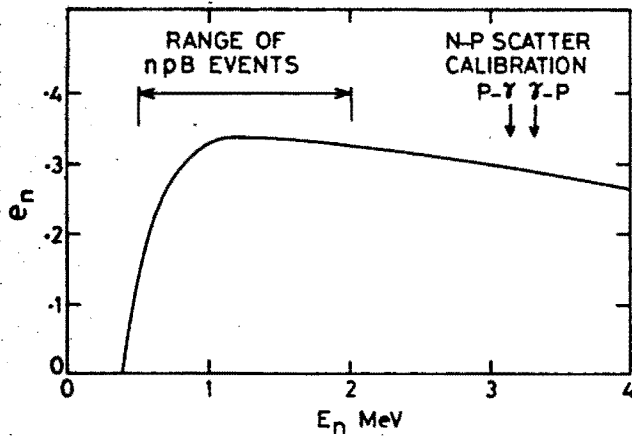
Fig. 4.5

Neutron detection efficiency (of
detector 3).

CHAPTER 5

THEORETICAL ASPECTS

5.1 INTRODUCTION

Although the theoretical framework for NNB was known as early as 1949 [30], the subject only began to gather momentum around 1963 with the ppB experiments of Gottschalk et al. [31] and the theoretical work of Sobel and Cromer [32]. The basis of the theory is now well established and parts of the non-relativistic approach are reproduced in Sects. 5.2 and 5.3 with the treatment broadly following that of Cromer and Sobel [33].

Two important model-independent methods are then discussed, the on-energy-shell (OES) approximation (Sect. 5.4), from which an analytic prediction of cross-section is made corresponding to this experiment, and the soft-photon approximation (SPA) (Sect. 5.5) which uses the Low theorem. The status of npB calculations is reviewed in Sects. 5.6 and 5.7 with the latter devoted to the low-energy region of this experiment. Finally (Sect. 5.8) we consider the problem of comparing Harvard (coplanar) cross-section predictions with results from experiments which have finite-sized detectors and hence allow non-coplanar events.

5.2 BASIC FORMULATION

In this section we show how the cross-section can be expressed in terms of off-shell elements of the 2-nucleon transition matrix (T-matrix).

The T-matrix element for production of a photon by NNB is, in the distorted-wave Born approximation:

$$T_{fi} = <\chi_f^- |V_{em}| \chi_i^+>$$

$$5.2.1$$

where V_{em} is the electromagnetic interaction and $|\chi^+>$ ($|\chi^->$) is the exact outgoing (incoming) 2-nucleon scattering state resulting from the nuclear interaction alone.   It is a solution of the Schrödinger equation:

$$|\chi_j^\pm> = |\phi_j> + G_j^\pm V_N |\chi_j^\pm>$$

$$5.2.2$$

where $G_j^\pm = 1/(E_j - H_o \pm i\eta)$ is the Green's function for a free 2-nucleon system of energy E_j, whose Hamiltonian is H_o. $|\phi_j>$ is the free plane-wave state

and V_N the nuclear potential.

In these formulae, the N-N interaction is treated exactly, whilst the use of only the first Born order of the electromagnetic interaction is justified by its comparitively weak coupling (see e.g. Nyman [34]).

Substituting Eq. 5.2.2 into 5.2.1:

$$T_{fi} = <\phi_f | V_{em} | \phi_i >$$
$$+ <\phi_f | V_{em} G_i^+ V_N | \chi_i^+ >$$
$$+ <\chi_f^- | V_N G_f^- V_{em} | \phi_i >$$
$$+ <\chi_f^- | V_N G_f^- V_{em} G_i^+ V_N | \chi_i^+ >$$

5.2.3

The first term of Eq. 5.2.3 corresponds to photon emission by non-interacting nucleons which violates conservation of energy/momentum. The remaining terms can be represented in diagrams (Fig. 5.1). Terms 2 and 3
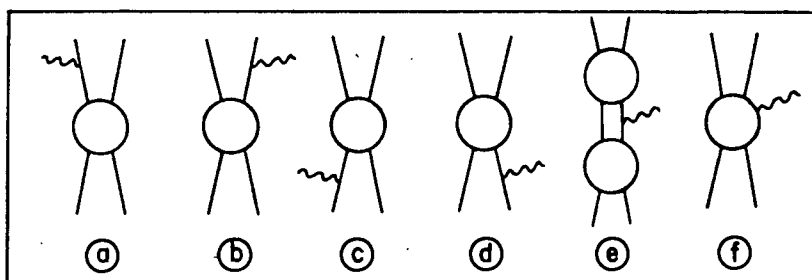
Fig. 5.1

Photon emission diagrams.
(a)-(d) : external emission
(e)   : rescattering }
(f)   : meson exchange } internal emission.

correspond to photon emission by one of the nucleons after and before the nuclear interaction respectively (external emission, single scattering or pole terms), while term 4 corresponds to photon emission between two nuclear interactions (double scattering or rescattering). The last diagram (Fig. 5.1f) is not covered by the theory presented here and represents photon emission by 'interaction currents' or 'meson-exchange currents'. Only the pole terms will be considered in the following and the internal scattering contributions are discussed in Sect. 5.6.

On inserting explicit forms for the Green's function and the electromagnetic interaction (the manipulations appear in Appendix F), the contribution to T_{fi} from the pole terms (Fig. 5.1(a)-(d)) becomes:

$$
T_{fi} = -\sqrt{\frac{2\pi\alpha}{P_\gamma m^2}} \left\{ \frac{\left(\varepsilon_1(\hat{\varepsilon}\cdot\underline{P}_1') - \tfrac{1}{2}i\mu_1\,\underline{\sigma}_1\cdot(\underline{P}_\gamma \times \hat{\varepsilon})\right)<\underline{P}_1' + \underline{P}_\gamma,\underline{P}_2'|T_N(E_i)|\underline{P}_1,\underline{P}_2>}{E_i - E(\underline{P}_1' + \underline{P}_\gamma,\underline{P}_2')} \right.
$$

$$
+ \frac{\left(\varepsilon_2(\hat{\varepsilon}\cdot\underline{P}_2') - \tfrac{1}{2}i\mu_2\,\underline{\sigma}_2\cdot(\underline{P}_\gamma \times \hat{\varepsilon})\right)<\underline{P}_1',\underline{P}_2' + \underline{P}_\gamma|T_N(E_i)|\underline{P}_1,\underline{P}_2>}{E_i - E(\underline{P}_1',\underline{P}_2' + \underline{P}_\gamma)}
$$

$$
+ \frac{\left(\varepsilon_1(\hat{\varepsilon}\cdot\underline{P}_1) - \tfrac{1}{2}i\mu_1\,\underline{\sigma}_1\cdot(\underline{P}_\gamma \times \hat{\varepsilon})\right)<\underline{P}_1',\underline{P}_2'|T_N(E_f)|\underline{P}_1 + \underline{P}_\gamma,\underline{P}_2>}{E_f - E(\underline{P}_1 - \underline{P}_\gamma,\underline{P}_2)}
$$

$$
\left. + \frac{\left(\varepsilon_2(\hat{\varepsilon}\cdot\underline{P}_2) - \tfrac{1}{2}i\mu_2\,\underline{\sigma}_2\cdot(\underline{P}_\gamma \times \hat{\varepsilon})\right)<\underline{P}_1',\underline{P}_2'|T_N(E_f)|\underline{P}_1,\underline{P}_2 - \underline{P}_\gamma>}{E_f - E(\underline{P}_1,\underline{P}_2 - \underline{P}_\gamma)} \right\}
$$

<div align="right">5.2.4</div>

Notation used in Eq. 5.2.4 is as follows:

α $= e^2/\hbar c = 137^{-1}$ is the fine structure constant

$\hat{\varepsilon}$ = a unit vector in the direction of the photon's polarisation

ε_j = charge on j^{th} nucleon in units of electronic charge

μ_j = magnetic moment of jth nucleon in units of $e\hbar/2\,mc$

m = nucleon mass

$T_N(E)$ = 2-nucleon transition operator

P_j = centre-of-mass momenta (see Sect. 5.6) where primes refer to final states, non-primes to initial states

E_i $= E(\underline{P}_1,\underline{P}_2) = P_1^2/2m + P_2^2/2m$ etc.

The units are such that $\hbar = 1$.

Underlined symbols are vectors.

Eq. 5.2.4 contains the 2-nucleon off-shell T-matrix elements, for instance, in the first term we have $<\underline{P}_1' + \underline{P}_\gamma,\underline{P}_2'|T_N(E_i)|\underline{P}_1,\underline{P}_2>$. The transition operator here is a function of the initial energy, but is between states whose energies are different; $|\underline{P}_1,\underline{P}_2>$ is the initial state and $|\underline{P}_1' + \underline{P}_\gamma,P_2'>$ is the intermediate state. It can be noted that the intermediate energy state for these pole terms is unique; evaluation of the rescattering term is more difficult and would require an integral over intermediate states.

The NNB cross-section is related to T_{fi} by time-dependent perturbation theory:

$$d\sigma = \frac{2\pi}{v_1}|T_{fi}|^2 d\rho \qquad\qquad 5.2.5$$

where $v_1 = P/m$ is the initial relative velocity of the nucleons (we use the notation for laboratory momenta that P = initial momentum; P_1, P_2 = final momenta), and:

$$d\rho = \frac{1}{(2\pi)^6}\int \delta^3(\underline{P} - \underline{P}_1 - \underline{P}_2 - \underline{P}_\gamma)\,\delta(E - E_1 - E_2 - E_\gamma)\,d^3P_1 d^3P_2 d^3P_\gamma$$

where the integral is taken over any 4 of the 9 laboratory variables which will remove the delta functions. In the present case, the cross-section is to be for Harvard geometry (Sect. 1.3), hence we integrate over $dP_1 dP_2 dP_\gamma d\phi_\gamma$ and then set up $\phi_\gamma = 0$. The result is (see e.g. Liou and Sobel [35]):

$$\frac{d\rho}{d\Omega_1 d\Omega_2 d\theta_\gamma} = F = \frac{1}{(2\pi)^6}\frac{P_1{}^2 P_2{}^2 P_\gamma / c}{\sin(\theta_1+\theta_2) - \frac{P_1}{mc}\sin(\theta_2-\theta_\gamma) - \frac{P_2}{mc}\sin(\theta_1+\theta_\gamma)} \qquad 5.2.6$$

F is known as the phase-space factor or density of final states, in this case for Harvard geometry. The angles $\theta_1, \theta_2, \theta_\gamma$ are defined in Fig. 5.2.
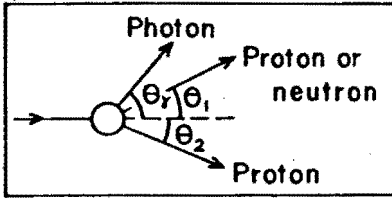
Fig. 5.2

Definition of angles of outgoing particles.

Using Eqs. 5.2.4, 5.2.5 and 5.2.6, an NNB cross-section can be calculated from 2-nucleon T-matrix elements. The latter can be obtained from a potential model or from 'quasi-phases', as outlined in the next section. In doing so, nucleon spin would have to be incorporated, and the momentum-space T-matrix elements would each become a 4×4 matrix in spin-space (M matrix). The computation would then include an initial spin average and final spin sum of amplitudes. These procedures are standard practice in on-shell calculations.

5.3 QUASI-PHASE PARAMETERS

Elastic N-N collision data are usually analysed in terms of phase-shifts and coupling parameters (e.g. Stapp et al. [36]). These phase parameters are still energy dependent, but remove the dependence on angle and on the particular elastic observable (cross-section or polarization) being measured. As such they are an intermediate step between experimental data and potential model. The virtue of this procedure is that a large number of data points can be reduced to a smaller number of parameters where this number depends on a cutoff at some point in the partial wave series. The connection between phase parameters and elastic observables was given by Wolfenstein [37], and the theory and techniques of phase-shift analysis are covered in several reviews [38].

In the off-shell case an analogous system exists [39] in which the meeting point between potential and data is, in addition to the on-shell parameters, a set of off-shell quasi-phases. The formalism is indicated in the following, where spin is disregarded for simplicity.

The transition amplitude for a 2-nucleon collision is:

$$t(\underline{k}',\underline{k}) = -\frac{m}{4\pi}<\phi_{\underline{k}'}|V_N|\chi_{\underline{k}}^+> = -\frac{m}{4\pi}\int d^3r\, e^{-i\underline{k}'\cdot\underline{r}}V_N(r)\chi_{\underline{k}}^+(\underline{r}) \qquad 5.3.1$$

where $\underline{k}(\underline{k}')$ is the initial (final) centre-of-mass momentum, and $\hbar = 1$.

If $|\underline{k}'| = |\underline{k}|$, $t(\underline{k}',\underline{k})$ is on-shell and can be represented as a sum of partial waves,

$$t(\underline{k}',\underline{k}) = \frac{1}{k}\sum_{\ell}(2\ell+1)\sin\delta_\ell\, e^{i\delta_\ell}P_\ell(\hat{\underline{k}}'\cdot\hat{\underline{k}}) \quad . \qquad 5.3.2$$

The phase shift, δ_ℓ, appears in the asymptotic form of the solution to the radial Schrödinger equation:

$$y_\ell(kr) \underset{r\to\infty}{=} \sin(kr - \ell\pi/2 + \delta_\ell)$$

An integral equation for δ_ℓ in terms of the potential V_N can then be derived:

$$\sin\delta_\ell = -m\int_0^\infty j_\ell(kr)V_N(r)y_\ell(kr)r\, dr \qquad 5.3.3$$

where j_ℓ are spherical Bessel functions.

If $|\underline{k}'| \neq |\underline{k}|$, the amplitude $t(\underline{k}',\underline{k})$ is off-shell and can be identified with any of the amplitudes of Eq. 5.2.4. By analogy with Eq. 5.3.3, the quasi-phase is then defined by:

$$\Delta_\ell(\underline{k}',\underline{k}) = - m \int_0^\infty j_\ell(k'r) V_N(r) y_\ell(kr) r \, dr \qquad 5.3.4$$

It can then be shown that the partial wave expansion is the same as Eq. 5.3.2 with $\sin \delta_\ell$ replaced by $\Delta_\ell(\underline{k}',\underline{k})$. The transition amplitude can thus be found from a set of quasi-phases which in turn can be derived from a potential model.

Although the above formalism is of value to the theory, only one explicit calculation of quasiphases from data is known [40]. This was made from a comprehensive ppB experiment at 42 MeV [41] and with large uncertainty.

5.4 THE ON-ENERGY-SHELL (OES) APPROXIMATION

The calculation of NNB cross-sections from potentials has been outlined in the previous sections; however there exist two approximation methods for obtaining cross-sections from on-shell information such as phase parameters. One of these, the soft-photon approximation (SPA), will be detailed in Sect. 5.5, and the other we shall call the on-energy-shell (OES) approximation. Both methods have achieved success, in restricted kinematic regions, in making predictions which compare favourably with experiment, but they ignore off-shell effects.

We now use the OES approximation, in which the off-shell N-N amplitudes of Eq. 5.2.4 are simply replaced by their on-shell counterparts, to arrive at an analytic expression for the npB cross-section. The method is due to Feshbach and Yennie [42] and our treatment is adapted from that of Signell [43]. We also use the inequalities $P \ll mc$ (P = incident laboratory momentum) and $P_\gamma \ll P$ which apply at the low energies of this experiment.

Using the low energy expressions for P_1 and P_2 (Appendix A.2a), and noting that $P_1/mc \ll 1$ and $P_2/mc \ll 1$, the phase-space factor of Eq. 5.2.6 is:

$$F = \frac{1}{(2\pi)^6} \frac{\sin^2\theta_n \sin^2\theta_p P^4 P_\gamma/c}{\sin^5(\theta_n+\theta_p)}$$

where suffices n, p now refer to outgoing neutron and proton. Whence, using Eq. 5.2.5,

$$\frac{d\sigma}{d\Omega_n d\Omega_p d\theta_\gamma} = \frac{1}{(2\pi)^5} \left(\frac{m}{P}\right) |T_{fi}|^2 \frac{\sin^2\theta_n \sin^2\theta_p P^4 P_\gamma/c}{\sin^5(\theta_n+\theta_p)} \qquad 5.4.1$$

Now T_{fi} must be calculated from Eq. 5.2.4. Considering first the energy denominators, for instance, for the first term of Eq. 5.2.4:

$$E_i - E(\underline{P}'_1 + \underline{P}_\gamma, \underline{P}_2) = E_f + cP_\gamma - E(\underline{P}'_1 + \underline{P}_\gamma, \underline{P}'_2)$$

$$= \frac{P'^2_1}{2m} + \frac{P'^2_2}{2m} + cP_\gamma - \frac{(\underline{P}'_1 + \underline{P}_\gamma)^2}{2m} - \frac{P'^2_2}{2m}$$

$$\simeq cP_\gamma - \underline{P}'_1 \cdot \underline{P}_\gamma / m$$

$$\simeq cP_\gamma$$

Next we make the on-shell approximation, thus for the first term of Eq. 5.2.4,

$$< \underline{P}'_1 + \underline{P}_\gamma, \underline{P}'_2 | T_N(E_i) | \underline{P}_1, \underline{P}_2 > = - (4\pi/m) t(E_i)$$

where t is the on-shell transition amplitude. Following previous notation we let $t = t(E_i)$, $t' = t(E_f)$.

Finally, omitting the magnetic moment interaction (see Sect. 5.7), and noting that for npB, $\epsilon_1 = \epsilon_n = 0$, $\epsilon_2 = \epsilon_p = 1$, Eq. 5.2.4 becomes:

$$T_{fi} = \frac{4\pi}{m} \sqrt{\frac{2\pi\alpha}{P_\gamma m^2}} \frac{1}{cP_\gamma} T'$$

5.4.2

with $T' = ((\hat{\epsilon} \cdot \underline{P}'_p) t - (\hat{\epsilon} \cdot \underline{P}_p) t')$

Now $\underline{P}_p$ and $\underline{P}'_p$ are centre-of-mass momenta of the proton (see Sect. 5.6) and these must be expressed in terms of the laboratory variables. Assuming, for the moment, that the photon polarization vector, $\hat{\epsilon}$, lies in the experimental plane, and using the results from Appendix A,

$$T' = \frac{p}{2} \cdot \frac{(t+t') \sin\theta_n \sin(\theta_p - \theta_\gamma) + (t-t') \sin\theta_p \sin(\theta_n + \theta_\gamma)}{\sin(\theta_n + \theta_p)}$$

5.4.3

This expression demonstrates the dipole (E1) radiation pattern; at low energies, t and t' are nearly equal, hence the cross-section depends on θ_γ through the term $\sin^2(\theta_p - \theta_\gamma)$. The null of the radiation pattern coincides with the outgoing proton, as would be expected from a classical theory (see Sect. 5.8).

The required npB cross-section is now obtained from these equations by integrating $|T_{fi}|^2$ with respect to θ_γ, substituting the lowest order expression for P_γ (Appendix A.2a) and taking the initial spin average and final spin sum. Since we are only concerned with s-wave interactions, this latter operation simplifies to an average over the singlet and triplet amplitudes:

$$|T'|^2 = \frac{1}{4}|T'_s|^2 + \frac{3}{4}|T'_t|^2 \ .$$

A sum over photon polarizations, $\hat{\epsilon}$, is also required; however with the choice of transverse gauge (Appendix F), this can be simplified to summation over any two directions mutually perpendicular to $\underline{P}_{-\gamma}$. In the coplanar situation considered (Harvard geometry), we take these two directions to be in the plane and normal to it. However by virtue of the terms $\hat{\epsilon}.\underline{P}'_{-p}$ and $\hat{\epsilon}.\underline{P}_{-p}$ in Eq. 5.4.2, there is no contribution if $\hat{\epsilon}$ is normal to the plane, hence we may consider the photons as being polarized in the experimental plane, and disregard the sum.

The final result is then:

$$\frac{d\sigma}{d\Omega_n d\Omega_p} = \frac{\alpha}{16\pi}\left(\frac{P}{mc}\right)\frac{|A_s|^2 + 3|A_t|^2}{\sin^3(\theta_n+\theta_p)\cos^2(\theta_n+\theta_p)} \qquad 5.4.4$$

where

$$|A|^2 = |t+t'|^2\sin^2\theta_n + |t-t'|^2\sin^2\theta_p - 2(|t|^2 - |t'|^2)\sin\theta_n\sin\theta_p\cos(\theta_n+\theta_p)$$

and t,t' are scattering amplitudes, given in the effective range theory by:

$$t = \frac{1}{-iP_1 + 1/a - rP_1^2/2} \ , \quad t' = \frac{1}{-iP'_1 + 1/a - rP_1'^2/2}$$

The cross-section calculated from Eq. 5.4.4 corresponding to this experiment with E = 4.77 MeV, $\theta_n = 35^0$, $\theta_p = 25^0$ is $d\sigma/d\Omega_n d\Omega_p = 89$ $\mu b/sr^2$, where the following values for the effective range parameters have been used:

singlet : a_s = -23.71 , r_s = 2.73
triplet : a_t = 5.43 , r_t = 1.74 .

The above theory has been equally applied to ppB; however it is found that a higher order of approximation of the energy denominators must be used, otherwise the cross-section vanishes. This means that ppB cross-sections are lower than npB (e.g. by a factor of $\simeq$ 10 at 60 MeV [6] or $\simeq$ 100 at 10 MeV [44]) and gives rise to the characteristic quadrupole radiation pattern for ppB.

Low energy ppB calculations using this OES approximation have been very successful, but so far as is known, there has been no appraisal of OES npB results. The validity of the approximation is discussed in Sect. 5.7.

5.5 THE LOW THEOREM

The NNB cross-section, expressed for any geometry, approaches infinity in the limit of zero photon energy. This 'infra-red divergence' can be seen in our OES calculations, Eq. 5.4.4; in this case the singularity is contained in the factor $1/\cos^2(\theta_n + \theta_p)$, because the photon energy becomes zero in the elastic limit when $(\theta_n + \theta_p) \to \pi/2$. As a result of this behaviour, Low [45] expanded the NNB amplitude, t, in powers of photon energy, k; as $t = t_{-1}/k + t_0 + t_1 k \ldots$, and found that the first two terms of this series can be exactly calculated from on-shell information. This is the Low theorem. It is based on gauge invariance, and Low's original proof used quantum field theory, but the result has since been shown to hold when t is derived from a potential model which can include nonlocal terms [46,47].

The Low theorem naturally leads to the soft-photon-approximation (SPA) in which the cross-section is calculated from on-shell parameters as the first two terms of the Low series. Whereas the OES approximation has achieved good results for low incident energy ppB, SPA is useful when the energy of the photon is low relative to that of the nucleons. Like OES, SPA makes no forecast of off-shell effects, and the inquiry into the off-shell interaction is one of the main motives for studying NNB. Moreover, the theorem does not imply that higher terms in the series are devoid of on-shell information, so that one cannot determine the off-shell contribution as a difference between an SPA calculation and a more complete one [48].

Besides excluding off-shell effects, SPA is not good for typical Harvard experiments. Low's prescription used, as dimensionless expansion parameter, $k/\bar{E}$ [43] where $\bar{E} = (E_i + E_f)/2$, the average of the initial and final N-N energies in the centre-of-mass, although there are apparently other allowable choices [49]. For Harvard geometry at typical angles of $\theta_1 = \theta_2 = 30^0$, we find $k/\bar{E} = $ unity, indicating zero convergence of the Low series. Finally, Liou [50] claims that SPA is invalid for Harvard geometry as, for a given choice of θ_1, θ_2 such that $\theta_1 + \theta_2 < 90$, k is constrained to be non-zero and hence the limit $k \to 0$ cannot be taken.

As a test of SPA, Signell [43] has compared cross-section calculations

against potential model results for ppB at 10 MeV and has shown that the SPA value is lower by 20% at $\theta_1 = \theta_2 = 30^0$. At the same point, an OES calculation was within 1% of the potential model prediction.

The Low theorem has however received much attention and several extensions have been made. Burnett and Kroll [51] expanded the NNB cross-section in powers of k and showed that the first two terms of this series can be determined from the corresponding elastic cross-section. Fearing [52] generalised this result to include polarized NNB cross-sections, and Nefkens et al. [53] have introduced the concept of external-emission dominance (EED), in which only the first term of Burnett and Kroll's expansion is retained, to account for experimental ppB results at 730 MeV. Of particular relevance to npB, the Low theorem has been used for calculating the order k^0 contribution to internal scattering (Sect. 5.6).

Aside from its calculational uses, the most significant result of the Low theorem is its implication for experimental planning. Off-shell behaviour is only contained in the order k and higher terms, hence, as the aim is to study such behaviour, experiments should be designed to maximise $k/\bar{E}$. In Harvard geometry this means working at small angles θ_1 and θ_2.

5.6 REVIEW OF npB CALCULATIONS

Most of the npB predictions have been at 130 MeV and 200 MeV corresponding to the two main experiments (Table 1.1). We now examine some of the features of the calculations; the lower energy region corresponding to this experiment will be discussed in the next section. Firstly, we make some general comments relevant to NNB as a whole.

The theory presented so far (Sects. 5.2 - 5.4) omitted a number of parts of the NNB amplitude. Whilst this may be justified at low energies (Sect. 5.7), a realistic calculation must consider all possible contributions including internal scattering (rescattering and meson-exchange). The rescattering term can be calculated exactly [54] but the meson-exchange term cannot, and this is the subject of much of the recent theoretical work in NNB (e.g. [55]).

A brief survey of NNB calculations up to 1975 has been made by Srivastava and Sprung [56]. Following the experimental trend, most theorists have concentrated on ppB rather than npB. After some initial confusion caused by errors in Sobel and Cromer's original work [32], there is now broad agreement, for ppB, between experiment and theory; however there are discrepancies in detail [5].

One of the errors in the early work was caused by the evaluation of the NNB amplitude, T_{fi}, in the laboratory frame. All calculations used the transverse gauge for the emitted photon, and gauge invariance then implies that, for ppB, if T_{fi} is evaluated in the centre-of-mass frame, internal scattering contributions are of order k or greater in the Low series [57 - 59]. This means that centre-of-mass ppB calculations involving only the pole terms can provide good approximations. For instance, Brown [54] computed Harvard ppB cross-sections at $\theta_1 = \theta_2 = 30^0$ and found by explicit calculation that the rescattering contributions were 0.2% at 62 MeV and 15% at 300 MeV.

For npB, T_{fi} should also be evaluated in the centre-of-mass frame as was done in Sect. 5.4, but internal scattering is now present down to order k^0 in the Low series [58,59]. From the more recent calculations [60,61] it is evident that internal terms are of the same magnitude as the pole terms at least above 100 MeV.

Table 5.1 lists known npB calculations at 130 MeV and 200 MeV, and the results are all shown at Harvard scattering angles $\theta_n = \theta_p = 30^0$ for comparison. Of the potential model calculations, that of Pearce et al. [62] included no internal scattering and neglected partial waves above $J = 2$, and the results are evidently too low. All later calculations included some internal scattering. Brown [65] included rescattering to all orders but no exchange effects, Celenza et al. [67] used the Low theorem (Sect. 5.4) to calculate the internal scattering contribution (both rescattering and exchange) to order k^0, and Brown and Franklin [60] included rescattering to all orders and exchange effects to order k^0. Finally, Bohannon [61] used an alternative to the Low theorem for estimating internal scattering; he expanded, in powers of k, the electromagnetic current instead of the transition amplitude, and retained only the lowest order.

The difficulty of calculating higher-order corrections to the exchange contribution stems from a basic ignorance about the strong-interaction dynamics, in that no potential model gives an unambiguous prescription for treating these terms [68,60,61]. However, Brown and Franklin estimated such higher orders to be small, and this view is supported by the convergence of the later calculations with the experimental value at 200 MeV. On the other hand, there is no such agreement at larger angles or at 130 MeV.

It may be noted from Table 5.1 that where the same calculations have been made with different potentials, there is very little difference in the results. This has become a general feature of NNB; the model-dependence of NNB cross-sections has always been found to be small. For npB in particular, with

Author	Year	Ref.	Cross-section, $\mu b/sr^2$		Basis and Comments
			130 MeV	200 MeV	
Pearce et al.	1967	62	8	5	Tabakin potential. Pole terms only. $J \leqslant 2$
Nyman	1968	63		23	Soft-photon approximation. No off-shell contribution.
Baier et al.	1969	64	45	46	One-boson-exchange model. Relativistic, gauge invariant.
Brown	1970	65		45 48	Hamada-Johnston potential.⎫ Pole & rescattering contribution Bryan-Scott III potential.⎭ to all orders in k. $J \leqslant 4$
McGuire	1970	66	29 36	26 35	On-shell approximation (model 'Oeℓ') Off-shell extrapolation of quasi-phases (model 'O')
Celenza et al.	1972	67	18	30	Hamada-Johnston potential. Internal scattering to order k^0.
Brown & Franklin	1973	60	30.6	34.6	Hamada-Johnston potential.⎫ Rescattering to all orders of k. Bryan-Scott III potential.⎭ Exchange contribution to k^0. $J \leqslant 4$
Bohannon	1978	61		33.4 33.2 - 36.3	Hamada-Johnston potential.⎫ Internal scattering to lowest Lomon-Feshbach potential. ⎭ order of k (see text). $J \leqslant 4$
MEASURED VALUES		10	77 ± 32		Measurement at $\theta_n, \theta_p = 29^0, 32^0$.
		9		35 ± 14	Measurement at 208 MeV.

Table 5.1:   npB cross-section predictions at $\theta_n, \theta_p = 30^0$, E = 130 and 200 MeV. Most of the calculations also included other angle pairs.

available experimental accuracy, there is little hope of being able to distinguish the various potential models.

Of the model-independent npB calculations, those of McGuire [66] require explanation. McGuire used a method based on one-pion exchange to extrapolate the on-shell phase shifts into quasi-phases (model 'O'). He then replaced the quasi-phases by the phase shifts (model '$O_{e\ell}$') for comparison. The object was to find how off-shell effects varied with the different kinematic regions, rather than to provide accurate cross-section predictions, and similar calculations were done for ppB [58,69]. For ppB McGuire included only the pole terms; for npB he also calculated the k^0 internal scattering contribution using the Low theorem in a similar manner to Celenza et al.

npB calculations have reached a level of sophistication which is by no means matched by experiment. It would therefore be of great value if further npB experiments of better accuracy could be undertaken which would distinguish between the different techniques used in the calculations.

5.7 ' LOW-ENERGY npB CALCULATIONS: COMPARISONS WITH THIS EXPERIMENT

Fig. 5.3 shows known npB predictions in the range 2-20 MeV, and it is unfortunate that they are so few. Of the calculations listed in Table 5.1, only those of Baier et al. [64] and McGuire [66] continue into this energy region, and Baier et al.'s results are unreliable as admitted by the authors.
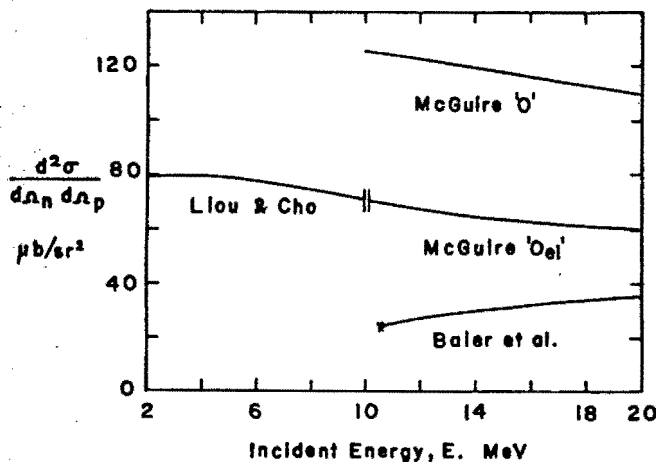

Fig. 5.3
npB cross-section predictions, Harvard geometry, $\theta_n = \theta_p = 30^0$.

This is because their one-boson-exchange model does not correctly reproduce the s-wave phase shifts [66] which dominate the N-N interaction at these energies. There is also one calculation, that of Liou and Cho [44] devoted to the low

energy region.   Table 5.2 summarises the predictions which may be compared
with this experiment.

	Ref.	10 MeV $\theta_n = \theta_p = 30^0$	4.8 Mev $\theta_n = 35^0$, $\theta_p = 25^0$
McGuire 'O'	66	125	140 †
McGuire 'O$_{e\ell}$'	66	70	83 †
Liou and Cho	44	70	84 ‡
OES		76	89
Experimental value			60 ± 150

Table 5.2:   Predictions of cross sections.   Values are of $d^2\sigma/d\Omega_n d\Omega_p$ in $\mu b/sr^2$
for Harvard geometry.   The values of the on-energy-shell
approximation (OES) are from our own calculations (Sect. 5.4).
Off-shell effects are only included in the McGuire 'O' and Liou
and Cho results.
† Values extrapolated from 10 MeV, $\theta_n = \theta_p = 30^0$ results.
‡ Value extrapolated from 4.8 MeV, $\theta_n = \theta_p = 30^0$ result.

McGuire's 'O$_{e\ell}$' calculation (see Sect. 5.6) appears similar to the
on-energy-shell approximation (OES) (Sect. 5.4) and the 10 MeV, $\theta_n = \theta_p = 30^0$
values support this.   Neither of these results is expected to be exact as
off-shell effects are excluded;   however their similarity may give credence to
McGuire's 'O' results which include off-shell effects.

McGuire's 'O' results have achieved general agreement with experiment for
higher energy npB [6] and over the range of ppB [69] except at very forward
angles [70];   however the differences between 'O' and 'O$_{e\ell}$' are of the same
magnitude or smaller than the experimental uncertainties.   Moreover, the
author states that the 'O' curve was intended not necessarily to give all the
correct off-shell effects but rather to show where these effects are most marked.
The difference between 'O' and 'O$_{e\ell}$' is greater in the region under consideration
than in most others.   There is also strong disagreement between 'O' and Liou
and Cho's prediction.

Liou and Cho's calculations used the Hamada-Johnston potential in the
laboratory frame;   they then found it necessary to include a rescattering term
to satisfy gauge invariance.   Whilst this procedure is justifiable, although
unusual, they are only able to show that gauge invariance holds when an
assumption is made that the amplitude for photon emission from the

proton is the same as from the neutron.   Since the electric terms
dominate and the neutron is uncharged, this assumption can hardly be correct.

In order to find out what realistic theoretical value may be compared with
this experiment, we have examined the possible errors in the OES result and the
following have been discounted:

i)   magnetic pole contribution.   This is estimated at < 1% of the E1
contribution at 4.77 MeV;

ii)   internal scattering.   At 4.77 MeV we need only consider s-waves in the
N-N interaction;   thus rescattering cannot occur as the initial s-state
interaction followed by photon emission can only provide a p-state for the
final strong interaction [43,71].

Meson exchange effects are also expected to be negligible.

If the correct cross-section value is indeed much higher than the OES
result, then the only remaining possibility is that the off-shell amplitudes
t and t′ (Eq. 5.4.2) are very different from the on-shell values, i.e. that
the on-shell approximation itself is bad.

This is unlikely.   ppB calculations using OES-type approximations have
achieved close agreement with exact calculations and experiment at 20 MeV [72]
and lower energies [73 - 75] when Coulomb corrections are included.   This
success is attributed to a partial cancellation of off-shell differences [72];
the on-shell value of t is too low whilst t′ is too high by a roughly equal
small amount.   However, a similar cancellation would also occur for npB
(Eq. 5.4.3).   On this basis we should expect that off-shell effects would only
alter the OES value by $\lesssim$ 1%.   If Liou and Cho's calculations are correct, this
notion would be corroborated.

, The likely conclusions are that the OES value of 89 $\mu b/sr^2$ is close to
correct, that off-shell effects are small at these energies, and that McGuire's
'O' result is not correct.

5.8   NONCOPLANARITY

The NNB cross-section varies rapidly as the noncoplanarity angle, $\beta_p^{\dagger}$, is
varied from zero to its maximum value, β_{pm}.   Since β_{pm} is small, many experiments
have used detectors which cover an appreciable fraction of the allowed range of
β_p, and hence are not directly comparable with Harvard calculations which assume

---

† Angle β_p is defined in Fig. 4.1 and, for symmetrical geometry ($\theta_1 = \theta_2$), is
   twice the angle ϕ used by others.   See e.g. Gottschalk et al. [76].

strict coplanarity. The difficulty worsens towards lower energies as β_{pm} reduces; for instance, for $\theta_1 = \theta_2 = 30^0$, at 200 MeV, $\beta_{pm} = 10.4^0$; at 4.8 MeV, $\beta_{pm} = 1.7^0$. As an addendum to this chapter we mention how this problem has been overcome.

For npB the cross-section rises as $|\beta_p|$ increases, and at low energies it has the parabolic form $\sigma(\beta) = \sigma(0)(1 + (\beta_p/\beta_{pm})^2)$, the cross-section at the kinematic limits being twice the coplanar value. For this experiment, where all β_p angles were accepted, this led to a downwards correction of the result by a factor of 3/4 (Sect. 4.1).

The parabolic formula is derived in Appendix B and is a consequence of the dipole (E1) pattern of the photon angular distribution. This distribution arises in the OES calculations of Sect. 5.4; the two terms of Eq. 5.4.3 represent dipole forms whose null lies in the direction of the outgoing proton and neutron respectively. We have checked the accuracy of the distribution for this experiment and find that 97% of the cross-section is dipole about the proton, 2.7% about the neutron, and the remaining 0.3% is a non-dipole distribution due to interference of the two terms. A further point is that the parabolic formula relies on a dipole pattern in 3 dimensions whilst Eq. 5.4.3 only gives the distribution on the Harvard plane. This was also checked, for the symmetrical ($\theta_1 = \theta_2$) case, and it was found that the photon angular distribution arising from each separate term of Eq. 5.4.3 has exactly a dipole pattern in 3 dimensions. Thus, within the accuracy of the OES approximation itself, the parabolic formula is certainly valid at low energies.

Similar forms for $\sigma(\beta)$ have been found from more sophisticated calculations. The calculation of Celenza et al. ([67], Sect. 5.6) included noncoplanar predictions and their $\sigma(\beta)$ curve at 130 MeV is not noticeably different from ours. At 200 MeV their curve is flatter. This is consistent with Signell's [43] observation that the dipole shape persists up to $\simeq$ 150 MeV.

In contrast to npB, the lowest order contribution to ppB has a quadrupole photon angular distribution and this evidently causes the cross-section to fall to zero at the out-of-planar limits. At higher energies the pattern approximates to quadrupole plus a constant term [43] and several experimenters have corrected their results using the calculated noncoplanar cross-sections of Drechsel and Maximon [71]. Low energy analytic corrections are discussed by Suter et al. [77].

Finally, we note that the Harwell results for npB at 130 MeV [10] were not corrected for finite detector geometry and should be reduced by a few percent.

Although the authors rightly state that the corrections would be smaller than the experimental errors, the corrections could reliably and quite simply be deduced from the $\sigma(\beta)$ formula above. This would have the benefit of bringing the results generally closer to theoretical values.

CHAPTER 6

CONCLUSIONS

The measured value for the npB differential cross-section in Harvard geometry is:

Incident neutron energy : $4.77 \pm .17$ MeV

Outgoing angles: θ_n : $35 \pm 5^{\circ}$

θ_p : $25 \pm 10^{\circ}$

npB cross-section, $\dfrac{d^2\sigma}{d\Omega_n \, d\Omega_p}$: 60 ± 150 µb/sr^2

or < 210 µb/sr^2 .

The large uncertainty was wholly due to the very low rate of npB events; from 125 hours' running, 9 possible npB events remained after all the cuts and $\simeq 1.5$ after background subtraction. This low rate was, in turn, caused by the high selectivity of the experiment, using detectors for all three final-state particles, which was necessary to count npB events preferentially above background. Due to the low rate, npB events were not conspicuous at any stage in the data reduction, thus the presence of events due to competing processes cannot be ruled out (Sect. 3.11). Nevertheless, this observation does not invalidate the above upper-limit statement of the cross-section.

The question arises as to whether any changes to the experiment would reduce the uncertainty. The obvious possibility is an extension of running time, but only a large extension would bring significant advantage. For instance, assuming that ideal experimental conditions could be maintained, based on the observed event rates, $\simeq 700$ hours' running would be necessary to achieve a positive lower limit. Apart from this, only two other useful changes have come to light as follows:

i) the use of newer photomultipliers and faster electronics (Sect. 2.6a) for the stilbene detectors should result in better p-γ separation by PSD which would then allow lower bias levels and higher detection efficiency;

ii) collection of events over a large background range of T_1 (time between counts in the stilbene detectors). This would marginally reduce the

error from background subtraction (Sect. 3.13c).

These changes would not reduce the overall uncertainty by more than a few percent.

Our upper limit is above the various theoretical predictions (Table 5.2) and hence is not able to distinguish them. On the other hand, when put into perspective with other known npB experiments (Table 6.1), it is the most accurate result to date in the low energy region and indicates the greatest precision to be expected from available technology.

Energy MeV	Institution	θ_n, θ_p	Cross-section $d^2\sigma/d\Omega_n d\Omega_p$	Ref.	Date reported
208	U.C. Davis	$30^0, 30^0$	35 ± 14 $\mu b/sr^2$	9	1968
130	Harwell	$32^0, 29^0$	77 ± 32 $\mu b/sr^2$	10	1974
14.4	R. Boskovic Zagreb	$30^0, 30^0$	< 400 $\mu b/sr^2$	11	1970
14	U.C.L.A.	$30^0, All$	$(< 170$ $\mu b/sr)$*	12	1967
4.8	Cape Town	$35^0, 25^0$	60 ± 150 $\mu b/sr^2$ or < 210 $\mu b/sr^2$		1979

Table 6.1: npB experiments at or near $\theta_n = \theta_p = 30^0$ in Harvard geometry including the result from this work.
  * Single differential cross-section, $d\sigma/d\Omega_n$. This result implies an upper-limit to $d^2\sigma/d\Omega_n d\Omega_p$ of the order of 3 mb/sr^2.

It is within the bounds of possibility that improvements could be made to the extent that McGuire's 'O' prediction (140 $\mu b/sr^2$, Table 5.2) could be tested. If his prediction is realistic, and off-shell effects are indeed large, then this energy region is a very useful one as calculations need not include all the usual contributions and corrections such as internal scattering, magnetic transitions and relativistic effects. In this case it would certainly be worth while to try to test his result. If, as seems more likely (Sect. 5.7), the off-shell effects are small at these low energies, then at least an order of magnitude improvement in accuracy will be necessary to observe them. This degree of improvement does not seem possible.

The usefulness of our measurement should be viewed against the success of NNB experiments as a whole. If we measure success in terms of how well NNB has been able to test potentials, then the results have not been spectacular. Even the latest comprehensive ppB experiments have not been able to decide

convincingly whether or not the Hamada-Johnston potential is good off the energy shell [5]. This is simply because off-shell effects and model dependence have generally been found to be small.

One should inquire as to what new NNB experiments should be done in order to further our knowledge of the off-shell N-N interaction. There is general agreement that high relative photon energies correspond to maximum off-shell effects (Sect. 5.5) and, in Harvard geometry, this means working at small angles θ_1, θ_2. In comparison with the other experimental difficulties, this does not pose such a problem for low energy npB as it does for ppB. Background was already severe at the angles used, and a relatively small worsening would result at small θ_1, θ_2. One could even contemplate working at $\theta_1 = \theta_2 = 0^0$ which would be totally impossible for ppB. It is also implied by OES calculations (Sect. 5.4) that the npB cross-section increases at smaller angles although the validity of the OES approximation is not necessarily substantiated in this extreme region $(P_1', P_2' \rightarrow 0)$.

For NNB experiments as a whole, there is a lack of coherent theoretical guidance as to what experiments should be performed and with what accuracy [5], and this is manifested by the wide variety of ppB experiments recently undertaken. A number of groups have turned their attention to small angles [78] following the contention that this should maximise off-shell effects. There have also been experiments at low energy, 6.92 MeV [74] and 11 and 13 MeV [75] where, for ppB, off-shell effects are negligible [43], and one experiment at 730 MeV [8] with large θ_1, θ_2, overlapping the elastic limit.

Moravcsik [79] has claimed that certain NNB polarization measurements would be able to isolate off-shell effects, but this has been doubted by Fearing [80]. In the same paper, Fearing maintains that off-shell effects will be largest when two parameters are maximised; these are $k/\overline{E}$ as before, and an 'off-shell parameter', Δm^2, which increases with incident energy. According to these rules, one should use small angles and the highest possible incident energy. Finally, Liou [50] suggests that measurements should be expressed in terms of 'Rochester' geometry, in which the cross-section is a function of the photon energy and angles, rather than Harvard geometry.

It is perhaps discouraging that the considerable effort that has been applied to NNB, although giving much insight into the NNB process itself, has so far brought such meagre knowledge of the off-shell 2-nucleon interaction. This comment could equally apply to the N-N interaction as a whole including on-shell. The basic difficulty lies in the complexity of the strong interaction itself. The standard theoretical 'explanation' of the strong force is that it

results from a sum of meson exchanges, but calculations are intractable above one or two pion exchange. Beyond this there is no better available tool than phenomenological analysis in terms of potentials.

One can speculate that the final solution may come from a more fundamental approach, such as studies of the internal structure of the nucleon now taking place. The inter-nucleon force may then be seen, for instance, as the residue of a relatively simple inter-quark force, just as complex inter-atomic forces stem from the simple Coulomb force in atoms.

APPENDIX A

KINEMATICS

A.1 KINEMATIC RESTRICTIONS FOR npB EVENTS

For a specified incident neutron energy, E, there are 9 variables (Fig. A.1) for the 3 outgoing particles, of which 5 are independent after conserving energy and momentum. Since the event is invariant under rotation about the incident
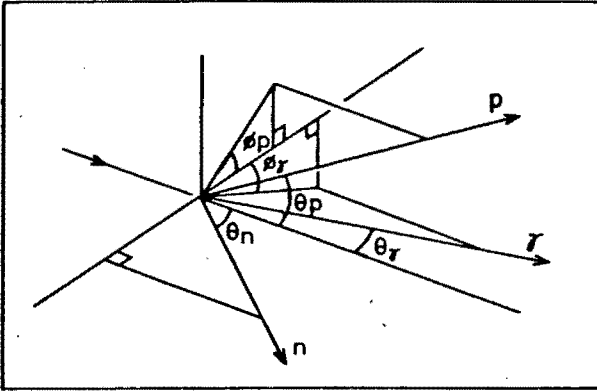

Fig. A.1

Definition of angles of outgoing particles.

particle axis (the beam and target are unpolarized), we define the scattered neutron azimuth, ϕ_n, as zero, leaving any four variables independent out of the group E_n, θ_n, E_p, θ_p, ϕ_p, E_γ, θ_γ, ϕ_γ. Considering these independent variables as E_n, θ_n, E_p, θ_p, the following analysis consists of derivations of conditions for extrema of one member of this subgroup when one or more of the others are specified. These conditions are then applied to the experimental configuration to map the kinematically allowed loci with respect to these variables (Fig. A.3). Relativistic formulation is used, and all variables refer to the laboratory reference frame. The formulation applies equally to proton-proton bremsstrahlung (ppB).

A.1a Energy and momentum relations

To simplify the formulation, we use dimensionless momenta:

$$P_i/mc \rightarrow P_i \qquad\qquad\qquad A.1.1$$

where P_i = laboratory momentum of ith particle,

and m = proton mass = neutron mass.

The relativistic kinetic energy to momentum conversions are then:

$$\text{nucleons} \begin{cases} P_N = \sqrt{2E_N/mc^2 + (E_N/mc^2)^2} \\ \\ E_N = mc^2 \left(\sqrt{1 + P_N^2} - 1 \right) \end{cases}$$

A.1.2

photons $\quad E_\gamma = mc^2 P_\gamma$

A.1.3

and the relativistic conservation of energy equation is:

$$1 + \sqrt{1 + P^2} = \sqrt{1 + P_n^2} + \sqrt{1 + P_p^2} + P_\gamma$$

A.1.4

In the non-relativistic limit, this becomes:

$$P^2 = P_n^2 + P_p^2 + 2P_\gamma$$

A.1.5

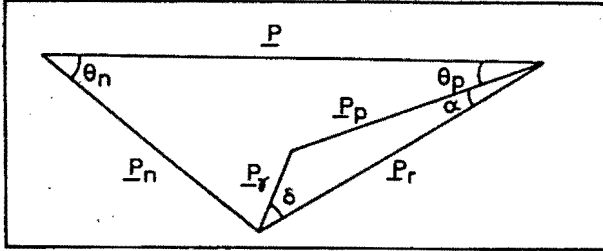A.1b <u>Extrema of E_p for specified E_n, θ_n</u>

Fig. A.2

Laboratory frame momentum diagram.

The momenta, $\underline{P}_i$, can be combined in the diagram of Fig. A.2. Now $\underline{P}_n$ is completely specified, as $\phi_n = 0$ by definition, hence $\underline{P}_r$, the resultant from $\underline{P}$ and $\underline{P}_n$, is also fixed. The two degrees of freedom remaining can be stated as

(a) rotation of triangle $\underline{P}_r, \underline{P}_\gamma, \underline{P}_p$ about $\underline{P}_r$;

(b) variation of angle δ through 2π.

These changes cover all possible photon angles. Evidently (a) has no effect on P_p (and hence E_p), and the extrema of P_p occur when $\delta = 0$ or π, thus $P_p \pm P_\gamma = P_r$.

Combining with Eq. A.1.4 to eliminate P_γ, the extrema of P_p are:

$$P_p(\text{ext.}) = \left| \frac{(A \pm P_r)^2 - 1}{2(A \pm P_r)} \right|$$

A.1.6

where $\quad$ A $\quad = \quad 1 + \sqrt{1 + P^2} - \sqrt{1 + P_n^{\,2}}$

and $\qquad P_r^{\,2} \quad = \quad P^2 + P_n^{\,2} - 2PP_n \cos\theta_n$

from Fig. A.2.

Eq. A.1.6 can equally be used to find the extrema of E_n for specified E_p, θ_p, as the formulation remains the same when the scattered proton and neutron are interchanged. An example of the application of Eq. A.1.6 is shown in Fig. A.3.

A.1c Allowed E_p-E_n region for specified θ_p, θ_n

We consider first the case when E_p, E_n, i.e. P_p, P_n are fixed, and thus P_γ is also fixed by conservation of energy. Referring to Fig. A.2, the freedom within the plane is again the variation of angle δ through 2π. This rotation then gives the locus of the kinematic limits of θ_p, θ_n for fixed E_p, E_n, since any departure from coplanarity by taking P_{-p} out of the plane will bring θ_p inwards from the limit. Thus the extrema occur when the event is coplanar.

It is less obvious but can be similarly shown that if θ_p, θ_n are fixed, the limits of E_p, E_n are also obtained by varying δ through 2π in the coplanar case.

From Fig. A.2, $\quad P_\gamma^{\,2} \quad = \quad P_p^{\,2} + P_r^{\,2} - 2P_p P_r \cos\alpha$.

Combining with Eq. A.1.4 to eliminate P_γ, the extrema of P_p for fixed θ_n, θ_p, P_n can be obtained:

$$P_p(\text{ext.}) \quad = \quad \frac{P_s(A^2 - P_r^{\,2} + 1) \pm A \sqrt{(A^2 - P_r^{\,2} + 1)^2 - 4(A^2 - P_s^{\,2})}}{2(A^2 - P_s^{\,2})} \qquad \text{A.1.7}$$

where $\qquad P_s \quad = \quad P_r \cos\alpha \quad = \quad P\cos\theta_p - P_n \cos(\theta_p + \theta_n)$

and A and P_r are as given above.

Equation A.1.7 was used to draw the small areas of Fig. A.3.

Since the extrema of E_n, E_p occur when the event is coplanar, the peripheries of the small regions of Fig. A.3 are the allowed loci for events in Harvard (coplanar) geometry. Only non-coplanar events can populate the insides of the regions.
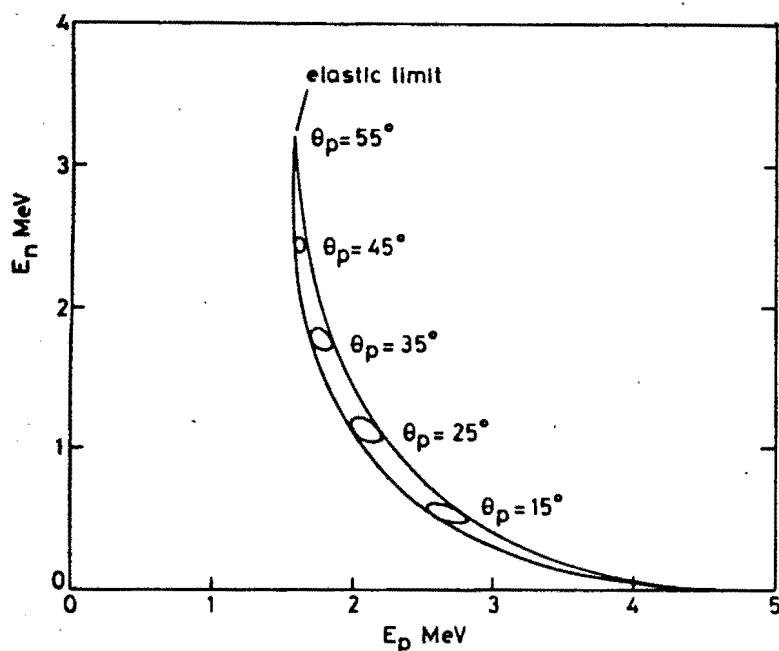
Fig. A.3

Kinematically allowed regions for E = 4.8 MeV, $\theta_n = 35^0$ (envelope). The small areas apply when θ_p is also fixed.

A.2 LOW-ENERGY EXPRESSIONS

At the incident energy of the experiment, $P/mc \ll 1$ ($P/mc = 0.10$ at E = 4.8 MeV); by conservation of energy (Eqs. A.1.5 and A.1.1) this further implies that $P_\gamma/P \ll 1$ ($P_\gamma/P \simeq .016$ at the angles observed). These inequalities are used below to obtain approximate expressions required in the evaluation of the experimental cross-section (Sect. 4.2) and in the theoretical OES prediction (Sect. 5.4).

A.2a Outgoing momenta

In formulating the phase-space factor (Sect. 5.4) explicit expressions are required for the outgoing laboratory momenta in terms of the scattering angles. From Fig. A.2, letting $P_\gamma/P \to 0$:

$$P_n = P \sin\theta_p / \sin(\theta_n+\theta_p)$$
$$P_p = P \sin\theta_n / \sin(\theta_n+\theta_p)$$

Then using Eq. A.1.5 (and Eq. A.1.1):

$$P_\gamma = \frac{P^2}{mc} \frac{\sin\theta_n \sin\theta_p \cos(\theta_n+\theta_p)}{\sin^2(\theta_n+\theta_p)}$$

The above could also be obtained as the lowest orders in series expansions of the momenta in powers of P/mc as has been done by Signell [43] in the symmetrical ($\theta_n = \theta_p$) case.

A.2b Centre-of-mass to laboratory frame conversions

The transition amplitude (Eq. 5.4.2) is evaluated in the centre-of-mass (cm) system and the quantities $\hat{\epsilon}.\underline{P}'_p$ and $\hat{\epsilon}.\underline{P}_p$ must be expressed in terms of laboratory variables.
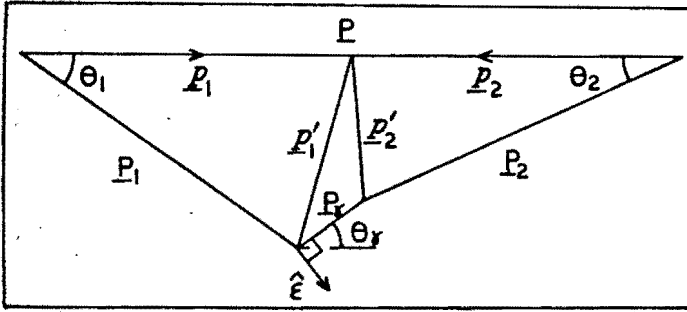
Fig. A.4

Relationship of centre-of-mass to laboratory frame momenta for coplanar geometry.

	Centre-of-mass	Laboratory	
		NNB	npB
incident momenta	P_1	P	P
	P_2	–	–
outgoing momenta	P'_1	P_1	P_n
	P'_2	P_2	P_p
	P_γ	P_γ	P_γ

Table A.1: Definition of momenta in the centre-of-mass and laboratory reference frames.

If the photon polarization vector, $\hat{\epsilon}$, is taken to be in the experimental plane as shown in Fig. A.4, then letting $P_\gamma/P \rightarrow 0$, the required expressions are:

$$\hat{\epsilon}.\underline{P}_p = -P/2 \sin\theta_\gamma$$

$$\hat{\epsilon}.\underline{P}'_p = -P/2\left\{\frac{\sin\theta_n \sin(\theta_p-\theta_\gamma) + \sin\theta_p \sin(\theta_n+\theta_\gamma)}{\sin(\theta_n+\theta_p)}\right\}$$

The centre-of-mass and equivalent laboratory frame momenta are defined in Table A.1.

A.2c Noncoplanarity limit

The noncoplanarity limit of the proton as expressed by the maximum value, β_{pm}, of angle β_p (Fig. A.5) was required in the transformation to Harvard geometry (Sect. 4.2). β_{pm} is a function of P_n and P_p (or θ_n and θ_p) and its value was calculated for all points remaining after the data reduction. In the limit $P_\gamma/P \to 0$, β_p is extreme when the photon is emitted normal to the experimental plane, hence $\beta_{pm} = P_\gamma/P_p$, with P_γ obtained from Eq. A.1.4.

The error involved in this approximation is of the order of $\tan \beta_{pm} - \beta_{pm}$ which, with the largest value of β_{pm} obtained (1.5^0), is only .05%.
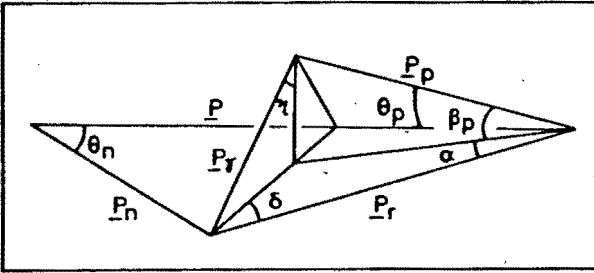

Fig. A.5

Momentum diagram showing the noncoplanarity angle, β_p. (P_γ is exaggerated.)

APPENDIX B

PHOTON ANGULAR DISTRIBUTION

At low incident energy the angular distribution of the npB photon has a dipole pattern about the direction of the scattered proton (see Eq. 5.4.3 and following paragraph, and Sect. 5.8). On this basis we now derive the distribution of npB events with respect to the noncoplanarity angle β_p (Fig. A.5) which the proton makes with the plane containing the incident and scattered neutrons. Formulae are given for use in the transformation to Harvard geometry (Sect. 4.2) and in the photon detection efficiency calculation (Sect. 4.8). It is also shown that the npB cross-section for Harvard (coplanar) geometry should be divided by the 'Harvard factor' of $4/3$ if the full 4π range of photon angles is observed.

B.1 DISTRIBUTION OF npB EVENTS WITH RESPECT TO ANGLE β_p

Defining a system of spherical coordinates, θ, ϕ, about the proton direction (Fig. B.1) the dipole law is:

$$\frac{dn}{d\Omega} = \frac{3}{8\pi} \sin^2\theta \qquad\qquad \text{B.1}$$

where dn is the probability that the photon scatters into solid angle $d\Omega = \sin\theta\, d\theta\, d\phi$, and the normalisation is such that:
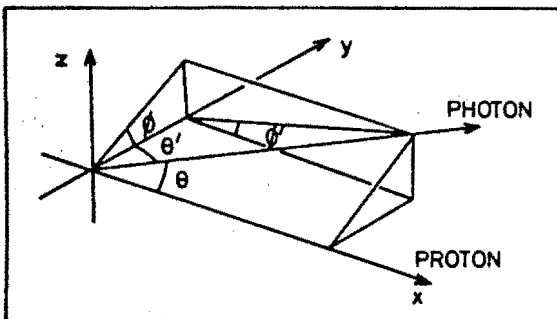
$$\int \frac{dn}{d\Omega}\, d\Omega = 1 .$$

Fig. B.1

Definition of new coordinates, (θ', ϕ').

Transforming to the new coordinates θ', ϕ' (Fig. B.1), Eq. B.1 becomes:

$$\frac{dn}{d\theta' d\phi'} = \frac{3}{8\pi} (1 - \sin^2\theta' \cos^2\phi') \sin\theta' \qquad \text{B.2}$$

The probability of photon scatters at angle θ' is given by integrating Eq. B.2 with respect to ϕ':

$$\frac{dn}{d\theta'} = \frac{3}{8} (1 + \cos^2\theta') \sin\theta' \qquad \text{B.3}$$

Referring to Fig. A.5, since β_p is small, and $P_\gamma \ll P_p$, we can identify angle θ' with η and:

$$\beta_p = \beta_{pm} \cos\theta',$$

where $\beta_{pm} = P_\gamma / P_r$, the extreme value of β_p. Combining with Eq. B.3

$$\frac{dn}{d\beta_p} = \frac{3}{8\beta_{pm}} (1 + \beta_p^2/\beta_{pm}^2) \qquad \text{B.4}$$

Alternatively:

$$f(\beta_p) = 1 + \beta_p^2/\beta_{pm}^2 \qquad \text{B.5}$$

expresses the same distribution normalised such that $f(0) = 1$, and this is the result required for the transformation of Sect. 4.2. It is noteworthy that the distribution has a minimum for coplanar events and rises to maxima at the out-of-planar limits (Fig. B.2).
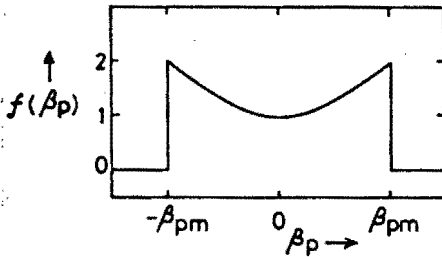

Fig. B.2

Distribution of npB events with respect to angle β_p.

If all kinematically allowed angles β_p are observed, the average value of $f(\beta_p)$ is:

$$\bar{f} = \int_{-\beta_{pm}}^{\beta_{pm}} f(\beta_p) d\beta_p \bigg/ \int_{-\beta_{pm}}^{\beta_{pm}} d\beta_p = {}^4\!/_3 ..$$

Hence, the 'Harvard factor', $\overline{f}/f(0)$ is $4/3$, as established in Sect. 4.2.

The distribution with respect to β_p was found for the purposes of the arguments of Sect. 4.2. However, the Harvard factor can be more simply derived by defining the plane to contain the outgoing proton instead of the neutron, then considering x-z of Fig. B.1 as this plane, the condition for coplanarity is $\theta' = \pi/2$. This condition can then be applied to Eq. B.3 and the Harvard factor emerges directly without approximation.

B.2 APPLICATION TO PHOTON DETECTION EFFICIENCY

In the calculation of the photon detection efficiency (Sect. 4.8b), the angular distribution of photons is required in a coordinate system where the axis of symmetry is the axis of the stilbene crystals. The proton direction is taken as being normal to this axis. The coordinates θ',ϕ' of Fig. B.1 satisfy these conditions, thus from Eq. B.2:

$$\frac{dn}{d\Omega} = \frac{3}{8\pi} (1 - \sin^2\theta' \cos^2\phi')$$

Alternatively:

$$g(\theta',\phi') = 3/2(1 - \sin^2\theta' \cos^2\phi') \qquad \text{B.6}$$

expresses the same distribution where g is normalised so that its average value is 1, $\int g d\Omega/\int d\Omega = 1$.

APPENDIX C

CROSS-SECTIONS FOR COMPTON SCATTERING

Equations are given below for the Compton cross-section as a function of electron energy. These are necessary for the calculation of the photon detection efficiency (Sect. 4.8c).

The unpolarized Compton cross-section as a function of recoil photon angle, θ_γ, is [81]:

$$\frac{d\sigma}{d\Omega} = \frac{r_0^2}{2}\left(\frac{\nu'}{\nu}\right)^2\left(\frac{\nu}{\nu'}+\frac{\nu'}{\nu}-\sin^2\theta_\gamma\right) \quad ; \quad d\Omega = 2\pi\sin\theta_\gamma\,d\theta_\gamma \qquad \text{C.1}$$

where r_0 = classical electron radius, 2.817×10^{-13} cm,

ν, ν' = initial, final photon energy (h = 1).

The electron energy, T, is related to θ_γ by kinematics:

$$T = \frac{\nu^2(1-\cos\theta_\gamma)}{m_0+\nu(1-\cos\theta_\gamma)} \qquad \text{C.2}$$

where m_0 = electron rest mass, .511 MeV (c = 1).

By conservation of energy, $T = \nu-\nu'$, then Eqs. C.1 and C.2 are used to evaluate $\frac{d\sigma}{dT} = \frac{d\sigma}{d\theta_\gamma}\frac{d\theta_\gamma}{dT}$:

$$\frac{d\sigma}{dT}(\nu,T) = \frac{\pi r_0^2 m_0}{2\nu^4}\left(\frac{\nu^3(\nu-T)+\nu(\nu-T)^3-2m_0 T\,\nu(\nu-T)+m_0^2 T^2}{(\nu-T)^2}\right) \qquad \text{C.3}$$

Eq. C.3 is the formula for the characteristic Compton distribution obtained when detecting radiation from a monoenergetic source. If the detector has a bias at an electron energy T_b, the total cross-section is obtained by integrating Eq. C.3 from T_b to T_{max}, where $T_{max} = 2\nu^2/(m_0+2\nu)$ from Eq. C.2:

$$\int_{T_b}^{T_{max}}\frac{d\sigma}{dT}\,dT = \frac{\pi r_0^2 m_0}{\nu^3}\left\{(\nu^2-2m_0^2-2\nu m_0)\,\log_e\left(\frac{(\nu-T_b)(m_0+2\nu)}{\nu m_0}\right)\right.$$

$$\left. + m_0\left(\frac{1}{\nu}+\frac{1}{\nu-T_b}\right)\left(2\nu^2-T_b m_0-2\nu T_b\right)+\tfrac{1}{2}\left((\nu-T_b)^2-\left(\frac{\nu m_0}{m_0+2\nu}\right)^2\right)\right\} \qquad \text{C.4}$$

If $T_b = 0$, this simplifies to:

$$\int_o^{T_{max}} \frac{d\sigma}{dT} dT = 2\pi r_0^2 \left\{ \left(\frac{1}{2\alpha} - \frac{1}{\alpha^3} - \frac{1}{\alpha^2} \right) \log_e (1 + 2\alpha) + \frac{2}{\alpha^2} + \frac{1+\alpha}{(1+2\alpha)^2} \right\} \qquad \text{C.5}$$

where $\quad \alpha = \dfrac{(h)\nu}{m_0(c^2)}$.

APPENDIX D

LOSSES FROM TAC DEADTIME AND PILEUP REJECTION

At the start input to a TAC (time-to-amplitude converter), signals are only accepted if there has been no previous accepted start within the start reset period, τ_T (2.1 μs*). If a stop input is received during the TAC set time, ω_1 (e.g. 50 ns) from an accepted start, τ_T is extended to τ_c ($\simeq$ 7.5 μs*), the conversion reset period. In most applications, the rate of starts is much greater than the coincidence rate, so this latter contribution to deadtime is disregarded in the following.

The pileup rejector (PUR) accepts signals only if there were no other signals within the unit's set period, τ_p. In this experiment (see Sect. 2.7f), τ_p (3 μs) was divided so that rejection occurred if there was a signal within τ_{p-} (0.6 μs) following the signal in question (pulse-pair rejection) or within τ_{p+} (2.4 μs) prior to it. The salient difference from rejection at the TAC start is that the PUR begins its busy period at every signal whilst the TAC only becomes busy after accepted signals.

In designing the experiment and in setting count rates it was important to know what losses to expect from pileup rejection and TAC deadtime, separately and in combination. Formulae to answer these questions are now given, together with the means to assess, in a given situation, what measure of protection against pileup is provided at the start input to a TAC by its deadtime.

The derivations all depend on the fact that events occur at random times with an average rate μ.

D.1 PROBABILITY THAT AN EVENT WILL PASS PILEUP REJECTION

The probability of passing PUR, P_p, is simply the probability that zero events occur within a period τ_p.

This is derived from the Poisson distribution, $P(r,\tau) = (\mu\tau)^r e^{-\mu\tau}/r!$ where $P(r)$ is the probability that exactly r events occur within a period τ when the average rate is μ. Thus:

---

* Reset periods are quoted for Ortec 437A or 467.

$$P_p = P(0,\tau_p) = e^{-\mu\tau_p} \qquad\qquad \text{D.1}$$

This applies for pileup and pulse-pair rejection provided τ_p is the sum of the periods, $\tau_p = \tau_{p-} + \tau_{p+}$, since the probability is then

$$P_p = e^{-\mu\tau_{p+}} e^{-\mu\tau_{p-}} = e^{-\mu\tau_p}$$

D.2 PROBABILITY OF ACCEPTANCE OF EVENTS AT A TAC START INPUT

The probability of passing the TAC start is equal to the fraction of time that the TAC is not busy:

$$P_T = 1 - \mu'\tau_T$$

where $\mu' = P_T\mu$ = average rate of accepted starts.

Then:

$$P_T = \frac{1}{1 + \mu\tau_T} \cdot \qquad\qquad \text{D.2}$$

D.3 JOINT PROBABILITY OF LOSS WHEN PILEUP REJECTION IS USED AT A TAC START INPUT

If $\tau_{p+} \geqslant \tau_T$, the TAC can not cause any losses over and above the pileup losses as any event within the previous τ_T will cause rejection by pileup anyway. The probability of an event passing both units, P_{PT}, is then:

$$P_{PT} = P_P = e^{-\mu\tau_p} \quad \text{for} \quad \tau_{p+} \geqslant \tau_T \cdot \qquad\qquad \text{D.3a}$$

On the other hand, if $\tau_{p+} < \tau_T$, it is possible for an event to pass PUR and be rejected by the TAC, or to pass the TAC and be rejected by PUR (Fig. D.1).
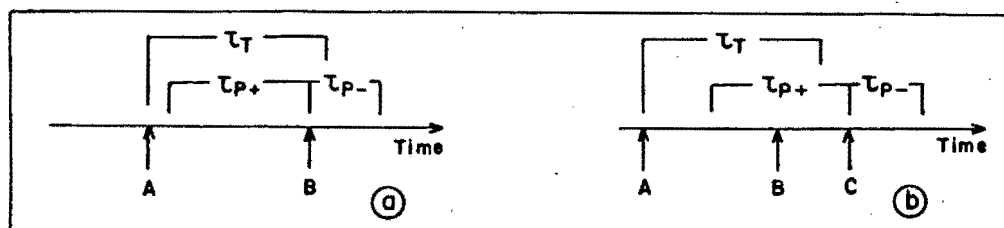

Fig. D.1

Event loss by pileup rejection and TAC start deadtime when $\tau_{p+} < \tau_T$. (a) event B was not piled-up but was lost as the TAC was busy from event A; (b) event C was lost due to pileup with B; however, it passed the TAC deadtime as the TAC was busy at event B due to event A.

The derivation of the joint probability for this situation is lengthy and not of direct relevance to this experiment, so we merely state the result.

$$P_{PT} = \frac{e^{-\mu\tau_p}(1+\mu\tau_{p+})}{1+\mu\tau_T} \quad \text{for } \tau_{p+} \leqslant \tau_T \qquad \text{D.3b}$$

This result is of interest because it can be used to find the efficiency of a TAC for pileup protection. Say, for instance, we required pileup rejection of 1 μs, i.e. $\tau_p = \tau_{p+} = 1$ μs, for a detector feeding the TAC start. Taking $\tau_T = 2.1$ μs and a rate, μ, of 50 kHz, we can calculate (see Fig. D.2):

$$P_{\bar{T}} = 1-P_T = .095 \quad ; \quad P_{\bar{P}} = 1-P_P = .049 \quad ; \quad P_{\bar{P}\bar{T}}/P_{\bar{P}} = (P_{PT}-P_T+P_{\bar{P}})/P_{\bar{P}} = .977 \ .$$

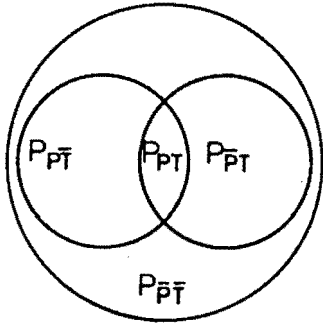
Fig. D.2

Venn diagram for probabilities of events passing pileup (P_P) and TAC start deadtime (P_T) when $\tau_{p+} < \tau_T$. The small circles represent P_p and P_T, and $P_{PT} = P_P \cap P_T$, etc.

In this example, the TAC deadtime loss is 9.5%, whilst a 1 μs PUR alone would lose 4.9% of events. However, of the events which the proper PUR would lose, 97.7% will be removed anyway by the TAC start deadtime; the TAC is thus performing the function of pileup rejection quite well.

In our experiment, $\tau_{p+} = 2.4$ μs, $\tau_T = 2.1$ μs, so $\tau_{p+} > \tau_T$ and Eq. D.3a is applicable; there were no events lost by the TAC which were not also pileup rejects. The PUR was also used at the stop input to the TAC, and it can be shown that the pass rate for the raw data in our experiment is then:

$$P'_{PT} = e^{-\mu_s\tau_p} \qquad \text{D.4}$$

where μ_s is the sum of rates at the start and stop including correlated coincidences.

The pileup fractions, $\overline{PU}$ (Sect. 3.13c), for the raw data can now be predicted as:

$$\overline{PU} = e^{-\mu_s\tau_p}/(1+\mu\tau_T) \qquad \text{D.5}$$

where μ is the start rate; the denominator is included as the events collected had already suffered deadtime loss at TAC 1.   Values of $\overline{PU}$ predicted by Eq. D.5 were in agreement with the measured values.

APPENDIX E

RATES OF RANDOM COINCIDENCES

In Sect. 4.7a the formula:

$$N_{e\ell} = N_{C1}/(\mu_2\omega) \qquad\qquad E.1$$

was used to obtain $N_{e\ell}$, the number of elastic n-p coincidences between detectors 1 and 3, from N_{C1}, the number of these scatters recorded as T_1 coincidences within a T_1 window, ω, where μ_2 is the random count rate in detector 2. We now justify this formula.

For every count in detector 1, a random T_1 coincidence will be recorded if a count occurs in detector 2 within the time ω. The probability of this, from the Poisson distribution (Sect. D.1), is $P(\geqslant 1, \omega) = 1-e^{-\mu_2\omega}$. The coincidence rate is then $\mu_R = \mu_1(1-e^{-\mu_2\omega})$ if μ_1 is the random rate in detector 1. Now $\mu_2\omega \ll 1$ (e.g. if $\mu_2 = 40$ kHz and $\omega = 50$ ns, $\mu_2\omega = 2 \times 10^{-3}$), then $1-e^{-\mu_2\omega} \simeq \mu_2\omega$ and:

$$\mu_R = \mu_1\mu_2\omega \qquad\qquad E.2$$

If we only observe those detector 1 events which are also n-p elastic coincidences with detector 3, then Eq. E.1 follows as the observed events in detectors 1 and 2 are still independently random.

APPENDIX F

THE ELECTROMAGNETIC INTERACTION

It is shown in the following how the pole terms of Eq. 5.2.3 for T_{fi} give rise to the expanded form of Eq. 5.2.4.

The field of the emitted photon is conventionally described by a real vector potential whose form is a plane wave (e.g. [32]):

$$\underline{A} = \hat{\mathcal{E}}\left(a\, e^{i(\underline{P}_\gamma \cdot \underline{r} - \omega t)} + a^* e^{-i(\underline{P}_\gamma \cdot \underline{r} - \omega t)}\right) \qquad\qquad \text{F.1}$$

where $\hat{\mathcal{E}}$ is the direction of polarization. In Gaussian units, the field energy density averaged over time is $\overline{u} = |E_0|^2/8\pi$ where E_0 is the amplitude of the electric field $\underline{E}$. Using the gauge freedom allowed by Maxwell's equations, we choose the transverse (or Coulomb) gauge which leads to $\underline{E} = -\dfrac{1}{c}\dfrac{\partial \underline{A}}{\partial t}$ and $\hat{\mathcal{E}}.\underline{P}_\gamma = 0$; then $\overline{u} = |a|^2 P_\gamma^2/2\pi$. Normalising to one photon per unit volume, $\overline{u} = \omega$ (units are such that $\hbar = 1$), then

$$|a| = \sqrt{\frac{2\pi c}{P_\gamma}} \qquad\qquad \text{F.2}$$

The non-relativistic Hamiltonian for a free particle of momentum $\underline{P}$, charge q, magnetic moment $\underline{\mu}$, moving in an electromagnetic field $\underline{A}$ is

$$H' = \frac{P^2}{2m} - \frac{q}{mc}\,\underline{A}.\underline{P} - \underline{\mu}.\nabla \times \underline{A} = \frac{P^2}{2m} + V_{em} \qquad\qquad \text{F.3}$$

This form of V_{em} arises from 'minimal coupling' [65] of the electromagnetic field to the nucleon currents, and is not strictly correct when the 2-nucleon potential contains nonlocal terms [68].

The perturbation giving rise to the emission of a photon is the coefficient of $e^{+i\omega t}$ in Eq. F.1. Using Eqs. F.2 and F.3, and omitting the phase factor in Eq. F.2, this becomes, for a single nucleon:

$$V_{em} = \sqrt{\frac{2\pi\alpha}{P_\gamma m^2}}\left\{-\mathcal{E}\,(\hat{\mathcal{E}}.\underline{P}) + \tfrac{1}{2} i\,\mu\,\underline{\sigma}.(\underline{P}_\gamma \times \hat{\mathcal{E}})\right\} e^{-i\underline{P}_\gamma \cdot \underline{r}} \qquad\qquad \text{F.4}$$

where the notation is that of Eq. 5.2.4.

We now consider the second term of Eq. 5.2.3:

$$T_{fi}^{(2)} = < \phi_f | V_{em} G_i^+ V_N | \chi_i^+ > \qquad\qquad F.5$$

Using the integral form of the Green's function:

$$< \underline{r} | G_j^\pm | \underline{r}' > = G_j^\pm (\underline{r},\underline{r}') = \frac{1}{(2\pi)^3} \int \frac{e^{i\underline{P}' \cdot (\underline{r}-\underline{r}')}}{E_j - E' \pm i\eta} d^3P'$$

and inserting complete sets of states between the operators, Eq. F.5 becomes:

$$T_{fi}^{(2)} = \int \frac{d^3P''}{(2\pi)^3} \frac{< \phi_f | V_{em} | \phi'' > < \phi'' | V_N | \chi_i^+ >}{E_i - E''} \qquad\qquad F.6$$

where we have used the plane wave normalisation $< \underline{r} | \phi > = e^{i\underline{P} \cdot \underline{r}}$ corresponding to one particle per unit volume. E_i is the energy of the initial state, and E'' that of the intermediate state between the nuclear interaction and the electromagnetic vertex.

Using Eq. F.4, and the explicit form for $| \phi >$; e.g. $< \underline{r} | \phi_f > = < \underline{r}_1, \underline{r}_2 | \underline{P}'_1, \underline{P}'_2 >$ we have: $< \phi_f | V_{em} | \phi'' > =$

$$-(2\pi)^6 \sqrt{\frac{2\pi\alpha}{P_\gamma m^2}} \left\{ \left(\epsilon_1 (\hat{\epsilon} \cdot \underline{P}'_1 - \tfrac{1}{2} i\mu_1 \underline{\sigma}_1 \cdot (\underline{P}_\gamma \times \hat{\epsilon}) \right) \delta^3 (\underline{P}''_1 - \underline{P}_\gamma - \underline{P}'_1) \delta^3 (\underline{P}''_2 - \underline{P}'_2) \right.$$

$$\left. + \left(\epsilon_2 (\hat{\epsilon} \cdot \underline{P}'_2 - \tfrac{1}{2} i\mu_2 \underline{\sigma}_2 \cdot (\underline{P}_\gamma \times \hat{\epsilon}) \right) \delta^3 (\underline{P}_1 - \underline{P}_\gamma) \delta^3 (\underline{P}''_2 - \underline{P}_\gamma - \underline{P}'_2) \right\} \qquad F.7$$

Substituting Eq. F.7 into F.6, integrating over the delta functions $(d^3P'' \to d^3P''_1 d^3P''_2)$, and using the definition of the transition operator $T_N(E_j) | \phi_j > = V_N | \chi_j^+ >$ results in the first two terms of Eq. 5.2.4. The third and fourth terms of Eq. 5.2.4 follow from the third term of Eq. 5.2.3 in an identical manner.

REFERENCES

1. M.J. MORAVCSIK, 'The two-nucleon interaction'. (Clarendon Press, Oxford, 1963).

2. T. HAMADA and I.D. JOHNSTON, Nucl. Phys. 34 (1962) 382.

3. M. BARANGER, B. GIRAUD, S.K. MUKHOPADHYAY and P.U. SAUER, Nucl. Phys. A138 (1969) 1.

4. M.L. HALBERT, Proc. Gull Lake Symposium on the Two-body force in Nuclei, ed. S.M. Austin and G.M. Crawley, (Plenum, New York 1972) p. 53.

5. J.V. JOVANOVICH, Proc. Int. Conf. on Nucleon-Nucleon Interactions, ed. D.F. Measday et al., Vancouver 1977. (A.I.P. Conf. Procs. No. 41. American Inst. Phys. New York 1978) p. 451.

6. J.H. McGUIRE, and W.A. PEARCE, Nucl. Phys. A162 (1971) 573.

7. L.G. GREENIAUS, J.V. JOVANOVICH, R. KERCHNER, T.W. MILLAR, C.A. SMITH and K.F. SUEN, Phys. Rev. Lett. 35 (1975) 696.

8. B.M.K. NEFKENS, O.R. SANDER and D.I. SOBER, Phys. Rev. Lett. 38 (1977) 876.

9. F.P. BRADY, J.C. YOUNG and C. BADRINATHAN, Phys. Rev. Lett. 20 (1968) 750. F.P. BRADY and J.C. YOUNG, Phys. Rev. C2 (1970) 1579; Phys. Rev. C7 (1973) 1707.

10. J.A. EDGINGTON, V.J. HOWARD, I.M. BLAIR, B.E. BONNER, F.P. BRADY and M.W. McNAUGHTON, Nucl. Phys. A218 (1974) 151.

11. M. FURIC, V. VALKOVIC, D. MILJANIC, P. TOMAS and B. ANTOLKOVIC, Nucl. Phys. A156 (1970) 105.

12. J.W. VERBA, I. SLAUS, J.R. RICHARDSON, L.S. AUGUST, W.T.H. VAN OERS and R.F. CARLSON, Proc. Int. Nuclear Physics Conference, Gatlinburg 1966 (Academic Press, New York, 1967) p. 619.

13. J.B. BIRKS, 'The Theory and Practice of Scintillation Counting'. (Pergamon, London 1964).

14. J. TUDORIC-GHEMO, Nucl. Phys. A92 (1966) 233.

15. P. BOSCHUNG, J.T. LINDOW and E.F. SHRADER, Nucl. Phys. A161 (1971) 593.

16. R.M. WILENZICK, K.K. SETH, P.R. BEVINGTON and H.W. LEWIS, Nucl. Phys. 62 (1965) 511.

17. C. ROLFS and R.E. AZUMA, Nucl. Phys. A227 (1974) 291.

18. F.D. BROOKS and D.T.L. JONES, Nucl. Inst. and Meth. 121 (1974) 69.

19. D.G. SCHUSTER, Nucl. Inst. and Meth. 76 (1969) 35.

20. R.B. OWEN, Nucleonics 17 No. 9 (1959) 92.

21. T.K. ALEXANDER and F.S. GOULDING, Nucl. Inst. and Meth. 13 (1961) 244.

22. J.M. ADAMS and G. WHITE, Nucl. Inst. and Meth. 156 (1978) 459.

23. J.A. HARVEY and N.W. HILL, Nucl. Inst. and Meth. 162 (1979) 507.

24. E. KOWALSKI, 'Nuclear Electronics'. (Springer-Verlag, Berlin, 1970).

25. D.A. GEDKE and W.J. McDONALD, Nucl. Inst. and Meth. 58 (1968) 253.

26. H.H. KNOX and T.G. MILLER, Nucl. Inst. and Meth. 101 (1972) 519.

27. D.T.L. JONES, Ph.D. Thesis, Univ. Cape Town 1972 (unpublished).

28. D.L. SMITH, R.G. POLK and T.G. MILLER, Nucl. Inst. and Meth. 64 (1968) 157.

29. L.E. BEGHIAN and S. WILENSKY, Nucl. Inst. and Meth. 35 (1965) 34.
    R. HONECKER and H. GRASSLER, Nucl. Inst. and Meth. 46 (1967) 282.

30. J. ASHKIN and R.E. MARSHAK, Phys. Rev. 76 (1958) 49.

31. B. GOTTSCHALK, W.J. SCHLAER and K.H. WANG, Phys. Lett. 16 (1965) 294;
    Nucl. Phys. 75 (1966) 549.

32. M.I. SOBEL and A.H. CROMER, Phys. Rev. 132 (1963) 2698.

33. A.H. CROMER and M.I. SOBEL, Phys. Rev. 152 (1966) 1351.

34. E.M. NYMAN, Phys. Reports 9 (1974) 179.

35. M.K. LIOU and M.I. SOBEL, Ann. Phys. 72 (1972) 323.

36. H.P. STAPP, T.J. YPSILANTIS and N. METROPOLIS, Phys. Rev. 105 (1957) 302.

37. L. WOLFENSTEIN, Ann. Rev. Nucl. Sci. 6 (1956) 43.

38. M.H. MacGREGOR, M.J. MORAVCSIK and H.P. STAPP, Ann. Rev. Nucl. Sci. 10 (1960) 291.   B.P. NIGAM, Rev. Mod. Phys. 35 (1963) 117.   I. SLAUS, 'Theory of Nuclear Structure', Trieste Lectures 1969 (I.A.E.A., Vienna, 1970) p. 17.

39. M.I. SOBEL, Phys. Rev. 138 (1965) B1517;   Phys. Rev. 156 (1967) 1553.

40. L.S. CELENZA, B.F. GIBSON, M.K. LIOU and M.I. SOBEL, Phys. Lett. 42B (1972) 331.

41. J.V. JOVANOVICH, L.G. GREENIAUS, J. McKEOWN, T.W. MILLAR, D.G. PETERSON, W.F. PRICHETT, K.F. SUEN and J.C. THOMPSON, Phys. Rev. Lett. 26 (1971) 277.

42. H. FESHBACH and D.R. YENNIE, Nucl. Phys. 37 (1962) 150.

43. P. SIGNELL, Adv. Nucl. Phys. 2 (1969) 223.

44. M.K. LIOU and K.S. CHO, Nucl. Phys. A145 (1970) 369.

45. F.E. LOW, Phys. Rev. 110 (1958) 974.

46. L. HELLER, Phys. Rev. 174 (1968) 1580.

47. M.K. LIOU, Phys. Rev. C2 (1970) 131.   M.K. LIOU and M.I. SOBEL, Phys. Rev. C3 (1971) 1430;   Phys. Rev. C4 (1971) 1507.

48. H.W. FEARING, Proc. Int. Conf. on Nucleon-Nucleon Interactions, ed. D.F. Measday et al., Vancouver, 1977.   (A.I.P. Conf. Procs. No. 41. American Inst. Phys. New York, 1978) p. 506.

49. H.W. FEARING, Phys. Rev. C6 (1972) 1136.

50. M.K. LIOU, Phys. Rev. D18 (1978) 3390.

51. T.H. BURNETT and N.M. KROLL, Phys. Rev. Lett. 20 (1968) 86.

52. H.W. FEARING, Phys. Rev. D7 (1973) 243.

53. B.M. NEFKENS, O.R. SANDER, D.I. SOBER and H.W. FEARING, Phys. Rev. C19 (1979) 877.

54. V.R. BROWN, Phys. Rev. 177 (1969) 1498.

55. M.A. PRESTON and W. VAN DIJK, Phys. Rev. C19 (1979) 1693.

56. M.K. SRIVASTAVA and D.W.L. SPRUNG, Adv. Nucl. Phys. 8 (1975) 121.

57. D. DRECHSEL and L.C. MAXIMON, Phys. Lett. 26B (1968) 477.

58. J.H. McGUIRE, A.H. CROMER and M.I. SOBEL, Phys. Rev. 179 (1969) 948.

59. M.J. MORAVCSIK, Rep. Prog. Phys. 35 (1972) 587.

60. V.R. BROWN and J. FRANKLIN, Phys. Rev. C8 (1973) 1706.

61. G.E. BOHANNON, Phys. Rev. C17 (1978) 865.

62. W.A. PEARCE, W.A. GALE and I.M. DUCK, Nucl. Phys. B3 (1967) 241.

63. E.M. NYMAN, Phys. Rev. 170 (1968) 1628.

64. R. BAIER, H. KUHNELT and P. URBAN, Nucl. Phys. B11 (1969) 675.

65. V.R. BROWN, Phys. Lett. 32B (1970) 259.

66. J.H. McGUIRE, Phys. Rev. C1 (1970) 371.

67. L.S. CELENZA, B.F. GIBSON, M.K. LIOU and M.I. SOBEL, Phys. Lett. 41B (1972) 283.

68. L. HELLER, Proc. Gull Lake Symposium on the Two-body force in Nuclei, ed. S.M. Austin and G.M. Crawley (Plenum, New York, 1972) p. 79.

69. J.H. McGUIRE and W.A. PEARCE, Nucl. Phys. A162 (1970) 561.

70. J.H. McGUIRE, Phys. Lett. 40B (1972) 41.

71. D. DRECHSEL and L.C. MAXIMON, Ann. Phys. 49 (1968) 403.

72. P. SIGNELL and D. MARKER, Phys. Lett. 26B (1968) 559.

73. T.K. DAHLBLOM and A.M. GREEN, Phys. Lett. 41B (1971) 23.

74. B. FROIS, M. IRSHAD, C.R. LAMONTAGNE, V. VON MOELLENDORF, R. ROY and R.J. SLOBODRIAN, Phys. Lett. 53B (1974) 341.

75. M. SUTER, W. WOLFI, G. BONANI, Ch. STOLLER and R. MILLER, Phys. Lett. 58B (1975) 36.

76. B. GOTTSCHALK, W.J. SCHLAER and K.H. WANG, Nucl. Phys. A94 (1967) 491.

77. M. SUTER, W. WOLFI, G. BONANI, Ch. STOLLER and R. MILLER, Helv. Phys. Acta 49 (1976) 863.

78. A. WILLIS, V. COMPARAT, R. FRASCARIA, N. MARTY, M. MORLET and N. WILLIS, Phys. Rev. Lett. 28 (1972) 1063.   J. SANADO, K. KONDO and S. SEKI, Nucl. Phys. A203 (1973) 388.

79. M.J. MORAVCSIK, Phys. Lett. 65B (1976) 409.

80. H.W. FEARING, Phys. Rev. Lett. 42 (1979) 21.

81. W.E. BURCHAM, 'Nuclear Physics, an Introduction', 2nd ed. (Longman, London, 1973).